Models of Electrode and Electrolyte Behavior at the Continuum Scale

by

Alexander F. Chadwick

A dissertation submitted in partial fulfillment
of the requirements for the degree of
Doctor of Philosophy
(Materials Science and Engineering)
in the University of Michigan
2018

Doctoral Committee:

Professor Katsuyo Thornton, Chair
Assistant Professor Neil P. Dasgupta
Professor John Kieffer
Associate Professor Donald J. Siegel

Alexander F. Chadwick

afchadwi@umich.edu

ORCID iD: 0000-0001-9328-8231

Dedication

In honor of my grandfather, the first Dr. Chadwick in my life.

Acknowledgements

There are many, many people without whom this dissertation would not have been possible. First and foremost, I would like to thank Prof. Katsuyo Thornton for being my advisor these past several years, as without her guidance and tutelage I would not be the researcher I am today. The only reason this dissertation exists is because she placed an enormous amount of trust in me and my abilities, even though I had barely performed any computational work before arriving at Michigan. I am also thankful to Prof. Neil Dasgupta and Prof. Don Siegel, both for being part of my committee and for the feedback they have given me over the course of our collaborations. In addition, I would like to thank Prof. John Kieffer for serving on my committee and providing valuable input over the course of my dissertation research.

Beyond my committee, I would also like to thank the members of the Thornton group, both past and present, for all of the support, camaraderie, and insight they have given me over all of the years. I am particularly grateful to the postdocs and senior grad students who mentored me in the early part of my work, including Dr. Steve DeWitt, Dr. Susan Gentry, Dr. Hui-Chia Yu, Dr. Larry Aagesen, Dr. David Montiel, and Dr. Raúl Enrique. They all took me under their collective wing throughout my studies and were always willing to answer all of my questions about electrochemistry and phase field modeling. I also would like to thank Dr. Lin Vardar, Dr. Alice Sleightholme, Prof. Chuck Monroe, Dr. Kevin Wood, Eric Kazyak, Michael Chen, and Dr. Jason Zhang for all of the experimental collaboration they provided.

I also must thank all of my wonderful friends who I have met at Michigan, as I am sure we made our graduate school experience all the more enjoyable. I am also thankful to my family

for always encouraging me, whether it was my sister, Sam, and her fiancé, Mike, for offering their perspective as fellow Ph.D. students, my parents, Pete and Linda, for their continual love and support, or my future in-laws, Mary, John, and Todd for providing another home away from home. Last, but by no means least, I must thank my wonderful fiancée, Rena, for being my rock and my loudest cheerleader throughout the course of my thesis studies.

I also must acknowledge all of the various funding agencies and user facilities that have supported my work. Much of the work contained within this thesis was supported by the Joint Center for Energy Storage Research (JCESR), an Energy Innovation Hub funded by the U.S. Department of Energy, Office of Science, Basic Energy Sciences. For the later part of my studies, support was provided from the Office of Naval Research and United Technologies Research Center under contract number N00014-14-2-0002 (subaward 0005A-1).

Many of the computational resources were provided by the National Energy Research Scientific Computing Center (NERSC), a DOE Office of Science User Facility supported by the Office of Science of the U.S. Department of Energy under contract number DE-AC02-05CH11231. This work also used the Extreme Science and Engineering Discovery Environment (XSEDE), which is supported by the National Science Foundation grant number ACI-1548562; specifically, this work used the Stampede2 system at the Texas Advanced Computing Center (TACC) and Comet at the San Diego Supercomputer Center (SDSC) through allocation TG-DMR110007. Additional computational resources were provided by Advanced Research Computing at the University of Michigan.

Table of Contents

List of Tables

List of Figures

List of Appendices

Abstract

When a reaction occurs at the surface of a metal electrode, as in metal-anode batteries or corrosion, it is often accompanied by a change in the morphology of the interface between that electrode and its surrounding environment, typically an ionically conductive electrolyte. However, there is a complex interplay between the reaction kinetics and transport in the electrolyte that influences the observed morphologies, such as dendrites on lithium metal anodes or corrosion pits in structural alloys. In this dissertation, the effects of ionic transport in the electrolyte and variable reaction kinetics along the electrode/electrolyte interface on the morphological evolution of the electrode are examined via continuum-scale modeling at a variety of length scales and dimensionalities. Two applications are studied: the electrodeposition and electrodissolution of metal battery anodes, and the corrosion of structural metals. Preliminary studies are also included for a reduced-order model of lithium symmetric cells and a diffuse-interface model of the mechanical response of decomposed mixed-conducting protection layers for lithium anodes.

For the electrodeposition and electrodissolution of metal anodes, a one-dimensional model that considers electrochemistry is developed for two-electrode (i.e., a coin cell) and pseudo-three-electrode (i.e., a beaker cell) systems. The model employs existing mean-field approximations of charge transport and electrostatics in the electrolyte, but a novel, morphology-aware expression is developed to capture the coarse-grained effects of nucleation and surface morphology on the reaction kinetics. The model implementation is heavily optimized to allow high-throughput determination of the physical parameters associated with electrodes and

electrolytes. The model is first demonstrated for the parameterization of the kinetic and transport properties of the $Mg(BH_4)_2$ electrolyte against an experimental cyclic voltammogram. The model is then validated by comparing the predicted voltammetric behavior to experimental results for different potential scan rates. Next, the model is extended to study dendrite formation on lithium anodes. The simulation results indicate that the morphological evolution due to preferential deposition and dissolution of dendrites affects the galvanostatic polarization of a lithium symmetric cell. Combined, the studies of magnesium and lithium anodes demonstrate that the proposed coarse-grained model captures key features of the morphological evolution on the anode surface without the computational cost associated with multidimensional simulations. The final study considers corrosion of structural metals such as stainless steel and aluminum. A multidimensional phase-field approach is coupled with a multicomponent diffusion model and a new microscopic expression for the limiting reaction kinetics to study the evolving microstructure during corrosion. Simulations are performed to examine how the interfacial electrolyte composition, electrostatic potential, and local reaction kinetics influence the evolution of morphological features such as pitting on the metal surface. The new model allows for regions of the electrode surface to experience different kinetic regimes and exhibits improved agreement against experimental data as compared to previous models. Additionally, preliminary results are presented for a reduced-order implementation of the morphology-aware electrode/electrolyte model as well as an examination of the chemo-mechanical behavior of protection layers for lithium-metal anodes. The models developed in this dissertation are flexible and extensible and can be utilized to design and optimize other emerging electrochemical systems and contribute to a quantitative understanding of the behavior of electrode/electrolyte interfaces.

Chapter 1.

Introduction

Context and Motivation

Electrochemical processes are ubiquitous in the world around us and directly impact our daily lives. Some electrochemical processes enable technological applications; for example, many of us have devices powered by a lithium-ion battery (LIB), and rechargeable batteries have allowed society to move toward more renewable energy sources. As of 2016, cumulative global sales of electric vehicles had surpassed two million and could exceed 220 million by 2030.[1] Additionally, the decreasing cost of battery energy storage systems will allow them to become highly competitive with pumped hydro and compressed air energy storage for grid applications without their associated geographic limitations.[2]

However, there are many electrochemical processes that are deleterious in nature. Most notably, the corrosion of materials and the associated cost to replace degraded components is estimated to consume $2.5 trillion annually, or about 3.4% of global gross domestic product.[3] If already-existing corrosion controls were uniformly implemented, a savings of up to $875 billion could be realized, but further development is needed to drive this figure even higher.[3] Corrosion poses a safety risk in structural applications, as the associated loss of material can reduce the mechanical integrity to a point where failure can occur, such as in the 2007 collapse of the I-35W bridge in Minneapolis.[4] Safety is also a key concern in LIBs; under adverse environmental conditions or during overcharge, lithium metal dendrites can form on the surface of the graphite

anode typically employed in the battery.[5] Dendrites can potentially penetrate the polymer separator in the cell and short the battery, possibly causing a fire.

Beyond safety, there are areas where improvements could be implemented to increase the practicality of batteries as an energy storage medium. For electric vehicles (EVs), battery packs are typically assembled from hundreds or thousands of individual cells; for example, the 85 kWh pack in a Tesla Model S is composed of around 7,100 cells.[6] Each cell, which has the 18650 form-factor, weighs about 46.5 g and has a volume of about 70 cm^3,[7] and thus the entire pack contains about 330 kg of batteries that occupy 0.5 m^3 of space. Neglecting the remaining pack components, this represents a significant amount of volume and weight in the overall vehicle. Part of this considerable size of the cell arises from the use of a graphite anode in LIBs. Graphite anodes have theoretical capacities of about 370 mAh/g or 760 mAh/cm^3;[8] in practice, the usable capacity is significantly less.[9] Replacing the graphite with a metallic anode—such as lithium metal—could lead to tenfold and threefold improvements in the theoretical specific and volumetric capacities of the anode, respectively.[8] This could lead to a significant reduction in the size and weight of battery packs. However, long-term sustainability is a key concern for lithium-based battery technologies; electrifying 800 million vehicles with 15 kWh battery packs (smaller than many EV packs currently available) would consume around 30% of the known worldwide supply of lithium.[10] Therefore, significant research has been performed to study other metal anode materials that offer competitive capacities while being more earth-abundant, such as sodium, magnesium, zinc, and other mono- and multivalent metals.[11,12]

Fundamentally, one of the key factors in the electrochemical behavior behind metal anodes and corrosion is that, over time, the morphology of the metal surface evolves. For metal-anode batteries, metal is deposited on the anode surface during charging and dissolved during

discharge. Lithium has a tendency to form dendrites during deposition,[13,14] while magnesium exhibits widely-varying morphologies due to local passivation of the anode surface.[15] Examples of observed metal-anode microstructures are shown in Figure 1.1. Beyond the previously-mentioned safety concerns, the constant formation of additional surface area on the anode leads to breakdown of the liquid electrolyte to form a solid-electrolyte interphase (SEI) layer on the anode.[11,16] While the SEI is believed to help stabilize the deposition and dissolution processes on the anode, over time its formation can consume all of the electrolyte in the battery, reducing the battery lifetime.[11] For corrosion, the formation of pits and other flaws on the metal surface influence the lifetime over which a component can be safely used, as the pits act as stress concentrators and initiation sites for cracks.[17] The rate at which corrosion occurs depends on multiple factors, including the conditions of the operating environment as well as the composition and morphology of the metal alloy. Typical artificially grown corrosion pits in 304 stainless steel as observed by Ghahari *et al.*[18] are presented in Figure 1.2.

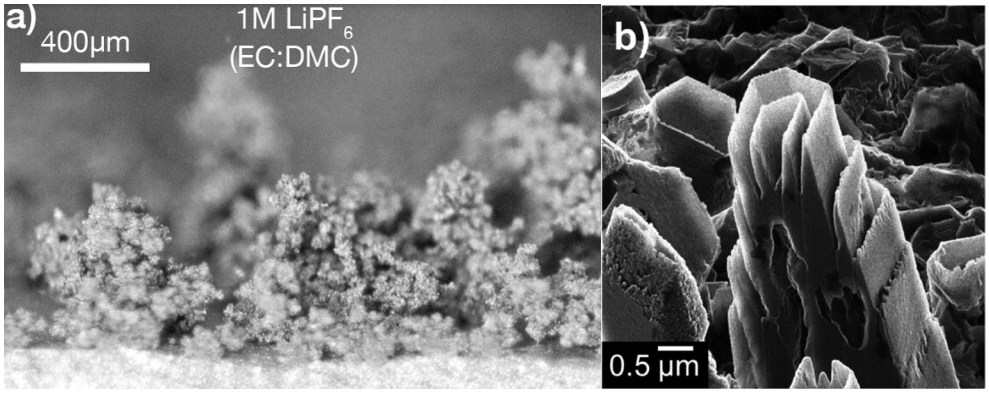

Figure 1.1. Examples of morphologies observed during cycling of metal battery anodes. Left: formation of "mossy" dendrites on a lithium anode during galvanostatic deposition. Adapted with permission from K.N. Wood *et al.*, *ACS Cent. Sci.*, 2, 790–801 (**2016**). Copyright 2016 American Chemical Society.[14] Right: surface structures on a magnesium anode after 20 potentiostatic deposition/dissolution cycles. Adapted with permission from D.J. Wetzel *et al.*, *ACS Appl. Mater. Interfaces*, 7, 18406-18414 (**2015**). Copyright 2015 American Chemical Society.[15]

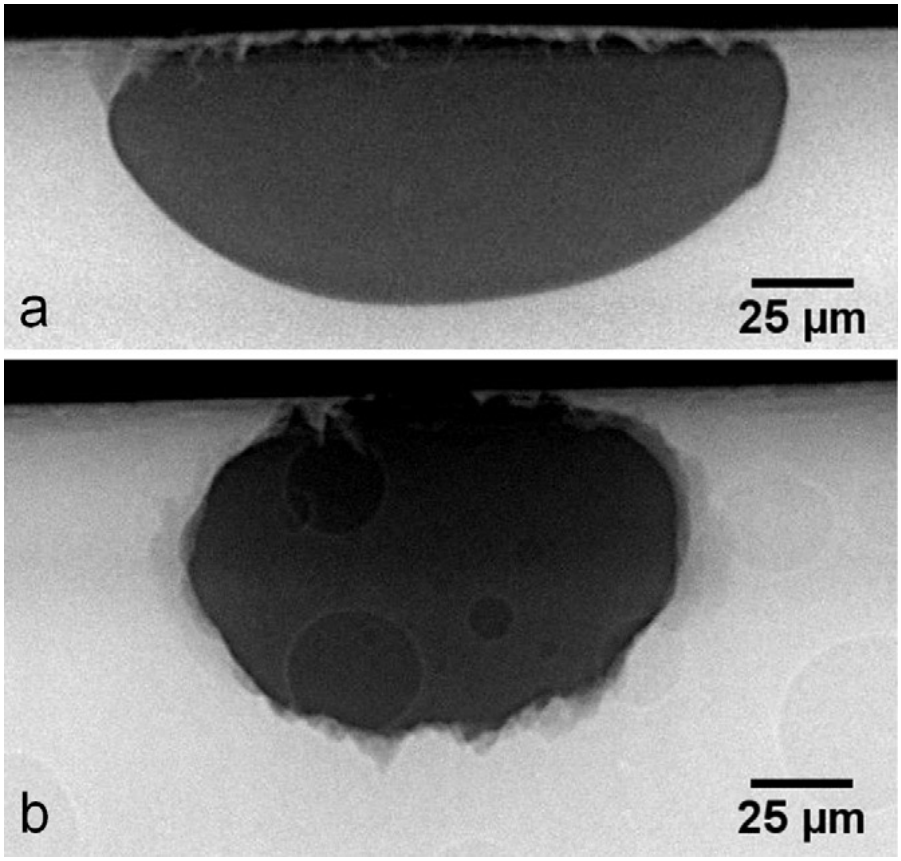

Figure 1.2. Corrosion pits in foils of 304 stainless steel observed by synchrotron X-ray radiography under (a) potentiostatic conditions of 600 mV vs. Ag/AgCl and (b) galvanostatic conditions of 10 µA. Reproduced with permission from M. Gahahari *et al.*, *Corrosion Sci.*, 100, 23-35 (**2015**). Copyright 2015 the Authors.[18]

Unfortunately, for physical and practical reasons it is not always possible to directly observe the evolution of the electrode morphology. First, the length scales involved in these electrochemical systems are diverse. The surface features that have been described thus far range in size from tens of nanometers to a few microns. The active area of the electrode could have dimensions in the millimeter range, and in turn it could be part of a larger cell or structural component that is on the order of centimeters or even larger. Second, there is a similarly wide range of relevant time scales. A battery may be charged and discharged over a few minutes to many hours. Conversely, a structural component may be in service for many years or decades because corrosion rates are slow under open-circuit conditions. Third, there are multiple concurrent processes that may occur in an electrochemical system. In addition to the deposition

and dissolution reactions, there will be a net flux of metal ions to and from the electrode surface into the electrolyte. The movement of these charged species in the electrolyte can induce gradients in the electrostatic potential, which further influences the rate of the overall reactions. Additionally, mechanical stresses may form in the system due to applied loads or misfit strains in the microstructure. If there is a significant amount of flow in the electrolyte, convection and hydrodynamic effects may become significant.

Thus, the interplay of physical processes that influence the time-dependent behavior of the electrode morphology form a richly complex physical problem with many degrees of freedom. Therefore, it is quite common to study these systems via a wide range of simulation and modeling techniques. These approaches can include atomistic-level tools such as density functional theory (DFT) and molecular dynamics (MD),[19–24] stochastic techniques such as Monte Carlo (MC),[25,26] and continuum-scale methods,[27] each of which have associated advantages for electrochemical studies. In this dissertation, the primary focus will be continuum-scale techniques, which can be applied to a broad range of systems with a large range of time and length scales, but neglect the behavior of individual atoms and particles.[27,28] Instead, these techniques capture the average response of the system, and therefore coarse-grained descriptions of the behavior at lower time and length scales are employed to enable efficient simulations of a given system. Consequently, models typically have to be tailored for specific applications.

Dissertation Overview

In this dissertation two examples of electrochemical systems are considered where the electrode morphology evolves over time: deposition and dissolution for metal battery anodes and the pitting corrosion of metal alloys. To study these systems, two distinct continuum-scale modeling frameworks will be presented. The first is a one-dimensional (1D) sharp-interface model that

employs a novel coarse-grained approach to incorporate surface morphologies into a high-throughput framework for simulating voltammetric behaviors of metal anode materials. The second is a two-dimensional (2D) diffuse-interface model that combines the phase-field and smoothed boundary methods to study how variations in morphology, concentrations, potentials, and reaction kinetics impact the evolution of a metal surface undergoing pitting corrosion. These models are validated against experimental results and are employed to develop a deeper understanding of how metal-electrode/electrolyte interfaces evolve over time. Additionally, the preliminary results are presented for two other studies: a reduced-order version of the 1D framework that examines the overall importance of considering transport in the electrolyte, and a model of the mechanical interactions between lithium anodes and decomposed anode protection layers.

The dissertation is divided into eight chapters: (1) Introduction, (2) Background, (3) a Computational Model of Magnesium Deposition and Dissolution for Property Determination via Cyclic Voltammetry, (4) One-Dimensional Model of Lithium Symmetric Cells Under Galvanostatic Conditions, (5) Numerical Modeling of Localized Corrosion Using Phase-Field and Smoothed Boundary Methods, (6) Preliminary Work: Reduced-Order Modeling of Lithium Symmetric Cells, (7) Preliminary Work: Mechanical Interactions Between Decomposed Protection Layers and Lithium Anodes, and (8) Summary and Future Work. Throughout the following chapters, the goal will be to answer the following open questions:

1. For the 1D model, when an electrode has multiple possible deposition and dissolution reactions occurring simultaneously, can the overall current through the electrode be described as a combination of the average behaviors of each reaction?

2. Does the kinetic behavior predicted by this coarse-grained approximation agree with experimentally-obtained voltammetric data?
3. Can the simulation results provide insight into how the kinetic pathways on the electrode surface are changing over time as the surface evolves?
4. For novel anode and electrolyte combinations, can the 1D model quantify the kinetic and transport properties of the system, even with limited experimental input?
5. For the 1D and 2D models, how do the operating conditions of an electrode/electrolyte system affect the morphological evolution and the observed reaction kinetics?
6. How strongly do variations in the diffusion and migration within an electrolyte affect the reaction kinetics along a metal electrode surface?
7. Can generalized modeling frameworks be developed that answer these questions in an efficient manner?

Chapter 2 describes relevant background material for understanding the models developed in this dissertation, including fundamentals of electrochemical transport and kinetics, and an overview of existing numerical models for deposition, dissolution, corrosion, and the effects of mechanics.

Next, Chapter 3 presents the initial derivation and implementation of the 1D morphology-aware modeling framework. This includes the theoretical development of the coarse-grained approximation of the electrode surface and how it is incorporated into a Butler-Volmer-type kinetic model,[29–32] which is frequently employed to describe electrochemical-reaction kinetics. The framework is then applied to study the cyclic voltammetry of magnesium deposition and dissolution from a $Mg(BH_4)_2$/DME electrolyte on a noble working electrode. The model is validated by first parameterizing the unknown kinetic and transport properties of the system

against a single experimentally obtained voltammogram. Then, the behavior under different potential scan rates is predicted and compared to other experimental data. The model accuracy is compared against available literature data and the importance of the experimental geometry in accurately applying the model is discussed.

Chapter 4 extends the model of Chapter 3 to consider the behavior of symmetric lithium/lithium cells. This requires including the moving electrode boundaries over time. Additionally, the morphology-aware kinetic model is modified to consider deposition of lithium on a lithium anode. The model is fitted to experimentally obtained galvanostatic voltage traces and a parametric study is performed. Combined, the simulation results provide insight into how the preferred reaction pathway on the electrode surface changes over time and what parameters determine the shape of characteristic features in the cell polarization behavior.

Chapter 5 presents a phase-field/smoothed boundary method (PF/SBM) framework for simulating pitting corrosion by extending a modeling framework that was developed for microstructural simulation of battery electrodes during charge and discharge.[33,34] Within this chapter, a generalized polycrystalline phase-field method is developed so that the microstructure of a metal evolves due to the presence of a source term at the metal/electrolyte interface. This source term is coupled to the reaction kinetics along the interface by employing the smoothed boundary method to solve for ionic transport in the electrolyte. The model is then demonstrated by directly simulating the effects of IR-controlled reaction kinetics on the corrosion of the metal, which has not been extensively examined by previous modeling efforts. Additional applications of the model are demonstrated for the consideration of anisotropic, polycrystalline microstructures.

Chapter 6 describes preliminary work for a reduced-order model that couples the morphology-aware kinetic model to a semi-analytical solution of transport in the electrolyte to further reduce the computational cost of the framework.

Chapter 7 presents preliminary results for a model with a smoothed boundary formulation of linear elasticity to enable simulations of mechanical interactions between mixed-ionic conducting protection layer materials and lithium metal anodes.

Finally, in Chapter 8 an overall summary of the dissertation is presented along with possible future extensions of the modeling frameworks.

Chapter 2.

Background

In this chapter,* we provide a general overview of the governing equations employed in typical models of electrochemical systems. We also discuss existing models that have been described in the literature for studying deposition and dissolution for batteries and corrosion as well as for including the effects of mechanical behavior.

In Chapter 1, we discussed how electrochemical reactions have fundamentally different consequences for metal battery anodes and corrosion, but there are many similarities in the physical behavior of these systems. At a minimum, an electrochemical cell consists of two electrodes which are separated by an ionically conductive electrolyte and are connected by an electronically conductive circuit.[35] For a rechargeable metal anode battery, during discharge metal cations and electrons are formed at the anode surface.[9] The cations are then transported across the electrolyte, where they then intercalate into the cathode's crystal structure or undergo a conversion reaction with species present in the cathode. The electrons flow through the device that is being powered by the battery and are then consumed at the cathode. For aqueous corrosion, the anode, cathode, and electronic pathway are typically all the same continuous piece

*Portions of the material in this chapter are adapted from A.F. Chadwick, G. Vardar, S. DeWitt, A.E.S. Sleightholme, C.W. Monroe, D.J. Siegel, and K. Thornton, "Computational Model of Magnesium Deposition and Dissolution for Property Determination via Cyclic Voltammetry," *J. Electrochem. Soc.*, 163 (**2016**) A1813; K.N. Wood, E. Kazyak, A.F. Chadwick, K.-H. Chen, J.-G. Zhang, K. Thornton, and N.P. Dasgupta, "Dendrites and Pits: Untangling the Complex Behavior of Lithium Metal Anodes through Operando Video Microscopy," *ACS Cent. Sci.*, 2 (**2016**) 790; and A.F. Chadwick, J.A. Stewart, R.A. Enrique, S. Du, and K. Thornton, "Numerical Modeling of Localized Corrosion Using Phase-Field and Smoothed Boundary Methods," *J. Electrochem. Soc.*, 165 (**2018**) C633.

of metal, and the aqueous solution in contact with the metal serves as the ionically conductive electrolyte.[36] The anode and cathode may be completely dissimilar metals that are connected together, or in metal alloys they can be different phases of the given alloy system with different equilibrium reaction potentials. Unlike a rechargeable battery, the reactions at the cathodic surface often do not involve the cationic species produced at the anode. Instead, hydrogen ions can be reduced to produce hydrogen gas or oxygen gas can be reduced to produce hydroxide ions. Due to the similarities between these processes, many models of batteries and corrosion share similar features.

Governing Equations

For a solution of ions in an electrolyte, each species has an associated electrochemical potential:[35,37]

$$\bar{\mu}_i = \mu_i^0 + RT \ln a_i + z_i F \Phi, \tag{2.1}$$

where $\bar{\mu}_i$ is the electrochemical potential of species i, μ_i^0 is the chemical potential at a standard reference state, R is the ideal gas constant, T is the absolute temperature, a_i is the activity of the species, z_i is its charge, F is Faraday's constant, and Φ is the local electrostatic potential in the electrolyte. When there is a gradient in the activity of a species or in the electrostatic potential, the corresponding gradient in $\bar{\mu}_i$ will lead to an overall flux of the i-th species:[35,37]

$$\mathbf{N}_i = -u_i c_i \nabla \bar{\mu}_i, \tag{2.2}$$

where $\mathbf{N}_i$ is the vector flux of the species, u_i is its electrochemical mobility, and c_i is its concentration. When there is an imbalance in the flux at a given point, there will be an evolution in the concentration of the species over time:

$$\frac{\partial c_i}{\partial t} = -\nabla \cdot \mathbf{N}_i = \nabla \cdot (u_i c_i \nabla \bar{\mu}_i), \tag{2.3}$$

where t is time. Equation 2.3 represents the fundamental equation by which much of electrochemical transport can be described. As written, Eq. 2.3 is applicable to so-called moderately dilute solutions.[35] In the limit of a dilute solution, the activity of a species is roughly equal to its concentration, which when combined with the Nernst-Einstein relationship[35,37] allows for Eq. 2.2 to be rewritten as:

$$\mathbf{N}_i = -D_i \nabla c_i - z_i \frac{F}{RT} D_i c_i \nabla \Phi, \tag{2.4}$$

which is the Nernst-Planck equation. [38–40] The two terms on the right-hand side correspond to the diffusion and migration contributions to the species flux. Equation 2.3 then becomes:

$$\frac{\partial c_i}{\partial t} = -\nabla \cdot \mathbf{N}_i = \nabla \cdot \left(D_i \nabla c_i + z_i \frac{F}{RT} D_i c_i \nabla \Phi \right). \tag{2.5}$$

For neutral species, Eqs. 2.4 and 2.5 reduce to Fick's first and second laws of diffusion.

To fully solve Eq. 2.5, it is necessary to describe the electrostatic potential. From a fundamental level, this can be achieved with the Poisson equation:[35]

$$\nabla^2 \Phi = -\frac{\rho}{\epsilon_s \epsilon_0}, \tag{2.6}$$

where $\rho = F \sum z_i c_i$ is the local charge density, ϵ_s is the dielectric constant of the solvent, and ϵ_0 is the vacuum permittivity. Together, Eqs. 2.4 and 2.6 are frequently referred to as the Poisson-Nernst-Planck (PNP) system of equations. The total current can be obtained by summing the product of the species' charge and flux:

$$\mathbf{i} = F \sum_{i=1}^{n} z_i \mathbf{N}_i = -F \sum_{i=1}^{n} z_i D_i \nabla c_i - \frac{F^2}{RT} \sum_{i=1}^{n} z_i^2 D_i c_i \nabla \Phi, \tag{2.7}$$

where $\mathbf{i}$ is the vector current density in the electrolyte, n is the number of species in the electrolyte, and the first term on the right-hand side of Eq. 2.7 is commonly referred to as the

diffusion current.[35] Similarly, the rate of change of the charge density can be obtained by summing the product of the species' charge and the rate of change for their concentration:

$$\frac{\partial \rho}{\partial t} = F \sum_{i=1}^{n} \left(z_i \frac{\partial c_i}{\partial t} \right) = \nabla \cdot \left[F \sum_{i=1}^{n} z_i D_i \nabla c_i + \frac{F^2}{RT} \sum_{i=1}^{n} z_i^2 D_i c_i \nabla \Phi \right]. \tag{2.8}$$

Various simplifications have been made in order to solve the PNP equations. In analytical electrochemical studies, supporting species are added to the electrolyte to increase the ionic conductivity, as then the reacting species only caries a fraction of the overall current.[37] This allows for Eq. 2.4 and 2.5 to be replaced with Fick's laws, which has permitted well-known analytical solutions such as Cottrell's equation for chronoamperometry[41] and Nicholson and Shain's methodology for cyclic voltammetry.[42,43] However, these methodologies do not account for the mass transfer to and from the electrode surface that is inherent to deposition and dissolution, and battery electrolytes do not employ supporting electrolytes. Thus, such approaches violate our requirement for generality and are not considered in the remaining portions of this dissertation.

In their early work, both Nernst[44] and Planck[38,39] introduced what has come to be known as the electroneutrality approximation. This approximation assumes that the small permittivities of typical solvents cause any charge separation that occurs to be screened over a vanishingly thin Debye length when compared to typical experimental length scales.[45] Therefore Eq. 2.6 can be replaced by:

$$\rho = \sum_{i=1}^{n} z_i c_i = 0. \tag{2.9}$$

The electroneutrality approximation, when inserted into Eqs. 2.6 through 2.8, implies that Φ satisfies Laplace's equation and that the current density is divergence-free. However, directly solving Laplace's equation is not guaranteed to converge due to the degeneracy of possible

solutions.[35] Instead, Eq. 2.9 is employed to solve for one charged species concentration in terms of the remaining concentrations, and Φ can be obtained by solving:

$$\nabla \cdot \left[F \sum_{i=1}^{n-1} z_i (D_i - D_n) \nabla c_i + \frac{F^2}{RT} \sum_{i=1}^{n-1} z_i (z_i D_i - z_n D_n) c_i \nabla \Phi \right] = 0, \tag{2.10}$$

where the concentration of the n-th species has been eliminated by electroneutrality, reducing the degrees of freedom by one.

At the electrode surface, some species in the electrolyte will react, and charge and mass will be transferred between the electrolyte and the electrode. Multiple models have been proposed for the rate of this reaction, but the most commonly employed description is perhaps the Butler-Volmer equation:[29–32,35,37]

$$i = i_0 \left[\exp\left(\frac{\alpha_a F}{RT} \eta \right) - \exp\left(-\frac{\alpha_c F}{RT} \eta \right) \right], \tag{2.11}$$

where i is the current density, i_0 is the exchange current density, α_a and α_c are the charge transfer coefficients of the anodic and cathodic reactions, respectively, and η is the overpotential that drives the reaction. The exact values of i_0, α_a, and α_c are typically assumed to be constants for a given reaction and system, but they frequently depend upon the concentrations of the reactants. The overpotential can be expressed as $\eta = V_a - E^{0'} - \Phi_0$, where V_a is the applied potential at the electrode surface, $E^{0'}$ is the formal potential, and Φ_0 is the electrostatic potential in the electrolyte immediately adjacent to the electrode surface. When the magnitude of the overpotential is large, either the anodic or cathodic reaction will be dominant. For $\eta \gg 0$, Eq. 2.11 can be rewritten as:

$$\ln i = \ln i_0 + \frac{\alpha_a F}{RT} \eta, \tag{2.12}$$

and when $\eta \ll 0$:

$$\ln(-i) = \ln i_0 - \frac{\alpha_c F}{RT}\eta. \tag{2.13}$$

Respectively, Eqs. 2.12 and 2.13 are known as the anodic and cathodic Tafel equations.[35–37]

Existing Modeling Approaches

Models of Transport and Kinetics Without Deposition or Dissolution

As opposed to the analytical solutions described above, there has been more of an interest to directly simulate the effects of migration in theoretical electrochemistry, particularly in open channels of electrolyte. Early attempts by Cohen and Cooley[46] and Sandifer and Buck[47] described models that replaced the Poisson equation with a current expression that included a displacement current:

$$\mathbf{i} = F\sum_{i=1}^{n} z_i \mathbf{N}_i + \epsilon_s \epsilon_0 \frac{\partial \mathbf{E}}{\partial t}, \tag{2.14}$$

where $\mathbf{E} = \nabla\Phi$ is the electric field. The reason for this approach was that Eq. 2.14 was more practical to simulate with computational resources available at the time. The limitation of these models[46,47] is that they employed explicit finite difference methods (FDMs), which due to the mathematical stiffness of the governing equations restricted the models to small time step sizes. Brumleve and Buck[48] noted that the limitation to small time steps made simulations expensive and implemented a fully implicit FDM to allow larger time steps, using Newton-Raphson iteration to solve the Nernst-Planck and displacement-current equations simultaneously. Implicit methods are now implemented in many models of analytical electrochemistry. Streeter and Compton[49] and Dickinson *et al.*[50] employed a similar method to study weakly supported potential-step experiments and cyclic voltammetry (CV), respectively. The results from these two models led Dickinson *et al.*[45] to perform an examination of why the electrochemical

modeling community would preferentially choose either the Poisson equation or electroneutrality. Their chief conclusion was that both approaches usually produce identical results, and that on modern computer hardware there are no significant differences in the numerical cost of one versus the other, nor does one confer an increased level of numerical stability.

Early models of transport in corrosion typically employed the electroneutrality to solve for the pseudo-steady-state current in artificial corrosion pits under diffusion-limited conditions. Tester and Isaacs[51] developed a model to examine common-ion effects on measured currents in corrosion pits but assumed that the effects of migration could be accounted for in an effective diffusivity of the electrolyte species. Galvele[52] employed a similar approach when modeling the effect of transport on the stability of corrosion pits. Sharland and Tasker[53,54] developed a model to directly consider the effects of migration on the local solution chemistry in a corrosion pit. However, as will be discussed below, more recent models of corrosion have been focused on including the effects of the moving corrosion boundary.

Models have also been developed to describe the coupled effects of transport and kinetics without considering the effects of deposition and dissolution, but within porous media instead of open channels. One of the most significant models is porous electrode theory (PET), which was initially developed by Euler and Nonnenmacher[55] and then generalized by Newman and Tobias.[56] PET was subsequently extended to consider impedance studies by de Levie.[57] In PET, the transport of electrolyte species and the resulting current distribution are described through a volume-averaged approach that considers two separate current distributions for the transport and reaction kinetics. Newman and Tiedemann[58] subsequently developed PET for applications to battery electrodes. Further extension of Newman and Tiedemann's method led to the

development of what is perhaps the most well-known modeling approach for batteries, and in particular LIBs, the pseudo-two-dimensional (P2D) model[59–61] described by Newman and coauthors. The P2D model's contributions to understanding LIB behavior have been dramatic, and the initial version of the model described by Doyle *et al.*[59] is one of the most-cited papers in the battery modeling field. The P2D model assumes electroneutrality and employs what is known as concentrated solution theory,[35] specifically a Stefan-Maxwell approach for multicomponent diffusion. However, when activity coefficients and transference numbers remain constant, the P2D model essentially reproduces dilute solution theory. Thus, when developing the models presented in Chapter 3 and Chapter 4 we will employ transport descriptions in the dilute solution limit. Typically, applications of PET and the P2D model have neglected the effects of deposition and dissolution.

In this dissertation, some of the developed models will employ electroneutrality, while others solve the Poisson equation. None of the models presented here consider transport in porous media. It should be noted, though, that as a mean field approximation the Poisson equation fails when applied to one-dimensional (1D) studies of transport in porous, tortuous media.[62] Instead, a rigorous homogenization must be performed that results in a tensorial description of the permittivity. However, the electroneutrality approximation is not subject to this limitation, and thus any future extensions of the 1D model in this dissertation to study porous media will need to change from the Poisson equation to electroneutrality.

Models of Deposition and Dissolution

Several models have been proposed to primarily simulate the kinetics of electrodeposition of metals. Wheeler *et al.*[63] employed the level-set method in two dimensions to examine the deposition of copper and to track the location of the metal/electrolyte interface, the movement of

which was governed by Butler-Volmer kinetics. Guyer *et al.*[64,65] first derived a fully variational, thermodynamically consistent phase-field model of electrodeposition that recovered nonlinear Butler-Volmer kinetics and the Gouy-Chapman-Stern model of the electrochemical double layer. However, this required very fine resolution in the numerical mesh and small simulation time step sizes, which made the model impractically expensive beyond one-dimensional studies. A modification of this approach by Deng *et al.*[66] was proposed to study the formation of surface layers in lithium-ion batteries, but it was similarly limited to a single dimension due to computational cost.

Other variationally derived phase-field models of deposition and dissolution, such as Shibuta *et al.*,[67] Liang *et al.*[68] and Liang and Chen,[69] have improved computational efficiency by simplifying the physics, typically by neglecting the effects of charge separation, the double layer, the diffusion potential, and/or the formation of concentration gradients. Cogswell[70] achieved a significant improvement in computational efficiency by employing a nonvariational approach within the thin-interface limit to enable efficient simulations of dendritic deposition of zinc. Cogswell's model also incorporated nonlinear Marcus-Hush-Chidsey kinetics. Ely *et al.*[71] derived a phase-field model for lithium deposition where the phase-field and electrostatic potential evolved via coupling of the fields through source terms at the solid/electrolyte interface. However, the effects of evolving non-uniform concentrations of ions in the electrolyte were neglected. DeWitt *et al.*[33] implemented a phase-field method of faceted magnesium electrodeposition and electrodissolution where the solid was represented by an order parameter that evolved according to Cahn-Hilliard[72] (i.e., conserved) dynamics. The interfacial velocity was given by a source term at the solid/liquid interface that coupled the reaction kinetics with electrochemical transport in the electrolyte, which was solved using the smoothed boundary

method.[73] This allowed for facile inclusion of anisotropic, spatially varying reaction kinetics in a computationally efficient framework. Enrique *et al.*[34] generalized the method of DeWitt *et al.*[33] to study the morphological evolution of lithium-metal electrode during electrodeposition. An additional order parameter, evolved by Allen-Cahn[74] (nonconserved) dynamics, was used to represent the electrolyte. An example of the microstructures considered by Enrique *et al.* is shown in Figure 2.1.

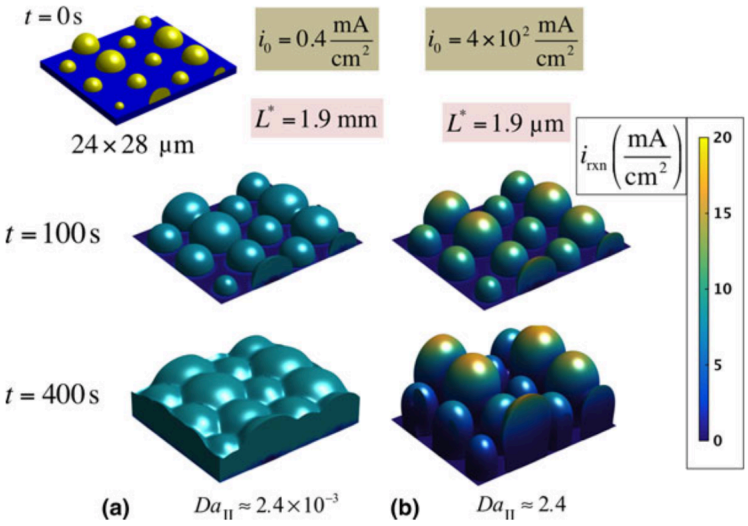

Figure 2.1. Simulated morphologies of dendritic lithium features, demonstrating how increased reaction kinetics along the deposit surfaces leads to morphological instability. Reproduced with permission from R.A. Enrique *et al.*, *MRS Commun.,* 7, 658-663 (**2017**). Copyright 2017 Materials Research Society.[34]

Models of Corrosion

Scheiner and Hellmich[75,76] developed a moving-boundary finite volume method (FVM) model for pitting corrosion in stainless steel that solved the diffusion equation for an effective ion within the electrolyte. Their model produced generally good agreement with experimental data by considering Tafel kinetics to describe the interfacial velocity at a constant overpotential. However, as the authors point out, the lack of electrostatic migration in the electrolyte produced an abrupt transition between activation- and diffusion-controlled conditions that is not observed experimentally. Other models have also employed the approximations of only considering

diffusion in the Tafel regime with a variety of numerical methods. These include Duddu,[77] who employed an extended finite element method (XFEM), Chen and Bobaru,[78] who employed a peridynamic model, and Mai *et al.,*[79] who proposed a model based on the Kim-Kim-Suzuki (KKS) phase-field formulation. Notably, the latter two of these models[78,79] were able to smoothly capture the transition between activation- and diffusion-controlled conditions. The peridynamic approach has also been utilized by Chen *et al.*[80] to simulate the effects of new diffusion pathways through the cover over the corrosion pit as it becomes increasingly perforated. However, the models from Mai *et al.*[79] and Chen *et al.*[78,80] did not consider orientation-dependent kinetics, as demonstrated in Figure 2.2.

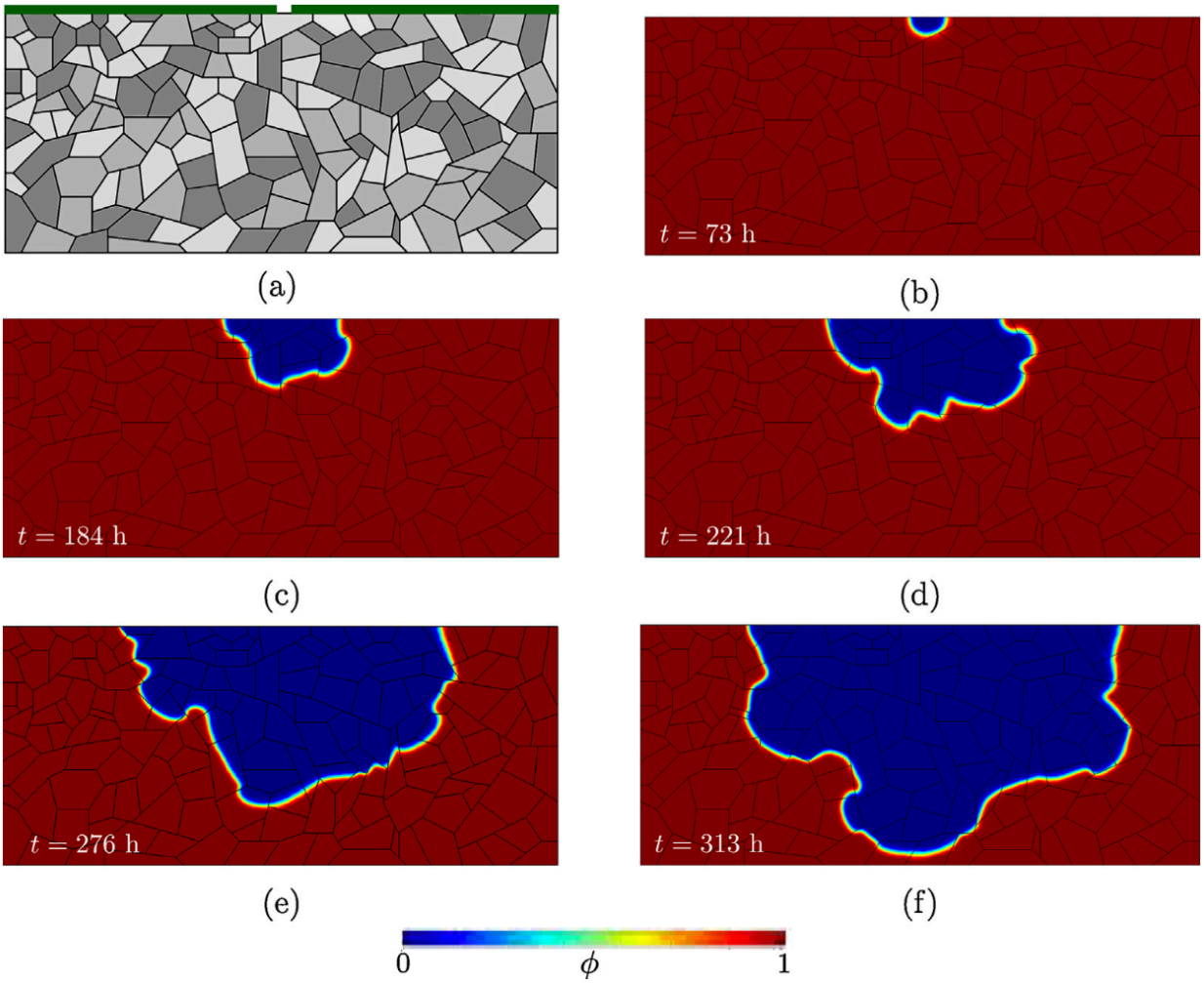

Figure 2.2. A simulation of pitting corrosion in a stainless steel microstructure performed by Mai *et al.* While the model included variations in corrosion kinetics arising from varying crystallographic orientation, this was implemented by assigning different corrosion current densities to three orientations and each grain was assigned one of these orientations and its corresponding current density to the entirety of the grain. Thus, their model did not include true orientation-dependent reaction kinetics, and faceting of the microstructure was therefore not observed. Reproduced with permission from W. Mai *et al.*, *Corrosion Sci.*, 110, 157-166 (**2016**). Copyright 2016 Elsevier.[79]

Other models have been proposed to include the effects of electrostatic migration. Laycock and White[81] developed a finite element method (FEM) approach to simulate pit propagation in a stainless steel that qualitatively agreed with experimental results but only examined short time scales. Deshpande[82] employed an arbitrary Lagrangian-Eulerian finite element moving mesh method (ALE-FEM) to simulate preferential corrosion in a Mg-Al alloy where the interfacial kinetics was parameterized with experimental polarization data. However,

the electrolyte was assumed to be well-stirred and only Laplace's equation was solved to determine the electrostatic potential and current density. This simplification neglects the effects that concentration variations can have on both the ionic conductivity in the electrolyte and the reaction rates. Yin *et al.*[83] implemented a similar ALE-FEM framework to simulate corrosion of Al near a cathodic particle with and without blocking effects from compound formation on the corroding pit interface. Their model employed experimental polarization data to calculate the electrode potential and the overall current density through the metal surface, but the simulations were performed in two dimensions and were limited to one cathodic particle. Duddu *et al.*[84] added the ability to solve for the electrostatic potential in the electrolyte to Duddu's[77] XFEM model, however this work neglected the effects of the moving boundary, which represents a significant simplification of the system. More recently, Mai and Soghrati[85] modified their phase-field model to include the effects of the electrostatic potential. This study considered the transport of multiple species, but the influence of varying conductivity within the pit solution was only considered for small cell polarizations. Furthermore, polarization was only accounted for at stationary interfaces (i.e., cathodic surfaces) and neglected along the corroding metal/electrolyte interface. Jafarzadeh *et al.*[86] considered the effects of the potential by including a correction for the applied potential based on estimates of the bulk solution resistance. The correction to the potential was obtained in a previous study[87] by fitting a function to an FEM simulation result based on the experimental cell geometry. While this approach improved agreement with experimental results, the decoupling of the potential from the corrosion physics introduces an additional step where the phenomenological relationship must be obtained for any given experimental geometry prior to simulation, and it also requires an assumption of constant conductivity.

Models of Mechanical Behavior

Modeling of the effects of mechanical behavior for both battery materials and corrosion has attracted a fair amount of interest recently. For batteries, multiple models have been proposed to examine how dendrite growth may be affected by the presence of a mechanically stiff region in contact with the lithium anode, such as a protection layer or a polymer separator. The initial work of Monroe and Newman[88] examined the effect of mechanics on the stability of the lithium anode surface during deposition, determining that the dendritic instability can be suppressed when the separator shear modulus is approximately twice that of lithium. This model has since been examined and extended upon, such as in the work of Ahmad and Viswanathan,[89] which found that the mechanical protection effect strongly depends on the orientation of the anode and protective layers when they are anisotropic. Additionally, Barai *et al*.[90] found that the initial morphology of the lithium surface is critical for exploiting the mechanical protection effect, as when the interface is pre-stressed the shear modulus must be significantly higher to prevent dendrite formation. Studies have also been performed to include effects of mechanical behavior within models derived from the P2D model, such as the work of Ferrese and Newman.[91] Models have also been proposed to study the effects of induced eigenstrains in cathode materials[92,93] and composite silicon anodes.[94] In these models, the formation of a concentration gradient induces a gradient in the inelastic eigenstrain due to changes in the local crystal structure and lattice constants;[95] as the system relaxes, elastic strains form in the cathode. Additionally, the formation of stress has an impact on the long-term microstructural evolution. Particularly in cathode materials, at some critical C-rate the eigenstrain becomes large enough to cause fracture of the material, an event known as electrochemical shock.[96] However, models have not yet been developed to consider how concentration-induced eigenstrains may form in an anode protection

layer and lead to stress in the lithium anode. For corrosion, mechanical behavior is important in understanding stress corrosion cracking and has recently been incorporated into numerical models such as in an extension to the phase-field model of Mai and Soghrati.[97]

Chapter Summary

In this chapter, we presented a brief introduction of the fundamental equations that are considered when modeling the transport of ionic species that is inherent to electrochemical deposition and dissolution as well as corrosion processes. This discussion included descriptions of typical regimes for which solutions are described and the variations in typical approaches for solving the electrostatic potential. Additionally, we presented a review of the literature to discuss existing models of deposition and dissolution, corrosion, and how mechanical behavior is becoming a growing area of interest when simulating these processes for batteries and corrosion.

Chapter 3.

Computational Model of Magnesium Deposition and Dissolution for Property Determination via Cyclic Voltammetry

Introduction

In this chapter,[*] a one-dimensional continuum-scale model is developed to simulate the voltammetry of an electrode/electrolyte system for magnesium metal-anode battery applications. A rechargeable magnesium battery was first demonstrated 25 years ago when Gregory *et al.*[98] showed that magnesium could be reversibly deposited onto and dissolved from a magnesium-metal surface, as well as intercalated into and deintercalated from various host cathodes. Further interest in secondary magnesium batteries arose following the work of Aurbach *et al.,*[99] which demonstrated a highly efficient organohaloaluminate electrolyte using a magnesium anode and a Mo_6S_8 Chevrel-phase cathode. As a battery anode, magnesium metal offers important advantages over both intercalation compounds and lithium metal, including a higher theoretical volumetric energy capacity (3833 mAh/cm^3 vs. 2046 mAh/cm^3 for lithium metal and 760 mAh/cm^3 for graphite-based lithium-ion anodes), as well as a higher abundance in the earth's crust.[8] Additionally, magnesium is less prone to dendrite formation than lithium when electrodeposited and therefore offers potential for improved battery cycle life and safety.[100]

[*]Adapted from A.F. Chadwick, G. Vardar, S. DeWitt, A.E.S. Sleightholme, C.W. Monroe, D.J. Siegel, and K. Thornton, "Computational Model of Magnesium Deposition and Dissolution for Property Determination via Cyclic Voltammetry," *J. Electrochem. Soc.*, 163 (**2016**) A1813.

In addition to high-capacity electrode materials, a practical magnesium battery will also require an efficient electrolyte that is compatible with (i.e., chemically stable in contact with) these electrodes. Compared to lithium electrolytes, magnesium electrolytes remain in a relatively early developmental stage.[8,21,22,33,98–122] Electrolytes formulated from Grignard reagents have been widely studied both in the battery and general electrochemistry communities.[98,119,121,123–128] The speciation of these electrolytes is complex because, in addition to ionic dissociation, the reagents also undergo the Schlenk equilibrium process (a type of ligand exchange) and form multimeric species in many solvents. Both organohaloaluminates and the so-called magnesium aluminum chloride complex (MACC) are electrolyte classes that relate closely to Grignard reagents; both include a Lewis acid, such as $AlCl_3$, to facilitate dissociation and shift the Schlenk equilibrium. Organohaloaluminates are typically of the form RMgX + $AlCl_3$, and MACC is typically of the form $MgCl_2$ + $AlCl_3$.[99,101,104,105,118,122] Due to their halide content, Grignards, organohaloaluminates, and MACC are corrosive to non-noble metal substrates, which presents a challenge to their practical application in batteries.[107] To avoid this problem, inorganic salts such as $Mg(TFSI)_2$ and $Mg(BH_4)_2$ in solutions based on traditional solvents[22,103,108–110,112,113] or ionic liquids[114–117] have also been explored.

Despite the recent growth in efforts to develop efficient magnesium electrolytes, many challenges remain. For example, formation of ion-blocking passivation films on magnesium surfaces and compatibility with cathode materials (allowing reversible intercalation of Mg^{2+}) both remain challenges.[8,15,104,106,112] Development of accurate electrochemical models of magnesium electrolytes, including how they interact with electrodes, could provide the insight needed to guide a search for the optimal electrolyte.

The electrochemical performance of any electrolyte depends strongly on its properties. Pinpointing which parameters most strongly impact performance can be a challenge, however. To date, only limited property values are available in the literature. For example, diffusivities have been reported for an organohaloaluminate in THF[101] and for $Mg(TFSI)_2$, $Mg(BF_4)_2$, and $Mg(BH_4)_2$ in a small number of solvents.[113] Estimates of the nucleation overpotential for magnesium deposition on different metal substrates[100,129,130] have also been presented. Development of a computational model for the plating and stripping of magnesium may be helpful, both to identify currently unexplored properties and to examine how these properties influence performance. If a computationally efficient model was available, it could be employed to obtain the unknown properties of the electrode/electrolyte system by reproducing the experimentally observed voltammetric behavior of the system. While the electrodeposition and electrodissolution models described in Chapter 2 have increased the scientific understanding of the phenomena observed during deposition and dissolution processes, they are commonly limited by high computational cost. This high cost reduces the ability of these models to quickly determine multiple physical properties of the system.

This chapter therefore presents a new continuum-scale model that is computationally inexpensive and can be employed to determine parameters describing both transport dynamics in the liquid electrolyte and interfacial reactions. The model is developed from non-electroneutral dilute-solution theory, using Nernst-Planck equations for the mass flux and Poisson's equation for the electrostatic potential. The electrochemical reaction is modeled with multistep Butler-Volmer kinetics, with a modified current/overpotential relationship that accounts for the portions of the current responsible for nucleating new deposits and growth or dissolution of existing ones. The model is used to simulate cyclic voltammetry of a magnesium borohydride/dimethoxyethane

($Mg(BH_4)_2$/DME) electrolyte on a gold substrate. In the following sections, we formulate the model's governing equations, outline the numerical methods by which these equations are solved, and describe the batch data-processing procedure employed to fit simulated CV curves to experimentally obtained results.[131] Several key properties such as ion diffusivities, heterogeneous rate constants, charge-transfer symmetry factors, nucleation overpotentials, and formal reaction potentials are determined through the fitting process. The fitted model parameters are provided in comparison with available literature data along with a discussion of the general utility of the model. This work demonstrates the model's applicability in parameterizing the electrode and electrolyte properties.

Theory

One common approach to modeling electrochemical systems is to apply dilute solution theory to describe the electrolyte. Generally, this approach involves treating the solvent as a species in great excess and solving the set of equations that govern the material balances for each solute species *i*,

$$\frac{\partial c_i}{\partial t} = -\nabla \cdot \mathbf{N}_i, \tag{3.1}$$

where c_i is the concentration, $\mathbf{N}_i$ the total molar flux (a vector quantity), and t is time. Nernst-Planck equations are adopted as constitutive laws for mass transport,[38–40]

$$\mathbf{N}_i = -D_i \nabla c_i - z_i \frac{F}{RT} D_i c_i \nabla \Phi, \tag{3.2}$$

where D_i is the diffusion coefficient, z_i is the charge, F is Faraday's constant, R is the ideal gas constant, T is the absolute temperature, and ϕ is the local electrostatic potential. We note that the Nernst-Einstein relationship[35] has also been employed to eliminate the electrochemical mobility as a degree of freedom here. The two terms on the right-hand side of Eq. 3.2 correspond to

contributions from diffusion and migration, respectively; it is assumed that convection is negligible in the overall mass transport. Poisson's equation relates the electrostatic potential in the electrolyte to the local charge density, $\rho = F\sum z_i c_i$, as

$$\nabla^2 \Phi = -\frac{\rho}{\epsilon_0 \epsilon_s}, \tag{3.3}$$

where ϵ_0 is the permittivity of free space and ϵ_s is the dielectric constant of the electrolyte.[35] When combined, Eqs. 3.1 through 3.3 form the Poisson-Nernst-Planck (PNP) system of equations.

This work builds upon the methodology of Dickinson *et al.*[50] by extending the interfacial reaction model to account for the nucleation, growth, and dissolution of metal deposits, as well as the experimental Coulombic efficiency. The utility of the model is demonstrated by identifying parameter sets that are consistent with experimentally obtained CV data. With this validation, the model could be employed in the future to determine how parameters may differ between different electrolyte systems that are under consideration for metal-anode battery applications.

Model Formulation

The present methodology derives from the work of Dickinson *et al.*[50] with several modifications, listed below. First, the electrolyte is taken to be unsupported. Second, the overall redox reaction is taken to comprise a sequence of two single-electron transfers, each governed by Butler-Volmer kinetics. Third, mass exchange between the electrolyte and electrode surface is allowed. Fourth, the model includes a description of both the nucleation behavior of magnesium as well as the Coulombic efficiency. Finally, the cell geometry is taken to be planar; this has an advantage in that it makes the ohmic loss between the working and reference electrode more precise, but a disadvantage in that the diffusion boundary layer may extend well into the electrolyte.[35] Within

the present 1D model, the counter electrode is assumed to be sufficiently far away from the reference electrode that the diffusion boundary layer extending from it does not impact the concentration field at the reference electrode during the duration of a CV sweep. In practice, experimental cells must be carefully designed so that these approximations are satisfied.

Since a planar cell was not available, experiments were performed in a standard three-compartment electrochemical cell, and the resulting data were used to parameterize the model. Fitting of data from the three-compartment cell serves to demonstrate the methodology as a proof-of-concept. These promising results will hopefully stimulate interest in performing experiments that correspond to the geometry assumed in simulations.

Model Electrochemical Half-Cell

The model describes an electrochemical half-cell comprising a working electrode (WE), a reference electrode (RE), and a region of electrolyte between them. A 1D model geometry is assumed, which approximates flat planar electrodes separated by a distance that is small in comparison to the size of the electrode surface. This model geometry is similar to those used in many experimental cells for battery material testing, such as coin cells or Swagelok cells. However, such cells would typically not include a reference electrode and would likely have a smaller spacing between the working and counter electrodes than is assumed here.

Magnesium is deposited and dissolved from the WE, which is assumed to be an ideal noble metal that does not participate in the reaction. Initially, we assume that there is no magnesium deposited upon the surface of the WE. A schematic representation of the model system is presented in Figure 3.1. The origin ($x = 0$) of the coordinate system is defined as the interface between the WE or deposited layer and the electrolyte. The surface of the reference electrode (RE) is defined to reside at position $x = L$. The counter electrode is not explicitly

considered in the model; it is assumed that the counter electrode is far enough away from the WE and RE such that it does not influence the response at either electrode. In cases where this assumption is not valid, the model can be modified to account for the counter electrode.

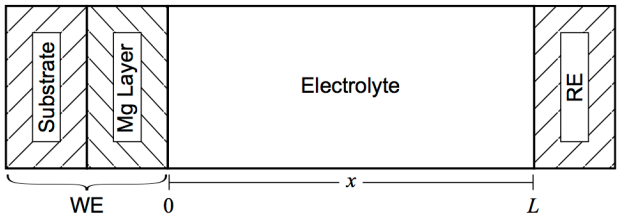

Figure 3.1. A schematic representation of the model domain (not to scale). Within the electrolyte, the concentrations of each electrolyte species are tracked along with the local electrostatic potential. The surface of the working electrode (WE), which is a combination of the substrate and deposited magnesium layer, is at $x = 0$, while the surface of the reference electrode (RE) is at $x = L$.

The electrolyte is assumed to be $Mg(BH_4)_2$ in dimethoxyethane (DME), a member of the glyme series. According to Mohtadi *et al.*,[108] dissociation of the salt in solution is governed by the equilibrium reactions

$$Mg(BH_4)_2 \rightleftharpoons Mg(BH_4)^+ + BH_4^-, \tag{3.4}$$

$$Mg(BH_4)^+ \rightleftharpoons Mg^{2+} + BH_4^-, \tag{3.5}$$

where the equilibrium concentration of each species is determined by K_{d1} and K_{d2}, the respective dissociation constants of Eqs. 3.4 and 3.5. Both K_{d1} and K_{d2}, and therefore the exact species concentrations, are unknown. It is generally believed that other metal borohydride salts exist in solution as a combination of solvated ions as well as solvated ion pairs.[132,133] In addition, Mohtadi *et al.*[108] determined via IR and NMR spectroscopy that while further dissociation occurs in DME than in THF, it is still unlikely that complete dissociation of $Mg(BH_4)_2$ occurs in solution. Here, it is assumed that the salt is mostly dissociated to its constituent ions, but if the actual speciation differs, the approach may require corresponding modifications. It is assumed that the redox couple for the electrodeposition and electrodissolution reaction is composed of two sequential single-electron transfers involving the Mg^{2+} ion produced by Eq. 3.5,

$$\mathrm{Mg}^{2+} + \mathrm{e}^{-} \rightarrow \mathrm{Mg}_{\mathrm{i}}^{+}, \tag{3.6}$$

$$\mathrm{Mg}_{\mathrm{i}}^{+} + \mathrm{e}^{-} \rightarrow \mathrm{Mg}, \tag{3.7}$$

where $\mathrm{Mg}_{\mathrm{i}}^{+}$ is an unstable intermediate. The overall half-reaction is

$$\mathrm{Mg}^{2+} + 2\mathrm{e}^{-} \rightarrow \mathrm{Mg}, \tag{3.8}$$

where metallic magnesium is deposited upon the WE.

Electrolyte Species Concentration and Electrostatic Potential

The model physics are described by the 1D Cartesian forms of Eqs. 3.1 through 3.3. To fully specify the solution of the boundary value problem, it is necessary to define boundary conditions on these equations. At the boundary between the WE and the electrolyte (at $x = 0$), it is assumed that the eventual thickness of the deposited magnesium layer is significantly smaller than the WE/RE separation, and thus it is assumed to be stationary in time. No reactions occur at the boundary between the electrolyte and RE (at $x = L$). The system size, L, is sufficiently large such that the combined diffusion/migration front does not reach the RE at the end of the simulation time. Therefore, rather than assuming a no-flux boundary condition, the concentration of each species can be set to its nominal bulk concentration for simplicity,

$$c_i|_{x=L} = c_{i,\mathrm{bulk}}. \tag{3.9}$$

The boundary condition at the WE surface ($x = 0$) is dependent upon whether or not a given species is involved in the electron transfer reaction. For inert species, a no-flux boundary condition is imposed:

$$N_i|_{x=0} = 0, \tag{3.10}$$

while for Mg^{2+}, the current is proportional to the current density, i:

$$N_{\mathrm{Mg}^{2+}}\big|_{x=0} = \frac{i}{2F}. \tag{3.11}$$

The zero-field approximation[49,134] is taken to govern the electrostatic potential at the WE surface,

$$\left.\frac{\partial \Phi}{\partial x}\right|_{x=0} = 0, \tag{3.12}$$

which assumes that the thickness of the double layer is negligible in comparison to the extent of the diffusion layer in the electrolyte, and thus the potential drop across the double layer does not substantially contribute to the potential difference between the WE and zero-field plane. For sufficiently large time and length scales, Streeter and Compton[49] concluded that the zero-field approximation was in agreement with a previously described dynamic double layer model.[135] The potential is set to a constant at the RE surface ($x = L$), and we choose the value to be zero for convenience:

$$\Phi|_{x=L} = 0. \tag{3.13}$$

Choosing this as the reference potential may introduce some amount of error in the calculated formal reaction potential, but this error is on the order of 10 mV, which is small compared to the uncertainties introduced by the differences between the model geometry and the experimental geometry.

Reaction Kinetics

The current density is taken to relate to the total (surface and concentration) overpotential through a reaction rate law. To account for the multistep reaction, Butler-Volmer equations are written for both reaction steps in Eqs. 3.6 and 3.7 in the form employed by Dickinson *et al.*.[50] We then employ an approach similar to that described by Newman and Thomas-Alyea,[35] where the intermediate species formed in Eq. 3.6 does not accumulate, and thus the current associated with the reaction in Eq. 3.6 must equal the current associated with the reaction in Eq. 3.7. If the heterogeneous rate constant associated with Eq. 3.7 is much greater than the rate constant associated with Eq. 3.6, the resulting current-overpotential relation may be written as

$$i = 2Fk^0 \left\{ c_{\mathrm{Mg}} \exp\left[\frac{(2-\beta)F}{RT}\eta\right] - c_{\mathrm{Mg^{2+}}} \exp\left[-\frac{\beta F}{RT}\eta\right] \right\}, \tag{3.14}$$

where i is the current density, k^0 is the standard heterogeneous rate constant for the multistep reaction, β is the symmetry factor, and $\eta = E - \Phi_0 - E^{0'}$ is the overpotential; where E is the potential of the WE (as compared to the RE), Φ_0 is the electrostatic potential in the electrolyte immediately adjacent to the electrode, and $E^{0'}$ is the formal potential of the redox reaction at the equilibrium electrolyte concentration.

The kinetic rate law presented above is insufficient for capturing all of the essential features of the electrodeposition and electrodissolution of magnesium within the 1D model. Experimentally obtained CV curves for the electrodeposition and electrodissolution of magnesium to and from non-magnesium electrodes exhibit a hysteresis in the current density.[99,108,109,119,136] Towards the more reducing potentials of the voltammogram, the onset of measurable current occurs later than would be expected, which is attributed to the effect of a nucleation overpotential associated with a free energy barrier for deposition.[100,136] In the oxidative region of the voltammogram, the current density increases until it abruptly drops to zero once all of the available magnesium has been dissolved from the WE. Experimentally, this drop-off occurs sooner than would be expected from the amount of magnesium deposited[119] because of Coulombic inefficiency. The following sections describe how both the nucleation overpotential and the Coulombic efficiency of the reaction process may be incorporated to supplement the kinetic rate law.

Nucleation

As mentioned, there is an overpotential associated with the nucleation of magnesium deposits upon the WE surface, and this overpotential may be observed experimentally. In the kinetic rate

law, the nucleation overpotential may be included as an additional term in the exponential. Experimental observations suggest that once a deposit has nucleated, no extra overpotential is necessary for its continued growth.[130] At any point during electrodeposition, nucleated deposits comprise a portion of the WE's surface area, with the balance being bare. The further nucleation and growth of deposits may both contribute to the measured current response, and as such, the kinetic rate law can be extended to represent a combination of the processes of deposit nucleation and subsequent growth:

$$i = 2Fk^0 \left\{ c_{\mathrm{Mg}} \theta \exp\left[\frac{(2-\beta)F}{RT}\eta\right] - c_{\mathrm{Mg^{2+}}} \left(\theta \exp\left[-\frac{\beta F}{RT}\eta\right] + (1-\theta)\exp\left[-\frac{\beta F}{RT}(\eta - \eta_{\mathrm{nuc}})\right]\right)\right\}, \tag{3.15}$$

where θ is the fractional coverage of the bare WE surface by deposits and η_{nuc} is the nucleation overpotential.

In organohaloaluminate electrolytes, it has been observed experimentally that magnesium nucleates in a hexagonal plate morphology.[33,100] Unfortunately, the available micrographs for $Mg(BH_4)_2$ in tetraglyme only show the deposit morphology well after the initial nucleation process has completed.[116] Thus we assume that that in $Mg(BH_4)_2$/DME, the deposits also nucleate as hexagonal plates with a constant ratio between the height and the deposit spacing; as these plates grow, they increasingly cover the WE surface and eventually merge. In this case, the value of θ is directly proportional to the average surface concentration of deposited magnesium, Γ_{dep}, until the deposits fully cover the WE and the fractional coverage reaches unity:

$$\theta = \begin{cases} \left(\dfrac{\Gamma_{\mathrm{dep}}(t)}{\Gamma_{\mathrm{ref}}}\right)^{\frac{2}{3}} & \Gamma_{\mathrm{dep}}(t) \le \Gamma_{\mathrm{ref}}. \\ 1 & \Gamma_{\mathrm{dep}}(t) > \Gamma_{\mathrm{ref}} \end{cases} \tag{3.16}$$

Here, $\Gamma_{\mathrm{ref}} = rd/\Omega$ represents the surface concentration of magnesium at which the surface is fully covered, where r is the ratio between the deposit's height and the reference deposit edge length, d, and Ω is the molar volume of magnesium. The surface concentration of deposited magnesium relates to the current density through

$$\Gamma_{\mathrm{dep}}(t) = -\int_0^t \frac{i(t)}{2F}\,dt. \tag{3.17}$$

Alternative assumptions can be made for the relationship between θ and Γ_{dep} to account for different deposit morphologies, which could be described in terms of their size, shape, and average spacing on the electrode surface. In future studies, it may also be desirable to account for the increased surface area of the electrode that would occur from the nucleation and growth of deposits; at present, it is assumed that this effect can be neglected.

Coulombic Efficiency

The 1D model also includes a phenomenological parameter that allows incorporation of the experimentally determined Coulombic efficiency, CE. This is defined as[108,109,137]

$$\mathrm{CE} = \frac{q_{\mathrm{diss}}^{\mathrm{tot}}}{q_{\mathrm{dep}}^{\mathrm{tot}}}, \tag{3.18}$$

where $q_{\mathrm{diss}}^{\mathrm{tot}}$ is the total charge that passes across the WE during electrodissolution and $q_{\mathrm{dep}}^{\mathrm{tot}}$ is the total charge that passes across the WE during electrodeposition. Since the charge is related to the integral of the current, Eq. 3.18 can be rewritten as follows:

$$\mathrm{CE} = \frac{\int_0^t i_{\mathrm{diss}}(t)dt}{\int_0^t i_{\mathrm{dep}}(t)dt} = \frac{\int_0^t N_{\mathrm{diss}}^{\mathrm{Mg^{2+}}}(t)dt}{\int_0^t N_{\mathrm{dep}}^{\mathrm{Mg^{2+}}}(t)dt}, \tag{3.19}$$

where $i_{\mathrm{diss}}(t)$ is the electrodissolution current, $i_{\mathrm{dep}}(t)$ is the electrodeposition current, and $N_{\mathrm{diss}}^{\mathrm{Mg^{2+}}}(t)$ and $N_{\mathrm{dep}}^{\mathrm{Mg^{2+}}}(t)$ are the fluxes of Mg^{2+} from and to the WE, respectively. These fluxes

are obtained by splitting Eq. 3.15 into its electrodeposition and electrodissolution components and applying Faraday's Law:

$$N_{\mathrm{diss}}^{\mathrm{Mg^{2+}}}(t) = k^0 C_{\mathrm{Mg}} \theta \exp\left[\frac{(2-\beta)F}{RT}\eta\right], \tag{3.20}$$

$$N_{\mathrm{dep}}^{\mathrm{Mg^{2+}}}(t) = k^0 C_{\mathrm{Mg^{2+}}} \left\{\theta \exp\left[-\frac{\beta F}{RT}\eta\right] + (1-\theta)\exp\left[-\frac{\beta F}{RT}(\eta - \eta_{\mathrm{nuc}})\right]\right\}. \tag{3.21}$$

A CE less than 1 (*cf.* Eq. 3.18) may arise from one or more processes in the cell that occur concurrently with the electrodeposition and electrodissolution of magnesium. In the experimental CV curves and electrochemical quartz crystal microbalance (EQCM) data presented by Lu *et al.*,[119] it seems reasonable to propose that these processes may be broadly categorized as one of two types. The first is a non-electrochemically active process that causes magnesium to be dissolved more quickly than expected (for example, magnesium becoming electronically isolated from the surface). The second is an electrochemically active process (such as a side reaction) during deposition that would contribute to the measured current, which would appear as if more magnesium was being deposited than in actuality. For our model, we assume a dominant process of the former type. Under the assumption that all deposited magnesium is subsequently dissolved from the WE, the following equation must hold:

$$\int_0^t N_{\mathrm{dep}}^{\mathrm{Mg^{2+}}}(t)dt = \int_0^t \left(N_{\mathrm{diss}}^{\mathrm{Mg^{2+}}}(t) + N_{\mathrm{side}}^{\mathrm{Mg^{2+}}}(t)\right)dt. \tag{3.22}$$

Further, we assume that the flux of Mg^{2+} due to processes not included in the redox couple, $N_{\mathrm{side}}^{\mathrm{Mg^{2+}}}$, is directly proportional to the electrodissolution flux, $N_{\mathrm{diss}}^{\mathrm{Mg^{2+}}}$, with a proportionality constant ω. This allows Eq. 3.22 to be rewritten as:

$$\int_0^t N_{\mathrm{dep}}^{\mathrm{Mg^{2+}}}(t)dt = \int_0^t \left(N_{\mathrm{diss}}^{\mathrm{Mg^{2+}}}(t) + \omega N_{\mathrm{diss}}^{\mathrm{Mg^{2+}}}(t)\right)dt = M + \omega M. \tag{3.23}$$

Equations 3.18 and 3.23 can be combined to determine the value of ω:

$$\omega = \frac{1}{\mathrm{CE}} - 1. \tag{3.24}$$

Finally, $i(t)$ in Eq. 3.17 is split into its components, $i_{\mathrm{diss}}(t)$ and $i_{\mathrm{dep}}(t)$, and $i_{\mathrm{diss}}(t)$ is multiplied by $(1 + \omega)$:

$$\Gamma_{\mathrm{dep}}(t) = -\int_0^t \frac{(1+\omega) i_{\mathrm{diss}}(t) - i_{\mathrm{dep}}(t)}{nF} dt, \tag{3.25}$$

which results in an expression of Γ_{dep} that is corrected for the effects of the Coulombic efficiency. Alternatively, if an additional electrochemically active process during deposition is dominant, one could still arrive at ω as described by Eq. 3.24, but Γ_{dep} would revert to Eq. 3.17, and the total measured current would be greater by a factor of $1 + \omega$ than the actual deposition current.

Numerical Methods

Equations 3.1 through 3.3 are coupled nonlinear partial differential equations that are numerically stiff,[48–50,138] requiring small time step size if an explicit time stepping scheme were employed. Therefore, the equations are discretized using a semi-implicit Crank-Nicolson scheme that is second order in space and second order in time. The spatial grid is composed of 100 points whose positions are given by:

$$x_j = x_{j-1} \left(\frac{L}{\Delta x_0} \right)^{\frac{1}{N-2}}, \tag{3.26}$$

where x_j is the j-th grid point position, $\Delta x_0 = 1$ Å is the minimum grid spacing, and N is the number of grid points. The grid point x_1 is at $-\Delta x_0$ and the grid point x_2 is at Δx_0. This generates a grid that has high resolution near the WE and lower resolution toward the RE, which ensures good numerical accuracy without sacrificing computational efficiency. At each grid point, five unknown quantities are defined: the concentrations of the four species (Mg^{2+},

$Mg(BH_4)^+$, BH_4^-, and undissociated $Mg(BH_4)_2$) in the electrolyte and the local electrostatic potential, Φ. All of the unknown quantities are solved simultaneously using the Newton-Raphson method, as described by Brumleve and Buck[48] and Streeter and Compton.[49] The linear system for the Newton-Raphson iteration is solved using Gaussian Elimination with partial pivoting.

A dimensionless scheme similar to those in the literature[48,50,139] was implemented to both improve the numerical accuracy and simplify the governing equations. The scheme is based upon four parameters: the nominal electrolyte concentration, c_{nom}, the thermal voltage, RT/F, the diffusivity of the magnesium cation, $D_{\mathrm{Mg^{2+}}}$, and the total cycle time, t_{max}. The resulting expressions for each dimensionless quantity are shown in Table 3.1. For this model, the relevant dimensionless quantities are the species concentrations, C_i, the electrostatic potential, ψ, the position, ζ, time, τ, the species diffusivity, δ_i, the standard heterogeneous rate constant, K^0, and a scale parameter, ξ, that relates the diffusion length of the electrolyte to the Debye length.

Applying the dimensionless scheme, the time evolution of the dimensionless Nernst-Planck equation is:

$$\frac{\partial C_i}{\partial \tau} = \delta_i \left[\frac{\partial^2 C_i}{\partial \zeta^2} + z_i \frac{\partial}{\partial \zeta} \left(C_i \frac{\partial \psi}{\partial \zeta} \right) \right], \tag{3.27}$$

and the dimensionless Poisson equation is:

$$\frac{\partial^2 \psi}{\partial \zeta^2} = -\xi^2 \sum z_i C_i. \tag{3.28}$$

The overpotential, applied electrode potential, and formal potential are also normalized by the thermal voltage, yielding the dimensionless surface flux of Mg^{2+}:

$$\begin{aligned} N^*_{\mathrm{Mg^{2+}}} = {} & K^0 C_{\mathrm{Mg}} \theta \exp[(2-\beta)\eta^{ND}] \\ & - K^0 C_{\mathrm{Mg^{2+}}} (\theta \exp[-\beta \eta^{ND}] + (1-\theta) \exp[-\beta(\eta^{ND} - \eta^{ND}_{\mathrm{nuc}})]). \end{aligned} \tag{3.29}$$

Here, η_{nuc}^{ND} is the dimensionless nucleation overpotential and $\eta^{ND} = E_{ND} - \psi_0 - E_{ND}^{0'}$ is the dimensionless overpotential, where E_{ND} is the dimensionless applied electrode potential and $E_{ND}^{0'}$ is the dimensionless formal potential.

Table 3.1. Expressions for the dimensionless quantities of the model.

Dimensional Quantity	Dimensionless Quantity
c_i	$C_i = c_i/c_{\mathrm{nom}}$
Φ	$\psi = \Phi F/RT$
x	$\zeta = x\left(D_{\mathrm{Mg^{2+}}} t_{\mathrm{max}}\right)^{-1/2}$
t	$\tau = t/t_{\mathrm{max}}$
D_i	$\delta_i = D_i/D_{\mathrm{Mg^{2+}}}$
k^0	$K^0 = k^0\left(t_{\mathrm{max}}/D_{\mathrm{Mg^{2+}}}\right)^{1/2}$
	$\xi = \left(c_{\mathrm{nom}}^2 F^2 D_{\mathrm{Mg^{2+}}} t_{\mathrm{max}}/RT\epsilon_0\epsilon_s\right)^{1/2}$

Fitting Procedure

The model described in the previous section is applied to construct a series of simulated CV curves. A semiautomatic procedure is adopted to determine the best-fitting parameters for the model. For each unknown parameter in the system, a batch-processing routine tests all possible combinations of parameters that are uniformly sampled from a discrete set within a range of values. For each simulated CV curve, the sum of squares of the difference with respect to the experimental data within a relevant portion of the voltage scan is calculated as a measure of the absolute error, which is minimized. For this study, the model simulates the CV curve between ± 1 V applied potentials, and for the calculation of the error we consider the voltage range starting at 0 V (where the experimental sweep started), to the lower bound of -1 V, and then back to 0.2 V (just before the peak during electrodissolution). This voltage range was chosen for the error calculation because the model is unable to capture the observed dissolution behavior past 0.2 V, which is likely due to changes in the deposit morphology that are not considered by the present approximations. To reduce the number of degrees of freedom within the parameter space, all of

the species arising from the dissociation of $Mg(BH_4)_2$ are taken to have equal diffusivity, D (consistent with the data reported by Rajput *et al.*[113]). In addition to D, the fitting procedure is used to obtain the values of the standard heterogeneous rate constant, k^0, the symmetry factor, β, the formal reaction potential, $E^{0'}$, and the nucleation overpotential, η_{nuc}, which appear in Eqs. 3.8 and 3.17.

This fitting procedure is applied to the first cycle of the experimentally obtained CV curve with a 20 mV/s voltage scan rate. An exploratory parameter sweep is performed to find the initial search range for subsequent parameter sweeps. A coarse parameter sweep is performed, and a histogram is generated of the parameter combinations whose sum of squared error (SSE) is less than 7×10^{-7} A^2/cm^4. This threshold value is chosen because it both encompasses the range of space where the likely parameters exist and results in voltammograms that are in good visual agreement with the experimental data. If a smaller tolerance is chosen, the histograms exhibit gaps in the peaks, which is due to an insufficient number of parameter sets that satisfy the tolerance at the coarse sampling resolution. The coarse histogram is then used to determine the bounds of a finer parameter sweep. To validate the model, we employ the resulting best-fit parameters to predict the behavior at the faster scan rates, which is then compared to the experimental data at the corresponding rates.

Results and Discussion

Parameter Fitting and CV Curve Prediction

The parameter spaces sampled and the numbers of sampling steps for the coarse and fine sweeps are summarized in Table 3.2, and additional parameters required for the simulation are summarized in Table 3.3. The sampling step size is equal for a given parameter and a given sweep. The coarse parameter sweep resulted in 38,880 combinations, the histogram of which is

shown as Figure 3.2. At the coarse level, the parameters exhibit unresolved peaks due to the low sampling resolution. Therefore, a fine parameter sweep was performed with 136,890 possible combinations, of which 145 (or 0.11% of tested combinations) met the SSE threshold of 7×10^{-7} A^2/cm^4. The histograms of the distributions of parameters for these calculations are shown in Figure 3.3. Compared to the coarse parameter sweep, the histograms in Figure 3.3 exhibit well-defined peaks due to their finer resolution. The voltammograms are shown in Figure 3.4 for the parameter sets that had the lowest overall SSE value as well as the highest value that was below the threshold. The SSE values and the parameter sets for these calculations are shown in Table 3.4. The experimental CV curve and the simulated CV curve with the best-fit parameter set are in good agreement except toward the end of dissolution, where the experimental data shows non-ideality, likely due to more complex deposit morphologies that are not accounted for in the model.

Using the best-fit parameter set, we predicted the voltammograms at the 50 and 100 mV/s voltage scan rates (shown in Figure 3.5). The predicted curves are again in good agreement with the experimental data for most of the voltage scan. In these cases, however, the slope of the simulated CV curves during electrodissolution better matched the experimental curves. In general, the predicted curves also show agreement with both the onset and cessation of deposition, although the peak deposition current is higher for the predicted curves than the experimentally observed peak current.

Table 3.2. Parameter spaces examined by the coarse and fine sweeps.

	Coarse			Fine		
Parameter	**Low**	**High**	**# steps**	**Low**	**High**	**# steps**
β	0.15	0.55	9	0.225	0.425	9
k^0 (cm/s)	1.78×10^{-8}	1×10^{-6}	8†	1.78×10^{-8}	5.62×10^{-7}	13†
D (cm^2/s)	0.9×10^{-5}	1.7×10^{-5}	9	1.0×10^{-5}	1.6×10^{-5}	13
$E^{0'}$ (V)	-0.02	0.08	6	-0.01	0.07	9
η_{nuc} (V)	-0.65	-0.2	10	-0.65	-0.2	10

†Indicates logarithmic step sizes were used.

Table 3.3. Additional simulation parameters.

Parameter	**Value**
ϵ_s	7.2†
T	298 K
L	5 cm
Δt	0.1 s
K_{d1}	4.77×10^{-5} mol/cm^3
K_{d2}	4.77×10^{-3} mol/cm^3
c_{Mg}	7.14×10^{-2} mol/cm^3
Ω	14 cm^3/mol
r	0.125
d	160 nm

†Value taken from Ref. 140.

Table 3.4. Parameters describing the lowest and highest SSE fits.

	Parameter Values	
Parameter	**Lowest SSE**	**Highest SSE**
SSE (A^2/cm^4)	5.32×10^{-7}	6.99×10^{-7}
β	0.3	0.375
k^0 (cm /s)	1.33×10^{-7}	5.62×10^{-8}
D (cm^2/s)	1.3×10^{-5}	1.2×10^{-5}
$E^{0'}$ (V)	0.03	0.01
η_{nuc} (V)	-0.3	-0.5

Table 3.5. Average parameter values fitted by model.

Parameter	**Average Value**
β	0.31 ± 0.04
k^0 (cm/s)	$1.3 \pm 0.4 \times 10^{-7}$
D (cm^2/s)	$1.3 \pm 0.1 \times 10^{-5}$
$E^{0'}$ (V)	0.030 ± 0.015
η_{nuc} (V)	-0.34 ± 0.07

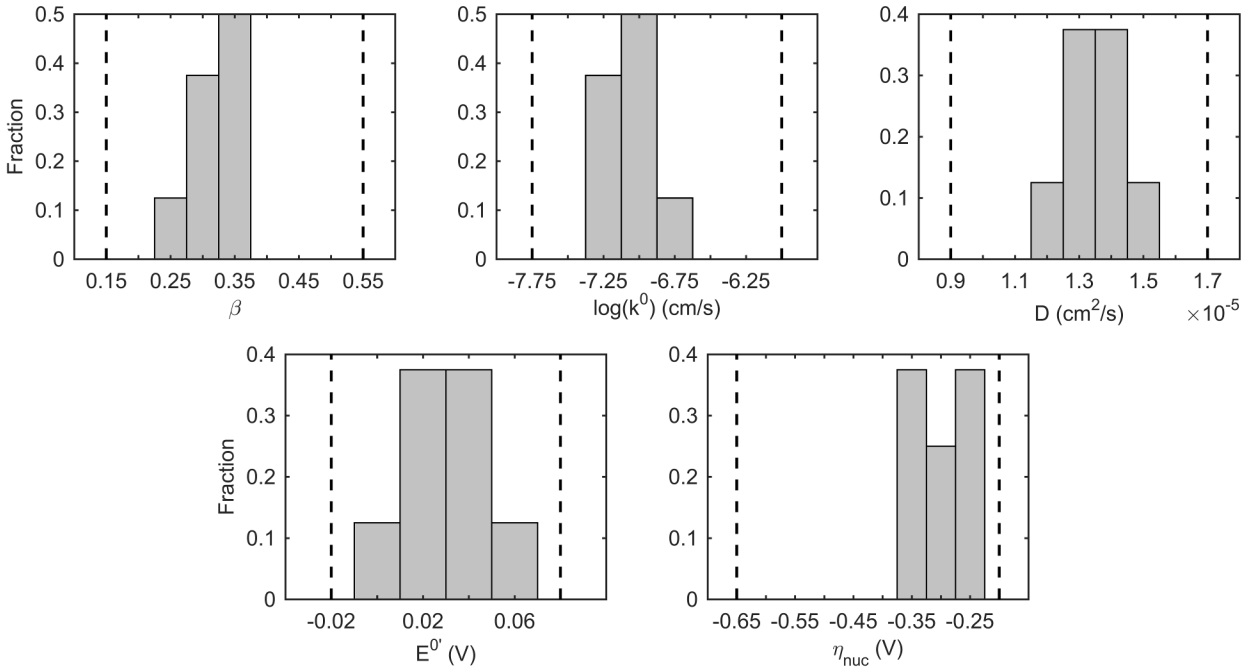

Figure 3.2. A histogram showing the distribution of parameters that result in simulated voltammograms with an SSE value below 7×10^{-7} A^2/cm^4 for 75 mM $Mg(BH_4)_2$ at 20 mV/s after the coarse parameter sweep. The dashed lines indicate the bounds of the parameter space.

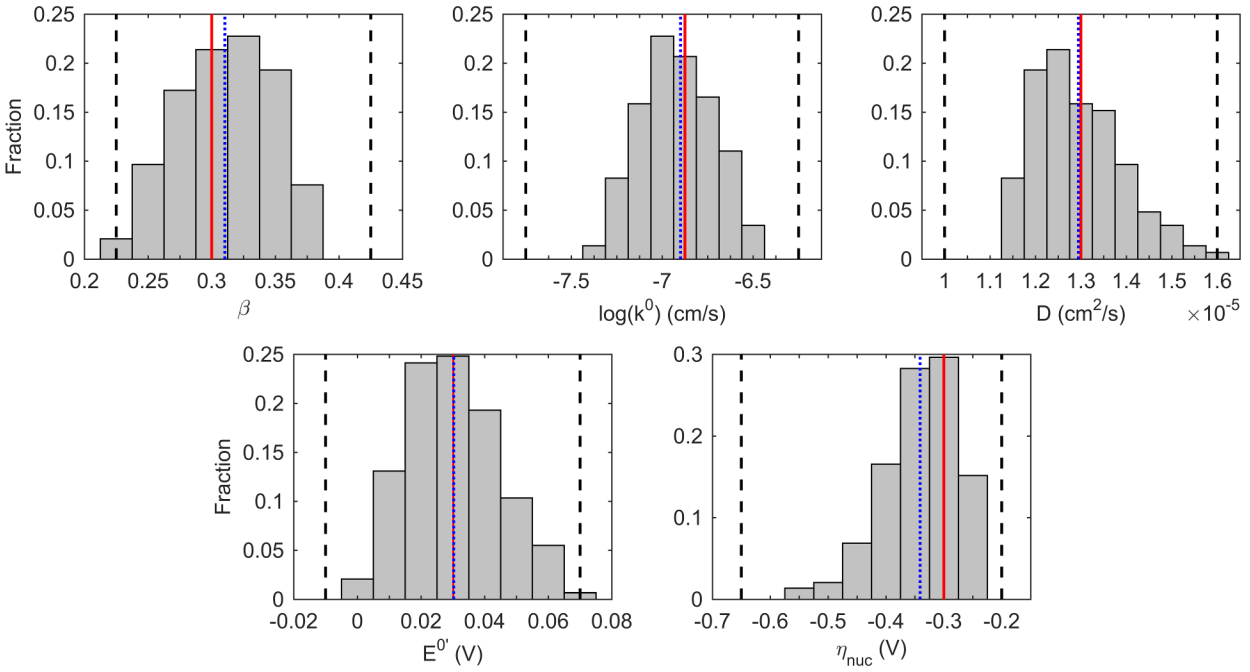

Figure 3.3. A histogram showing the distribution of parameters that result in simulated voltammograms with an SSE value below 7×10^{-7} A^2/cm^4 for 75 mM $Mg(BH_4)_2$ at 20 mV/s after the fine parameter sweep. The black dashed lines indicate the bounds of the parameter space. The solid red line indicates the best-fit value of the parameter, and the dash-dot blue line indicates the mean value of the parameter.

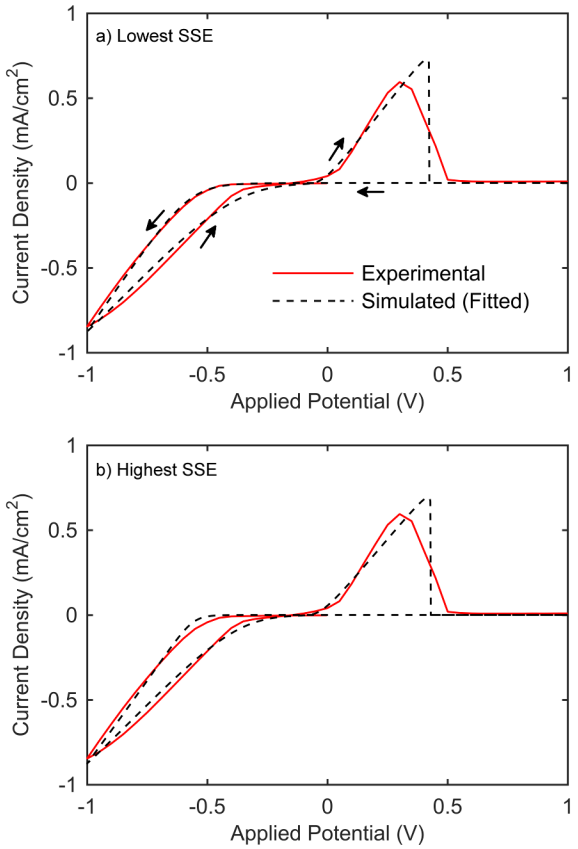

Figure 3.4. A comparison of the experimental (solid red) and simulated (dashed black) cyclic voltammograms for the 75 mM concentration at 20 mV/s for the combinations of the parameters that resulted in (a) the lowest sum of squared error and (b) the highest sum of squared error below the threshold of 7×10^{-7} A^2/cm^4. The parameters for each curve are reported in Table 3.4.

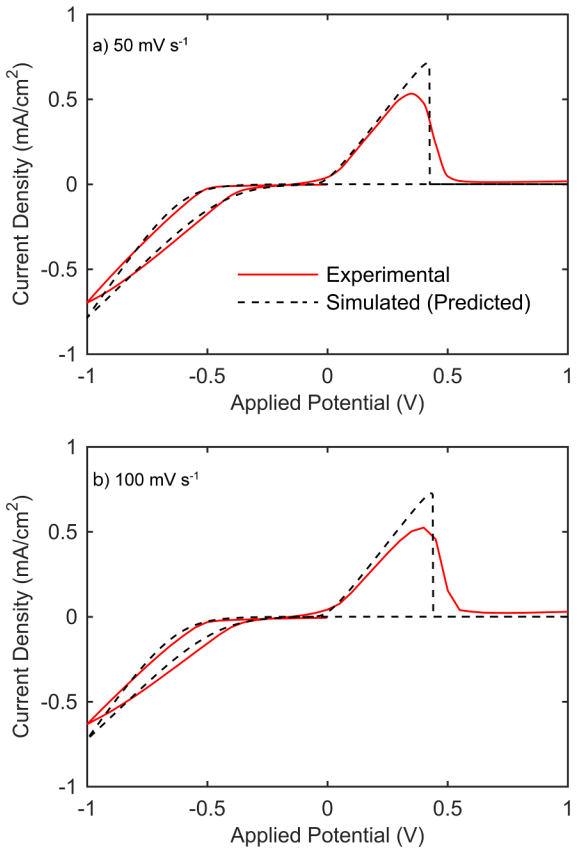

Figure 3.5. A comparison of the experimental (solid red) and simulated (dashed black) cyclic voltammograms for the 75 mM concentration at (a) 50 mV/s, and (b) 100 mV/s. The best-fit values in Table 3.4 that were obtained by fitting the 20 mV/s curve were then used to predict the behavior at higher sweep rates.

To estimate the uncertainties of the fitted parameters, the mean and standard deviation was calculated for each parameter, the values of which are summarized in Table 3.5. It is observed that the best-fit parameter set is within one standard deviation of the mean values. Comparison of the fitted parameters with experimental data is difficult because, as was mentioned previously, many of these parameters do not have reported values in the literature. However, we may make comparisons for both D and η_{nuc}. For D, the fitted value of 1.3×10^{-5} cm^2/s is about six times larger than the value of approximately 2×10^{-6} cm^2/s reported by Rajput *et al.*[113] While a value of η_{nuc} is not available for nucleating magnesium upon a gold substrate, literature values upon copper, platinum, nickel, and silver range from -240 mV to -850

mV,[100,129,130] and our fitted value of -300 mV is within the range. It should be noted that the predicted values of k^0 and η_{nuc} would depend on the assumed deposit geometry, as well as the cell geometry.

For the symmetry factor, β, the fitted value of 0.31 is lower than the value of 0.5 that has been measured previously for lithium deposition.[141] It is well-known that the charge transfer coefficient, and consequently the symmetry factor, depends upon the overall reaction mechanism.[142,143] Although the model is capable of isolating a likely value of β, the fitted value depends on the assumed reaction mechanism. Therefore, if the actual mechanisms differ from the assumed mechanism, the fitted value of β may not be representative. However, this does lead to the possibility of future investigations that could be performed with the described model to determine whether or not the calculated value of β is a consistent trend in magnesium electrochemistry.

Overall, the results demonstrate that while it is feasible to determine the parameters using the described fitting procedure, there is a moderate degree of uncertainty in the calculated parameters. However, the uncertainties would be reduced if one or more of the parameters—particularly the deposit morphology throughout the cycle—could be accurately determined experimentally. It should also be noted that there is an inherent error in the values summarized in Table 3.5 because of the fact that the simulated cell geometry does not exactly correspond to the one used in the experiments reported in this work. However, the data is sufficient for the demonstration of the approach.

Effect of Sweep Rate on Peak Current

Generally, an increase in the sweep rate is expected to lead to an increase in the magnitude of the peak currents in the voltammogram from non-Faradaic processes.[37,50] However, both the

experimental and simulated results in Figure 3.4 and Figure 3.5 exhibit a decrease in the magnitude of the peak current with increasing scan rate. We propose that the decrease in peak current is due to a smaller amount of electrochemically active magnesium and not non-Faradaic behavior of the electrolyte. In Figure 3.6, it is observed that as the sweep rate increases, there is a corresponding decrease in the simulated value of θ at the peak deposition current. This is primarily a result of the shorter duration of the cycle at higher voltage scan rates within the same fixed voltage range. As stated in Eq. 3.25, the total amount of deposited magnesium is related to the time integral of the current. Thus, at higher rates, less magnesium is deposited even if the current at a given voltage is otherwise the same.

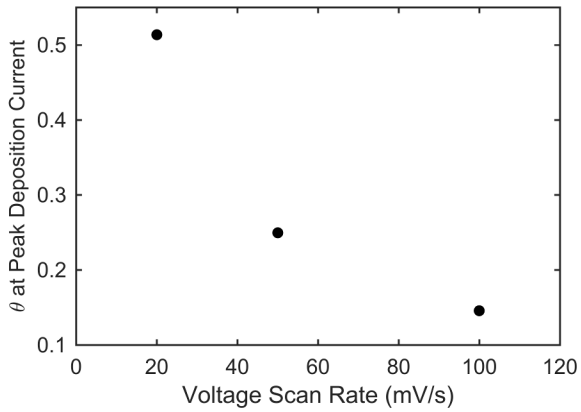

Figure 3.6. A plot of the fraction of the surface area covered by magnesium, θ, at the peak deposition current as a function of the sweep rate. At higher sweep rates, less material can be deposited due to the shorter duration of the cycle, reducing the coverage by magnesium.

While the model agrees with the experimentally observed trend of a decreasing peak current with increasing sweep rate, the model predicts a smaller magnitude of decrease than is experimentally observed. The likely cause of this discrepancy is that the actual deposit morphology is more complex than that assumed in the model. By inspection of Eq. 3.15, the deposition behavior may be split into two limiting cases: deposition purely by growth of existing deposits or by nucleation of new deposits. The nucleation overpotential lowers the formal

potential of the reaction, which shifts the voltammetric behavior to more negative applied potentials. Thus, at a given negative applied potential, deposition by nucleation would yield a lower current than deposition by growth. It can be observed from the simulation that θ serves to shift the deposition curve in between these two extremes. Therefore, we conclude that the assumed nucleation model overestimates the active amount of magnesium, and consequently the current is predicted to be higher than is observed experimentally. Future experimental work may be able to inform the model regarding more realistic morphology of the magnesium deposits, which may depend on the voltage scan rate.

Considerations of Experimental Geometry

Using the parameters predicted by the model, we also predict the response of the voltammogram to changes in the spacing between the WE and the RE. For this test, we calculated the voltammogram for a 75 mM electrolyte at a voltage scan rate of 20 mV/s, assuming spacings of 2.5 cm, 5 cm (the actual experimental spacing), and 10 cm using the parameters given in Table 3.4. The resulting curves are plotted in Figure 3.7, where the magnitude of the measured current decreases as the electrode spacing increases. This relationship is of the form $i \propto 1/L$, where L is the WE/RE spacing; halving the electrode spacing roughly doubles the measured current density at a given point and doubling the spacing halves the measured current density. Therefore, the model indicates that when using electrodes that are large as compared to the separation between them, the spacing between the WE and RE must be known in order to accurately determine the dynamics of the system. This behavior arises from the uncompensated resistance of the poorly conductive unsupported electrolyte. This is in agreement with the report by Myland and Oldham,[144] which concluded that, for a weakly conductive electrolyte, the uncompensated resistance will always have an effect on the measured cell behavior unless the separation

between the WE and RE becomes infinitesimally small. Thus, the cell geometry should always be reported for experimental measurements of voltammetry with unsupported electrolytes.

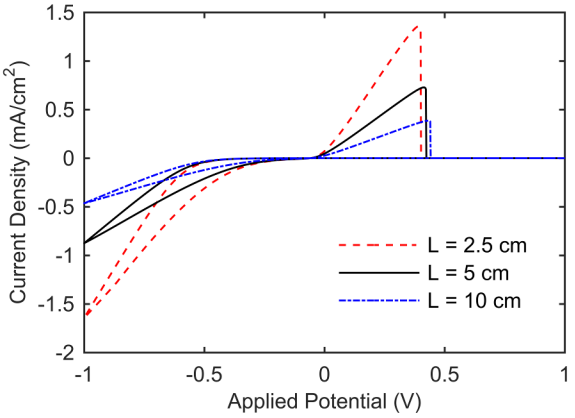

Figure 3.7. The impact of the spacing between the WE and RE in the model. As the spacing increases, the measured current response to the voltage sweep decreases. These curves were calculated using the parameters for the 75 mM electrolyte at 20 mV/s.

Summary and Conclusions

A 1D model was developed to simulate the cyclic voltammetry of a $Mg(BH_4)_2$/DME electrolyte with a gold WE and a magnesium RE by simultaneously solving the Nernst-Planck and Poisson equations for the mass transport and electrostatic potential, respectively. Additional modifications were made to the governing equations to account for the nucleation behavior of magnesium upon the WE and the experimentally determined Coulombic efficiency. This model was parameterized by batch fitting to the first cycle of experimentally obtained voltammograms for 75 mM concentration of electrolyte at 20 mV/s. The fitted parameters were employed to predict the voltammetric behavior at 50 and 100 mV/s. Histograms of the parameter sets that produce a good fit to the experimental voltammogram over a large parameter space were generated. The results show that the model is able to predict a likely range of the parameters that describe the system. The best-fit values of the parameters produce cyclic voltammograms that

are overall similar to the experimental curves against which they were fit, and the predicted voltammograms at higher sweep rates also exhibit good agreement with the experimental data.

The model, combined with the fitting procedure, allowed for the determination of kinetic information of the $Mg(BH_4)_2$/DME electrolyte, but this was made possible by employing several assumptions to minimize degrees of freedom in the system of equations. First, it was assumed that the electrolyte was mostly dissociated into solvated ions and the electroactive species was Mg^{2+}. Second, convection was assumed not to contribute to mass transport. Third, a simple deposit morphology was assumed to describe the surface of the WE due to a lack of available experimental data. Fourth, the Coulombic efficiency below unity was assumed to arise from a non-electrochemical process that occurs during dissolution. Fifth, all solute diffusivities were assumed to be equal. Finally, experimental data with a planar cell geometry were not available, and thus a data set obtained with a disk microelectrode and comparatively larger counter and reference electrodes was utilized. Based on the present simulation results, an experimental setup with a planar electrode geometry where the electrodes are large with respect to the separation between them appears to be a viable scheme for extracting the parameters governing reaction kinetics and mass transport. In addition, the electrode separation must be accurately measured and reported for such a setup because it plays a key role in the dynamic behavior captured by the voltammogram. There are also moderate uncertainties in the average values of some of the fitted parameters, which are likely due to interplay between the surface deposit morphology, nucleation overpotential, and standard heterogeneous rate constant. With experimental work to accurately measure values of even one or two parameters, the uncertainties in the remaining parameters should decrease greatly.

Chapter 4.

One-Dimensional Model of Lithium Symmetric Cells Under Galvanostatic Conditions

Introduction

In this chapter,* the one-dimensional framework developed in Chapter 3 is adapted and extended for the study of lithium/lithium symmetric cells. Like magnesium, lithium metal is an attractive material for next-generation secondary battery anodes due to its improved theoretical energy density as compared to existing lithium-ion technologies.[145] However, the use of lithium as an anode is complicated by the tendency of lithium to form dendritic features during electrodeposition.[13,14,146–150] The formation of these dendrites is accompanied by a rapid increase in electrode surface area and consumption of the electrolyte due to the growth of the solid electrolyte interphase (SEI) on the dendrite. Previous studies have attempted to suppress dendrite growth, such as through depositing thin layers of alumina on the anode,[148] co-deposition of cesium or rubidium,[150] or using highly concentrated electrolytes and ionic liquids.[151,152] However, there has not been a general consensus on the reaction pathways involved during lithium deposition and how they affect dendrite formation.[153]

Here, the one-dimensional model is combined with results from an experimental study[14] to gain further insight into how morphological evolution of the lithium surface due to preferential

*Adapted from K.N. Wood, E. Kazyak, A.F. Chadwick, K.-H. Chen, J.-G. Zhang, K. Thornton, and N.P. Dasgupta, "Dendrites and Pits: Untangling the Complex Behavior of Lithium Metal Anodes through Operando Video Microscopy," *ACS Cent. Sci.*, 2 (**2016**) 790. This is an unofficial adaptation of an article that appeared in an ACS publication. ACS has not endorsed the content of this adaptation or the context of its use.

deposition and dissolution of dendrites affects the time-dependent cell behavior. As detailed in Ref. 14, a lithium/lithium symmetric cell with a planar geometry was fabricated such that it could be observed *in operando* via optical video microscopy. The morphology of the lithium electrodes is observed while galvanostatic voltage traces are recorded, which allows for real-time correlation between features in the voltage trace and the electrode surface morphology. An example galvanostatic voltage trace and the corresponding optical micrographs for the electrode that initially undergoes deposition (referred to as EL-b) are presented in Figure 4.1. Here it is observed that, as dendritic deposition occurs on EL-b, there is an initial decrease in the magnitude of the cell polarization (a and b). The sign of the applied current is reversed, inducing dissolution of EL-b, during which the magnitude of the polarization decreases (c) until the previously deposited dendrites are removed, at which point the polarization is at a local maximum (d). Pits then nucleate on the electrode surface, which correspond to another decrease in the magnitude of the cell polarization (e). During the next deposition half-cycle, new dendritic material nucleates and grows on the electrode surface, including in the pits (f). Additionally, the galvanostatic voltage trace demonstrates the characteristic "peaking" behavior of the symmetric cell. In the subsequent sections of this chapter, the 1D model is employed to determine how transport in the electrolyte, the deposition/dissolution reaction kinetics, and the time-dependent electrode morphology all contribute to this observed behavior.

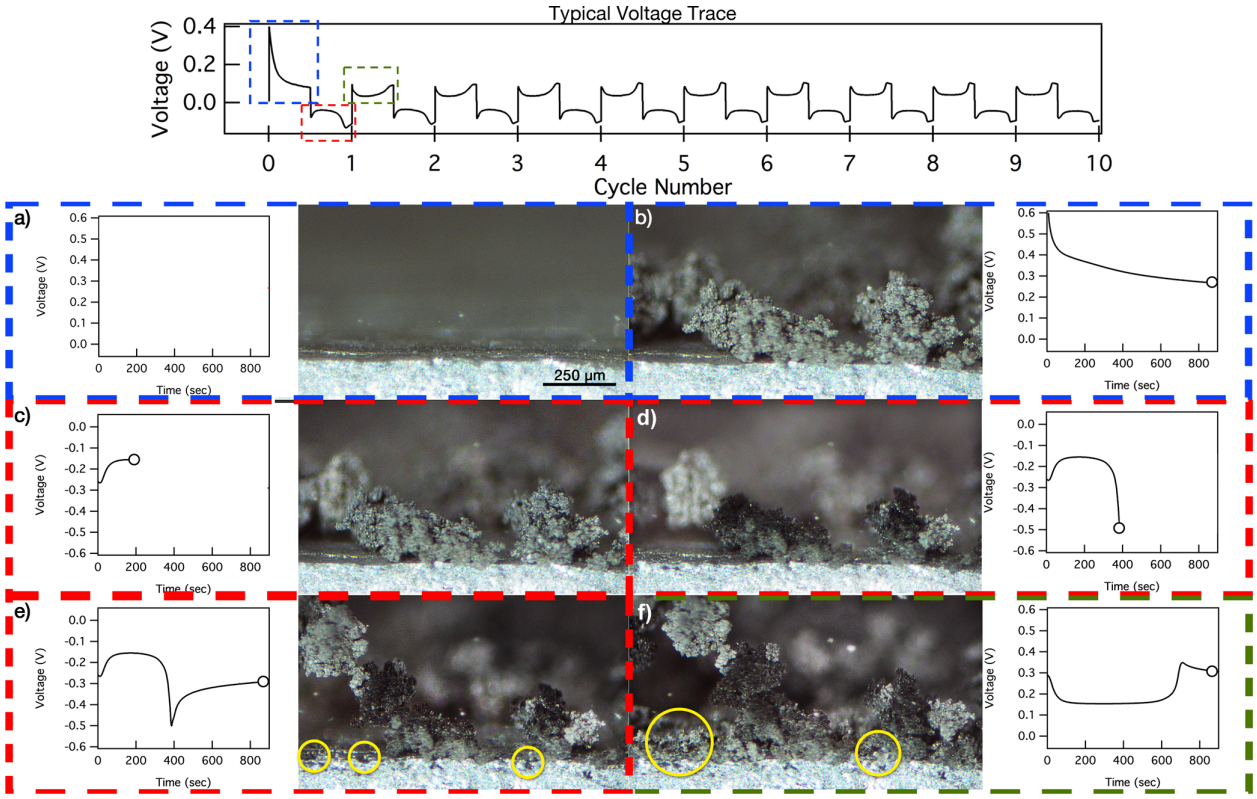

Figure 4.1. Experimentally observed electrode morphologies and the corresponding galvanostatic voltage trace for a lithium/lithium symmetric cell cycled at 5 mA/cm^2, reproduced from Ref. 14. The morphology is shown for the electrode that initially undergoes deposition (EL-b in subsequent experimental data) at times (a) before cycling; (b) after first half-cycle (deposition at EL-b); (c) at cell polarization minimum (dissolution at EL-b); (d) at cell polarization maximum; pitting not yet evident; (e) morphology at end of half-cycle; pitting observed (examples highlighted in yellow circles); (f) morphology at end of third half-cycle (deposition at EL-b); new dendrites are deposited in the pits which formed at the end of the previous half-cycle (yellow circles).

Governing Equations

To provide a theoretical description of the cell behavior, a one-dimensional (1D) numerical continuum-scale model is developed by extending the model in Chapter 3. The mass fluxes of the electrolyte species are described by the 1D Nernst-Planck equation[38–40]

$$N_i = -D_i \frac{\partial c_i}{\partial x} - z_i \frac{F}{RT} D_i c_i \frac{\partial \Phi}{\partial x}, \tag{4.1}$$

where N_i is the scalar flux and the remaining quantities have the same meaning as in Chapter 3. This mass flux includes contributions from diffusion and migration. The diffusivity is dependent

upon the concentration of the electrolyte species, and the values are taken from the experimental data obtained by Valøen and Reimers.[154] The time-dependent evolution of the concentration of each species follows the 1D continuity equation

$$\frac{\partial c_i}{\partial t} = -\frac{\partial N_i}{\partial x}. \tag{4.2}$$

There are several approaches that have been employed in the literature to describe the electrostatic potential, including electroneutrality,[35,155,156] continuity of the current,[33,35,156] the displacement current equation,[46–48] and the Poisson equation,[20,49,50] which is the approach adapted for this model. The 1D Poisson equation is

$$\frac{\partial^2 \Phi}{\partial x^2} = -\frac{\rho}{\epsilon_0 \epsilon_s}. \tag{4.3}$$

For this work, the model uses a 1D domain (depicted in Figure 4.2) where the boundaries correspond to the surfaces of the lithium electrodes, initially located at $x = 0$ and $x = L$. These interfaces are allowed to move independently, and the velocity of each electrode surface may be calculated by Faraday's law:

$$v_{\mathrm{el}} = \frac{i\Omega_{\mathrm{Li}}}{F}, \tag{4.4}$$

where v_{el} is the electrode surface velocity, i is the current density (as measured per unit projected area of the electrode), and Ω_{Li} is the molar volume of metallic lithium.[33] Over the course of a half-cycle, the electrode surfaces only move a small distance relative to the electrode separation, and we therefore neglect convection in the electrolyte and its effect on Eq. 4.1. The boundary conditions for the species concentrations and the electrostatic potential are given in Table 4.1, with the extra boundary condition on the electrostatic potential at $x = L$, which is necessary to prevent the PNP equations from becoming ill-posed.

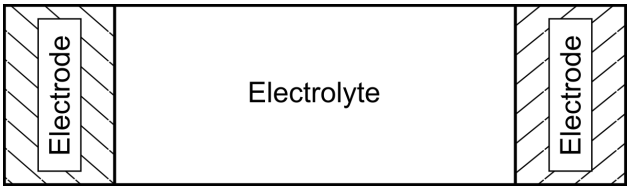

Figure 4.2. A schematic representation of the geometry employed by the model, not necessarily to scale.

Table 4.1. Boundary conditions for the PNP equations. The extra boundary condition on the electrostatic potential prevents the equations from becoming ill-posed.

Quantity	$x = 0$ (Left)	$x = L$ (Right)
c_{Li^+}	$N_{\mathrm{Li}^+} = i/F$	$N_{\mathrm{Li}^+} = i/F$
$c_{\mathrm{PF}_6^-}$	$N_{\mathrm{PF}_6^-} = 0$	$N_{\mathrm{PF}_6^-} = 0$
Φ	$\frac{\partial \Phi}{\partial x} = 0$	$\frac{\partial \Phi}{\partial x} = 0, \Phi(L) = 0$

At each electrode, the applied current is assumed to be governed by Butler-Volmer kinetics, for which the current-overpotential relationship may be written as:[35,37,49,50]

$$i = Fk^0 \left[c_{\mathrm{Li}} \exp\left(\frac{(1-\beta)F}{RT} \eta \right) - c_{\mathrm{Li}^+} \exp\left(-\frac{\beta F}{RT} \eta \right) \right], \tag{4.5}$$

where k^0 is the standard heterogeneous rate constant, β is the charge transfer symmetry coefficient, $c_{\mathrm{Li}} = 1/\Omega_{\mathrm{Li}}$ is the surface concentration of metallic lithium, and c_{Li^+} is the surface concentration of lithium ions. The overpotential, η, may be further rewritten as:

$$\eta = E_{\mathrm{el}} - \Phi_0 - E^{0'}, \tag{4.6}$$

where E_{el} is the electrode potential, Φ_0 is the electrostatic potential at the electrode/electrolyte interface, and $E^{0'}$ is the formal potential of the electron transfer reaction.[49,50,157]

To capture the effects of the electrode morphology and the SEI layer, two modifications are made to Eq. 4.5 that are consistent with the approach in Chapter 3.[20] First, the right-hand side is multiplied by γ, which is a measure of the roughness of the electrode surface. This coefficient is calculated as the ratio of the total surface area including deposits relative to the surface area of

the electrode if it was perfectly flat. The second modification is that k^0 becomes dependent upon the extent to which the electrode is covered in deposits. In this model, we assume that the reaction kinetics is faster on the deposits than on the bulk electrode, which may be attributed to differences in the SEI layer. The SEI layer on the deposits may be thinner and/or more defective than that on the bulk electrode, or it may have an entirely different chemical composition, leading to the higher reaction rate.[9] The assumption of different kinetics between the deposit and the bulk may be expressed as:

$$k_{\text{eff}}^0 = \theta_{\text{fast}} k_{\text{fast}}^0 + (1 - \theta_{\text{fast}}) k_{\text{slow}}^0, \tag{4.7}$$

where θ_{fast} is the fraction of the surface area with fast kinetics, and k_{fast}^0 and k_{slow}^0 are the rate constants for the deposit surface and the bulk electrode surface, respectively. The modified current-overpotential relationship is therefore:

$$i = \gamma F k_{\text{eff}}^0 \left[c_{\text{Li}} \exp\left(\frac{(1-\beta)F}{RT} \eta \right) - c_{\text{Li}^+} \exp\left(-\frac{\beta F}{RT} \eta \right) \right], \tag{4.8}$$

which accounts for the effects of the electrode morphology and the SEI layer. Note that this current density is defined per nominal area of the electrode (i.e., the area if the electrode were flat). This form of the modified current-overpotential relationship is similar to the one defined for the electrodeposition and electrodissolution of magnesium[20] in Chapter 3. Integrating Eq. 4.8 in time results in the deposited charge per nominal area, Γ_{dep}:

$$\Gamma_{\text{dep}}(t) = -\int_0^t \frac{i(t)}{F} dt. \tag{4.9}$$

Figure 4.3. Schematic showing the modeled approximation of lithium deposits as a uniform square array of hemispheres that grow and eventually impinge during electrodeposition and that contract and separate during

electrodissolution. In reality, the dendritic growth result in porous structure, which behaves similarly to the model due to screening.

To mathematically describe the values of both γ and θ_{fast}, it is necessary to make some assumptions about the geometry of the lithium deposits. We assume that the deposits grow as an array of uniform hemispheres, and that the hemispheres may begin to impinge and then eventually merge, which is depicted schematically in Figure 4.3. This assumption is consistent with the observations of Stark *et al.*[158] The volume of the hemispherical deposit (with radius r), V_d, may be calculated by solving the following integral in the x-y plane:

$$V_{\mathrm{d}} = \iint (r^2 - x^2 - y^2)^{1/2}\, dx\, dy. \tag{4.10}$$

The surface area of the deposit, A_d may be calculated by solving:

$$A_{\mathrm{d}} = \iint \left(\frac{r^2}{(r^2 - x^2 - y^2)}\right)^{1/2} dx\, dy, \tag{4.11}$$

and the uncovered area of the electrode, A_e^u may be calculated by solving:

$$A_{\mathrm{e}}^{\mathrm{u}} = A_{\mathrm{e}}^{\mathrm{n}} - \int (r^2 - x^2)^{1/2}\, dx, \tag{4.12}$$

where A_e^n is the nominal area of the electrode. The bounds of the integrals depend upon the extent of the hemispherical deposit and whether it has impinged on its neighbors. The volume per nominal area of the electrode is then related to Γ_{dep}. With Eqs. 4.11 and 4.12, it is possible to calculate both γ and θ_{fast}:

$$\gamma = \frac{A_{\mathrm{d}} + A_{\mathrm{e}}^{\mathrm{u}}}{A_{\mathrm{e}}^{\mathrm{n}}}, \tag{4.13}$$

$$\theta_{\mathrm{fast}} = \frac{A_{\mathrm{d}}}{A_{\mathrm{d}} + A_{\mathrm{e}}^{\mathrm{u}}}, \tag{4.14}$$

and the values of these two quantities may be related to the deposited charge per nominal area via Eq. 4.10.

To include its effect in the model, it is necessary to define the effective Coulombic efficiency. We follow a definition similar to those in the literature:[137]

$$\mathrm{CE} = \frac{\text{mass of dissolved Li from prev. deposits}}{\text{mass of deposited Li to prev. deposits}}. \tag{4.15}$$

In the visualization cell, it was clearly observed that electrochemically dead lithium forms during dissolution.[14] However, for simplicity, the model does not explicitly track the amount of dead lithium that has formed. Instead, we assume that a less-than-unity Coulombic efficiency would result in an apparently faster dissolution of the deposited lithium as some lithium is converted to dead lithium and does not contribute to the current. Thus, the Coulombic efficiency is incorporated as an effective multiplier of the applied current density during electrodissolution:

$$i^{\mathrm{eff}} = i\frac{1}{\mathrm{CE}}, \tag{4.16}$$

where i^{eff} is the effective applied current density during electrodissolution. This increased current only occurs at the electrode that is currently being dissolved. In addition, we assume that lithium may only be dissolved from the bulk electrode once the deposited lithium layer has been removed. The effective velocity of the electrode/electrolyte interface during electrodissolution is then given by:

$$v_{\mathrm{el}}^{\mathrm{eff}} = v_{\mathrm{el}}\frac{1}{\mathrm{CE}}, \tag{4.17}$$

where $v_{\mathrm{el}}^{\mathrm{eff}}$ is the effective velocity of the electrode/electrolyte interface, which is greater than the theoretical velocity when the Coulombic efficiency is less than unity.

Numerical Methods

For this study, a backward-implicit finite difference method (FDM) was employed to discretize and solve the governing equations. A typical backward-implicit stencil was found to not

conserve the mass of the system, and thus the following discretization[159] was employed for equation (S2):

$$c_j^{n+1}\Delta x_j^{b,n+1} + \Delta t\left(N_j^{+,n+1} - N_j^{-,n+1}\right) = c_j^n \Delta x_j^{b,n}, \tag{4.18}$$

where the superscript n refers to the current time step, the subscript j refers to the grid point, $\Delta x_j^b = x_j^b - x_{j-1}^b$ is the difference in the cell boundary positions of the grid point, Δt is the time step size, and N_j^+ and N_j^- are the fluxes in and out of the cell at positions x_j^b and x_{j-1}^b, respectively. The overall FDM was second order in space and first order in time. Note that explicit forward Euler time stepping can also be described with a stencil similar to Eq. 4.18, but second-order schemes such as Crank-Nicolson and DuFort-Frankel were found to not conserve mass in the system.

The model domain is initially discretized using a cell-centered grid of 100 grid points that are evenly spaced between the electrodes. An additional ghost point is placed outside each edge of the computational domain to ensure centering of the boundary conditions. A detailed schematic of a portion of the grid is shown in Figure 4.4. The boundaries are allowed to move over time with the velocities $v_{\mathrm{el}}^{\mathrm{left}}$ and $v_{\mathrm{el}}^{\mathrm{right}}$. To ensure that the edge of the computational domain (excluding the ghost zone) remains at the midpoint between the ghost point and the first point within the computational domain, these points are moved at the same velocity. As a result, the size of the second cell from the edge cell changes as deposition or dissolution occurs. To prevent this cell from becoming too large, it was divided into two if it became larger than $1.5\Delta x^0$, where Δx^0 is the initial grid spacing. Likewise, if a cell became smaller than $0.5\Delta x^0$, it was merged with its neighbor to maintain numerical accuracy.

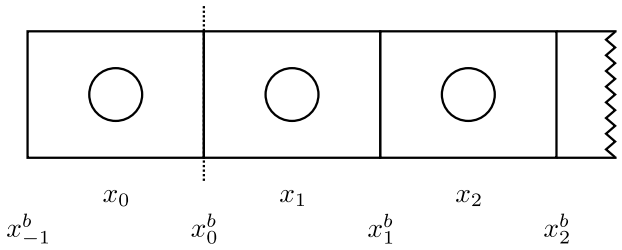

Figure 4.4. A schematic depiction of the cell-centered grid used for the finite difference discretization employed by the model. The variable x_j denotes the locations of the cell center for grid point j, and x_j^b denotes the location of the boundary between grid points j and $j+1$.

The discretization of Eqs. 4.1 through 4.3 with N grid points in the computational domain results in a system of 3(N+2) nonlinear equations with 3(N+2) unknown variables, $c_{\mathrm{Li^+}}$, $c_{\mathrm{PF_6^-}}$, and ϕ, associated with each grid point (including the ghost points). The system of equations may be solved simultaneously using the Newton-Raphson method, the details of which may be found in Refs. 48 and 49. The Newton-Raphson method is also employed when adding a grid point in the refinement scheme. The values of the concentrations and electrostatic potentials are known on either side of the refined cells, and the remaining unknown quantities may be calculated by assuming that mass is conserved and that the mass flux at one of the boundaries of the cell to be refined remains constant during the refinement process. When two cells are merged, the concentration of the new cell is calculated from the conservation of mass alone. The electric potential of each electrode is calculated separately from the PNP equations by solving Eq. 4.8. The difference between $E_{\mathrm{el}}^{\mathrm{left}}$ and $E_{\mathrm{el}}^{\mathrm{right}}$ is the cell voltage. The deposited charge per unit surface area, Γ_{dep}, is calculated by integrating the applied current density with respect to time. To improve the computational performance, a lookup table was used to interpolate γ and θ_{fast} for a given value of Γ_{dep}. This lookup table was generated by numerically evaluating Eqs. 4.9-4.14 from a lower radius bound of $r = 0$ to an upper bound of $r = R_{\mathrm{dep}}^{\mathrm{max}}$ in increments of Δr. The nominal electrode area was calculated based on a center-to-center deposit spacing, d_{deposit}. For

all portions of the model that use the Newton-Raphson method, the iteration was performed until the residuals were less than a tolerance $10^6\epsilon_m$ (2.22×10^{-10}), where ϵ_m is machine precision for double precision floating point arithmetic. Decreasing the tolerances beyond this value did not change the final simulation result. To avoid instances where the residual never reached the tolerance, the grid refinement scheme employed an adaptive tolerance that would increase by one order of magnitude if the Newton-Raphson method failed to converge within 10,000 iterations.

Table 4.2. Parameter values used for simulation of potentiometric behavior in the visualization cell.

Parameter	Value	Ref.
c_{nominal}	$1.0 \times 10^{-3}\,\text{mol/cm}^3$	
$c_{\text{Li}^+}^{\text{init}} = c_{\text{PF}_6^-}^{\text{init}}$	$0.5 \times 10^{-3}\,\text{mol/cm}^3$	154
D_{nominal}	$3.208 \times 10^{-6}\,\text{cm}^2/\text{s}$	154
Ω_{Li}	$13.0\,\text{cm}^3/\text{mol}$	
ϵ_s	16.8	160–162
T	300 K	
i	$5.0\,\text{mA/cm}^2$	
$t_{\text{on}}^+ = t_{\text{on}}^-$	900 s	
t_{off}	30 s	
n_{cyc}	5	
β	0.5	141
$E^{0'}$	0.0 V	
k_{fast}^0	$3.5 \times 10^{-6}\,\text{cm/s}$	
k_{slow}^0	$9.0 \times 10^{-8}\,\text{cm/s}$	
CE	80 %	
L	7.5×10^{-2} cm	
x_{int}	1.0×10^{-8} cm	
Δt	1.0×10^{-2} s	
Δr	1.0×10^{-6} cm	
d_{deposit}	2.4×10^{-3} cm	14
ϵ_m	2.22×10^{-16}	

Model Results and Discussion

Table 4.2 contains values of the parameters that were used for the simulation of the visualization cell. The initial concentrations of Li^+ and PF_6^- ($c_{\text{Li}^+}^{\text{init}}$ and $c_{\text{PF}_6^-}^{\text{init}}$), the nominal diffusivity, the solvent dielectric constant, and the charge transfer symmetry coefficient were parameterized

from available data.[141,154,160–162] The deposit spacing is chosen such that it is consistent with what is observed in the video data[14] and with observations by Stark *et al*.[158] The rate constants and effective Coulombic efficiency were determined by visually fitting the simulated voltage trace to the experimental data, with the resulting voltage traces plotted in Figure 4.5. For each cycle from 1 to n_{cyc}, the applied current density was first held positive for t_{on}^{+}, followed by a rest period t_{off}, then held negative for t_{on}^{-}, and lastly a final rest for t_{off}. To compare with the experimental data, the simulation results are plotted without the rest period.

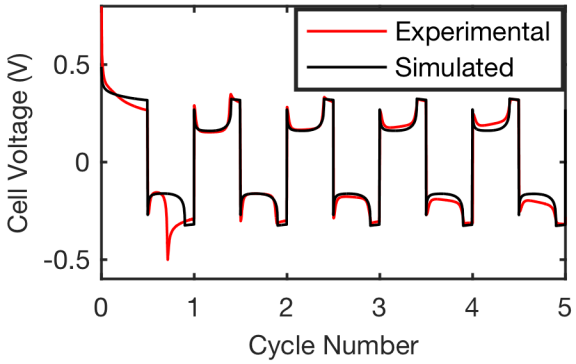

Figure 4.5. Simulated galvanostatic trace of the total cell polarization as a function of cycle number, shown in comparison with the experimental data[14] to which it was fitted.

From Figure 4.5, it is observed that overall there is very good agreement between the experimental and simulated voltage traces, and both exhibit a characteristic "peaking" voltage profile. In both cases, the cell voltage exhibits a sharp peak at the start of each half-cycle, followed by an asymmetric trough and a subsequent sharp increase leading to a blunted peak before the end of the half-cycle. We note that the model does not fully capture the experimentally observed behavior of the first cycle. This is expected because the model is parametrized for a system that has already been cycled once, which exhibits fundamentally different physical properties than the initial system. During the first half-cycle, the left electrode would experience the formation of pits in the anode surface, rather than the bulk dissolution

assumed by the model.[14] Pitting would also occur during the second peak of subsequent half-cycles, which is why there is a slight difference in the slope of the voltage trace in these regions between the model and experiment.

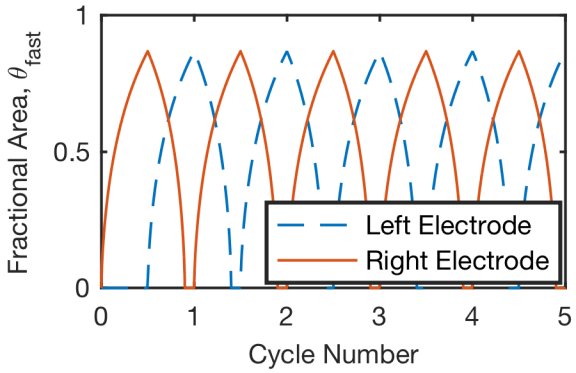

Figure 4.6. The time-dependent behavior of θ_{fast} as a function of cycle number over the course of the simulation. When the left electrode is at a maximum value of θ_{fast}, the right electrode is at a minimum value, and vice versa.

The behavior of θ_{fast} is shown in Figure 4.6, where it is observed that when one electrode is at a maximum value for the fractional surface area, the other electrode is at a value of zero. In the first half-cycle, the left electrode undergoes uniform dissolution as there are initially no dendrites on the surface. Simultaneously, lithium begins to deposit on the right electrode, increasing the value of θ_{fast} until a maximum is achieved. In all subsequent half-cycles, the electrode that was previously deposited upon will have its lithium dendrites dissolved until they have all been removed, at which point bulk dissolution will occur as pitting effects are neglected. Concurrently, the electrode which was previously dissolved will undergo lithium deposition. This parallel process where one electrode is undergoing deposition and the other dissolution can be correlated with the features of the double peak in Figure 4.5. The first peak occurs when one electrode is free of dendrites and the other is mostly covered with dendrites. The bottom of the trough in the voltage trace occurs when each electrode has significant amounts of lithium dendrites on the surface. Finally, the second peak begins once the electrode undergoing dissolution has been fully depleted of dendrites. These initial results strongly suggest that the

behavior of the galvanostatic voltage trace arises from a change in preferred kinetic pathway on the electrode surfaces during cycling.

Additionally, the concentration profile of lithium cations in the electrolyte across the entire simulation domain is plotted for 14 different times in Figure 4.7. It is observed that the concentration of lithium cations is never depleted at either electrode surface. Thus, it is expected that transport-limited behavior is not dominant in the observed voltage trace. The small electrode separation and the lack of separator in the visualization cell likely contribute to this result.

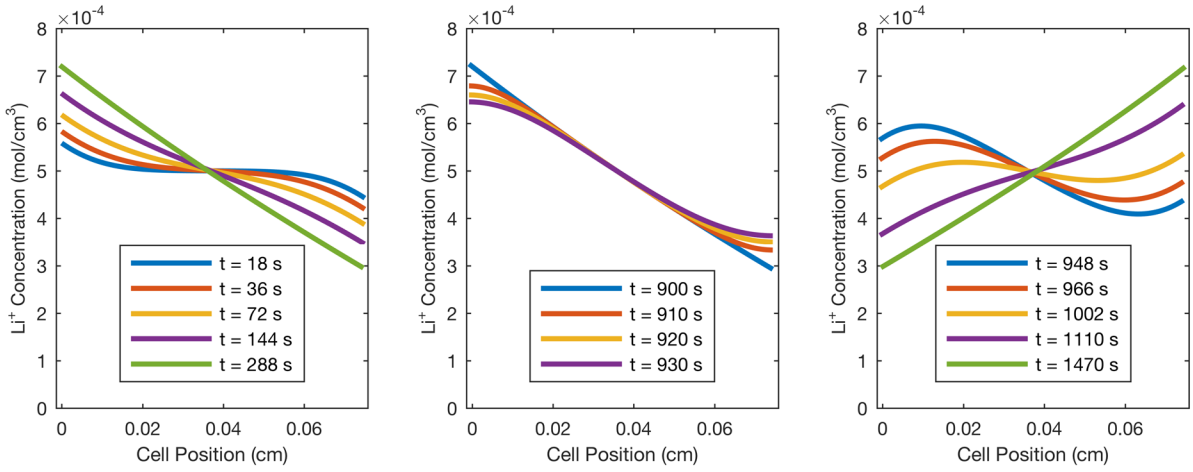

Figure 4.7. Simulated concentration profiles of lithium cations across the visualization cell during (left) the first half-cycle, (center) the first rest cycle, and (right) the second half-cycle, demonstrating the transient and pseudo steady-state behavior of the mass transport. The concentration is never depleted at either electrode surface (the edges of the domain in each plot), and thus the observed voltage trace is not expected to be dominated by transport-limited behavior.

Parametric Response of Model Behavior

To support the result of the previous subsection, a parametric sweep was performed for the values of k^0_{fast} and CE. For each of these two parameters, the remaining model parameters were held constant with their values in Table 4.2. First, two additional simulations were performed for k^0_{fast}: one with $k^0_{\text{fast}} = 9.0 \times 10^{-8}\text{cm/s}$ and one with $k^0_{\text{fast}} = 3.5 \times 10^{-7}\text{cm/s}$. The results of these two simulations are plotted in Figure 4.8 along with the first two cycles of the simulation from Table 4.2. It is observed that as k^0_{fast} is reduced from the fitted value, the trough between

the first and second voltage peak becomes shallower. The model therefore predicts that the size and shape of the trough between the double peaks in the voltage depends upon the effects of the SEI layer and the electrode morphology. When $k^0_{\text{fast}} = k^0_{\text{slow}} = 9.0 \times 10^{-8}$ cm/s, the cell voltage is nearly uniform throughout the half-cycle; the small variation is due to the change in γ as the surface morphologies evolve.

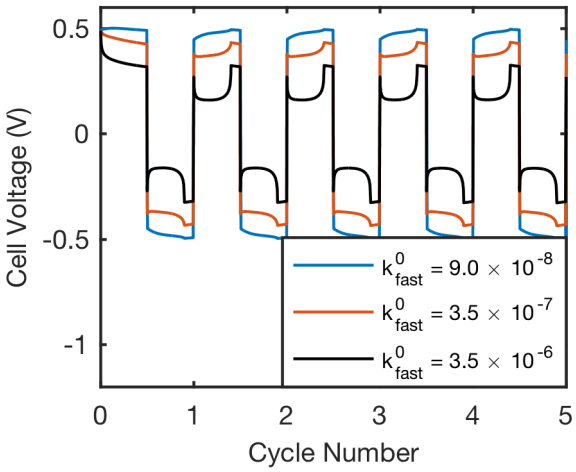

Figure 4.8. Parametric simulations with values of k^0_{fast} from 9.0×10^{-8} cm/s (equal in value to k^0_{slow}) to 3.5×10^{-6} cm/s (the fitted value). As the value of k^0_{fast} decreases, the depth of the trough between the double peaks in the cell voltage becomes shallower until it disappears completely.

Next, two additional simulations were performed for the effective Coulombic efficiency: one with $\text{CE} = 60\%$ and one with $\text{CE} = 100\%$. These two simulations are plotted along with the fitted voltage trace in Figure 4.9. It is observed that in the first half-cycle there is no difference between the different effective Coulombic efficiencies, as there are no existing dendrites on the electrode surfaces during dissolution. However, during the subsequent half-cycles there is a clear trend that as the effective Coulombic efficiency decreases, the onset of the second blunted peak occurs earlier, and the width of this peak increases. Conversely, when the effective Coulombic efficiency is 100%, there is no blunting of the second peak. As such, it appears that the width of the second peak is purely dependent upon the effective Coulombic efficiency of the system.

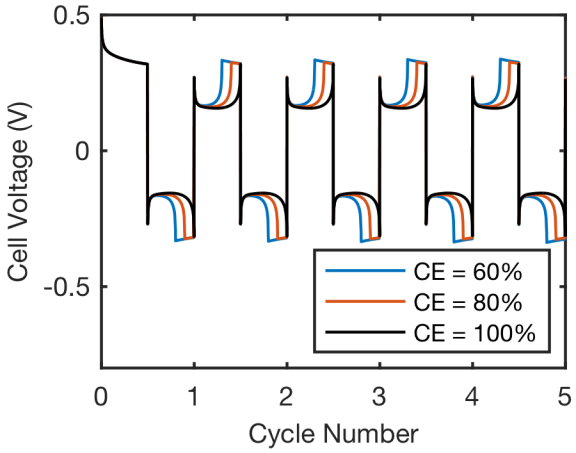

Figure 4.9. Parametric simulations with effective Coulombic efficiencies of 60%, 80%, and 100%. As the Coulombic efficiency falls below 100%, it can be observed that the onset of the second voltage peak occurs earlier in each half-cycle and that the width of the peak increases. Additionally, at 100% efficiency, the second peak is very sharp and has no plateau.

Isolated Electrode Overpotentials

With the numerical model, it is possible to explicitly track the overpotentials associated with each electrode as well as the potential drop across the electrolyte. Such a test is qualitatively similar to experimental three-electrode measurements in that it is possible to correlate changes in the overpotential of each electrode with the changes in the overall cell voltage. The results from the numerical model are displayed in Figure 4.10 along with an experimental three-electrode voltage trace (not identical to the voltage trace employed for the model fitting, refer to Ref. 14 for additional details). It can be observed that the electrode undergoing deposition (initially the right electrode in the simulation and EL-b in the experiment) in a given half-cycle features the initial voltage peak, and the electrode undergoing dissolution (initially the left electrode in the simulation and EL-a in the experiment) is the source of the second voltage peak, confirming our interpretation of Figure 4.5 and Figure 4.6. By contrast, the potential drop across the electrolyte remains relatively constant throughout a given simulation half-cycle, indicating that it is not a dominant feature in the total voltage trace. Qualitatively, the simulated overpotentials are in agreement with the experimental results, as well as the behavior of other published experimental

three-electrode measurements.[163] The only significant difference is that the simulated dissolution behavior does not exhibit a decrease in overpotential after the peak of the dissolution half-cycles, which is attributed to the fact that the model does not specifically consider pitting of the electrode surface.

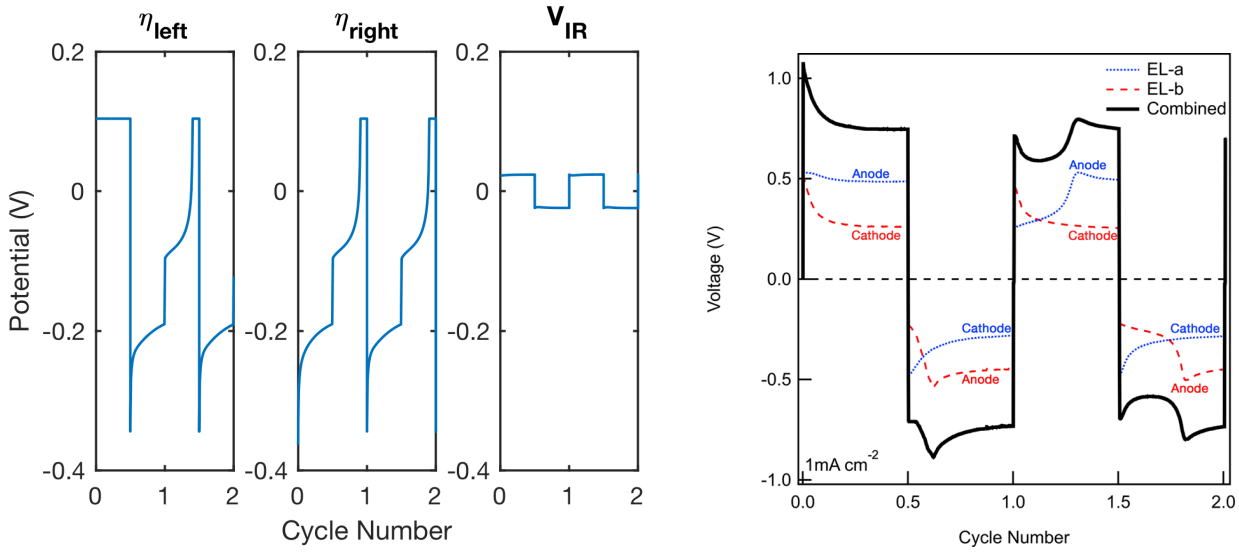

Figure 4.10. Left: the simulated overpotentials of the left and right electrodes, as well as the simulated potential drop across the electrolyte for the first two cycles. Right: an experimentally obtained three-electrode voltage trace. In a given half-cycle, the electrode undergoing deposition (initially the right electrode/EL-b) is the source of the initial voltage peak, while the electrode undergoing dissolution (initially the left electrode/EL-a) is the source of the second voltage peak. Note that the sign of the voltage trace for EL-b has been reversed from what was actually measured.

It is observed in Figure 4.10 that the simulated overpotential at each electrode is not centered about 0 V as might initially be expected. However, this offset can be readily explained by examining the governing equations. If Eq. 4.8 is solved for when there is no net current density, the resting electrode potential is obtained:

$$E_{el} = \frac{RT}{F}\ln\left(\frac{c_{Li^+}}{c_{Li}}\right) + \Phi_0 + E^{0'}, \tag{4.19}$$

which can be recognized as a modified form of the Nernst equation.[35,37] As an example, we first consider the behavior of the right electrode. The formal potential is 0 V for all of the simulations, and at $x = L$ the electrolyte potential has been pinned to 0 V. From the data presented in Figure

4.9, the lithium cation concentration ranges from around 0.3×10^{-3} mol/cm^3 at the end of deposition to around 0.7×10^{-3} mol/cm^3 at the end of dissolution. Within this concentration range, the electrode potentials at zero current range from approximately -143 mV after deposition to -121 mV after dissolution, which correspond to the observed offsets. Because both electrodes are offset by roughly equal potential values, their individual contributions are negated in the total voltage trace. If a reference electrode were explicitly included in the numerical model, then it would also have an offset potential within this range. Therefore, the simulated electrode overpotentials relative to a reference electrode would be approximately centered around 0 V.

Summary and Conclusions

The numerical model developed in Chapter 3 was extended to simulate the galvanostatic cycling of lithium/lithium symmetric cells. This required discretization of the time-dependent Poisson-Nernst-Planck equations with a mass-conserving moving-boundary method. A simplified kinetic model was derived and implemented for an idealized description of dendrite growth on the lithium electrodes. Within this model, the lithium surface was assumed to consist of kinetically fast and slow regions, with the former representing lithium dendrites that had been recently deposited and were consequently lacking a thick SEI or other passivating layer, and the latter representing lithium with a thick SEI that reduced the reaction rate. As lithium was deposited, allowing dendrite formation, the evolution of the electrode surface area led to a change in the preferred reaction kinetic pathway. When parameterized by fitting to experimental galvanostatic voltage traces, the model achieved excellent agreement with the measured cell polarization. Particularly, the model captured the characteristic double-peak behavior in the voltage trace as well as the blunting of the second peak. Additional simulations confirmed that the observed

behavior was due to a combination of the evolving surface morphology, a change in reaction kinetic pathways, and the effective Coulombic efficiency of the half-cell. Overall, the results further demonstrate the power of the morphology-aware Butler-Volmer kinetic model developed in Chapter 3 and its ability to consider evolution of the electrode morphology via coarse-grained approximations of the deposited morphology.

Chapter 5.

Numerical Modeling of Localized Corrosion Using Phase-Field and Smoothed Boundary Methods

Introduction

In this chapter,* a modeling framework is presented for localized corrosion of metals. Corrosion is the destructive degradation of a material due to chemical reactions occurring at its surface as a consequence of its surrounding environment. Prominent engineering materials, such as stainless steels and aluminum alloys are resistant to corrosive attack due to the formation of a passive, protective oxide layer on the metal's surface.[17,164–167] However, when exposed to an environment containing aggressive anions such as chlorides, these oxide layers are susceptible to partial breakdown along the surface. This leads to contact between the underlying metal and the electrolyte where dissolution of the metal, given by the anodic reaction $M \rightarrow M^{n+} + ne^{-}$, can occur at an increased rate.[17,75,77–79,84,164–167] This exposure causes pitting corrosion, a localized form of corrosion where the chemical reactions occurring within the pit (acting as the anode) provide a current that flows to a more noble metal surface (acting as the cathode). The formation and growth of these corrosion pits can accelerate degradation and lead to sudden mechanical failure of engineering materials by acting as nucleation sites for severe crack formation.[17,75,77–79,84,164,167,168] As such, predictive modeling of materials performance in corrosive operating

*Adapted from A.F. Chadwick, J.A. Stewart, R.A. Enrique, S. Du, and K. Thornton, "Numerical Modeling of Localized Corrosion Using Phase-Field and Smoothed Boundary Methods," *J. Electrochem. Soc.*, 165 (**2018**) C633.

conditions is useful in understanding corrosion pit evolution and in developing methods to mitigate its growth and impact.

In developing a physics-based model for corrosion, several underlying physical and electrochemical processes must be considered. The metal/electrolyte interface during corrosion is inherently dynamic, and its morphological evolution can be complex due to the coupling of transport kinetics, electrochemistry, and material microstructures. Specifically, corrosion pits can be narrow and deep, wide and shallow, or mostly subsurface.[164,165,169] The velocity of this interface, or equivalently the corrosion rate of the metal, depends on local microstructural features (e.g., grains, grain boundaries, precipitates, accumulation of corrosion products) as well as the properties of the given electrolyte (e.g., pH, molarity, fluid flow).[17,164,168,170–172]

Pitting corrosion occurs in three stages: passive layer breakdown, metastable pitting, and stable pit growth, each of which proceed by their own mechanism.[17,77,84,168] Many numerical modeling efforts solely focus on the stable growth stage of pitting corrosion.[53,54,75–80,82–86,172,173] As discussed in Chapter 1, these models typically employ simplified descriptions of the transport in the electrolyte and the interfacial kinetics.

In this chapter, the models of DeWitt *et al*.[33] and Enrique *et al*.[34] are adapted to develop a new smoothed-boundary-method/phase-field modeling framework to simulate pitting corrosion. This framework captures the effects of spatially varying reaction kinetics due to microstructural features as well as the effects of local variations of the concentration and electrostatic potential in the electrolyte. In order to accurately solve for the coupling between the electrochemistry and morphological evolution, we apply the smoothed boundary method (SBM),[73] which enables the enforcement of internal boundary conditions on evolving and/or complex interfaces within the computational domain. The SBM/phase-field approach automatically couples the ionic transport

and electrostatic potential in the electrolyte with the electrochemical reactions at the pit surface without any *a priori* assumption of the pit morphology or the need to maintain a conformal mesh in the simulation domain. Using the SBM, the electrostatic potential and concentrations are consistently solved for, including the effects of the spatially and temporally varying conductivity and of the diffusion potential.

To provide the diffuse interface description of the system required by the SBM, the phase-field method is employed to follow the moving metal/electrolyte interface and to distinguish the different regions of the domain (e.g., electrolyte, individual grains, or precipitates) and their interfaces. Two different approaches are employed for the phase-field model. For the first, an advective Cahn-Hilliard equation to describe the metal phase is coupled with an equilibrium Allen-Cahn equation to describe the electrolyte phase. In the second, advective Cahn-Hilliard equations are employed for both metal and electrolyte phases. The former is computationally efficient, while the latter is necessary for simulating polycrystalline systems. The velocity of the metal/electrolyte interface is calculated by Butler-Volmer reaction kinetics, which is coupled to the concentration and potential fields that are solved by the SBM. Additionally, a microscopic expression is derived and implemented for the transient evolution of the maximum possible corrosion current density at the diffuse interface. This expression allows for a smooth transition between activation-, IR-, and transport-controlled kinetic regimes. At saturation, it recovers the typical macroscopic approximation for the pseudo-steady-state limiting current.

The model is first validated against experimental results from Ernst and Newman[169] and Ghahari *et al.*[18] through simulations of corrosion for a one-dimensional (1D) pencil-type electrode and a two-dimensional (2D) foil-type electrode. For the latter case, examples are

considered both with and without an artificial inert pit cover that influences concentration diffusion paths. To consider a well-studied example,[18,75,77,79,166,169] the developed framework is initially applied to the propagation of an existing corrosion pit in 304 stainless steel that is exposed to a 1M NaCl solution under potentiostatic conditions. The capabilities and versatility of the model are further demonstrated through simulations of (i) a polycrystalline microstructure with orientation-dependent reaction kinetics and (ii) a synthetic microstructure containing secondary phases along a grain boundary (e.g., intermetallic precipitate particles). Note that this latter example is purely a demonstration of how a wide range of varying morphologies and reaction kinetics can be readily incorporated into the model and is not meant to reflect any specific stainless steel microstructure.

Model Formulation

Phase-Field Model for Interface Evolution

The phase-field method is a modeling technique that has been employed to simulate a variety of complex physical processes, including dendrite growth during solidification,[174,175] electrodeposition and physical vapor deposition,[33,34,176] grain growth,[177,178] dislocation dynamics,[179] and oxidation.[180] In this work, the evolution of the combined metal and electrolyte system is modeled using an approach similar to those of DeWitt *et al.*[33] and Enrique *et al.*[34] that were employed to simulate electrodeposition and dissolution. For this approach, the phase-field method is utilized as a tool to track the positions of the moving metal/electrolyte boundary as well as interfaces at grain boundaries or between phases within the microstructure. Following the phase-field models for electrodeposition[34] and grain growth in polycrystalline materials,[177,181,182] the microstructure is defined by a set of field variables known as order parameters, denoted by ϕ_i and ψ. Here, ϕ_i represents the i-th physical domain of the metal (e.g., the metal matrix,

secondary phase particles, or grains) and ψ represents the liquid electrolyte. These order parameters have a value of 1 within the region they represent, i.e., an order parameter representing the metal matrix would equal 1 within that domain and 0 elsewhere. The free energy functional for this system is constructed using the order parameters and their gradients:[34,182]

$$\mathcal{F} = \int_{\Omega} \left(W f_0(\{\phi_i\}, \psi) + \frac{\epsilon^2}{2} \sum_{i=1}^{N} (\nabla \phi_i)^2 + \frac{\epsilon^2}{2} (\nabla \psi)^2 \right) d\Omega, \tag{5.1a}$$

$$f_0(\{\phi_i\}, \psi) = \sum_{i=1}^{N} \left(\frac{{\phi_i}^4}{4} - \frac{{\phi_i}^2}{2} \right) + \left(\frac{\psi^4}{4} - \frac{\psi^2}{2} \right) + \gamma \sum_{i=1}^{N} \sum_{j>i}^{N} {\phi_i}^2 {\phi_j}^2 + \gamma \sum_{i=1}^{N} {\phi_i}^2 \psi^2. \tag{5.1b}$$

Here, W is the well height of the free energy, ϵ is the interfacial gradient energy coefficient, and γ is a phenomenological parameter that leads to an increase in the free energy at overlapping interfaces.

The evolution equations for this system are determined through reduction of this free energy functional.[174,183] The ϕ_i variables are evolved according to the advective Cahn-Hilliard equation[72,184]

$$\frac{\partial \phi_i}{\partial t} = \nabla \cdot \left[M(\psi) \nabla \frac{\delta \mathcal{F}}{\delta \phi_i} \right] + v |\nabla \psi|, \tag{5.2}$$

where M is the Cahn-Hilliard mobility coefficient and v is the velocity of the interface normal to the surface.[33,182,185] The variational derivative in Eq. 5.2 is given by:

$$\frac{\delta \mathcal{F}}{\delta \phi_i} = W \left(\phi_i^3 - \phi_i + 2\gamma \phi_i \sum_{j \neq i}^{N} \phi_j^2 + 2\gamma \phi_i \psi^2 \right) - \epsilon^2 \nabla^2 \phi_i. \tag{5.3}$$

The use of Cahn-Hilliard dynamics ensures conservation of mass in the bulk of each phase. However, at the metal/electrolyte interface, a source term is added to account for dissolution due to corrosion, corresponding to the second term on the right-hand side of Eq. 5.2. The normal

velocity of the interface is related to the reaction current density, i_{rxn}, by Faraday's law of electrolysis,[75,77]

$$v = -\frac{V_M i_{rxn}}{z_M F}, \tag{5.4}$$

where V_M is the molar volume of the metal, z_M is the dissolved metal cation charge number, and F is Faraday's constant. Note that the velocity of the interface has the opposite sign of the reaction current, in accordance with the convention that corrosion corresponds to positive current densities.

As the metal dissolves, the electrolyte is displaced to fill the regions where dissolution has occurred. In the present work, there are two different sets of governing equations that are examined for describing this displacement, which is represented by the evolution of ψ. The first approach describes the evolution of ψ using the Allen-Cahn equation:[34,74]

$$\frac{\partial \psi}{\partial t} = -L\frac{\delta \mathcal{F}}{\delta \psi}, \tag{5.5}$$

where L is the Allen-Cahn mobility coefficient. For the first approach, it is assumed that the displacement of the electrolyte occurs sufficiently quickly such that the liquid order parameter is always in equilibrium for the given values of ϕ_i. This equilibrium is described by

$$\frac{\delta \mathcal{F}}{\delta \psi} = W\left(\psi^3 - \psi + 2\gamma\psi\sum_{i=1}^{N}\phi_i^2\right) - \epsilon^2\nabla^2\psi = 0. \tag{5.6}$$

The second approach for simulating the evolution of ψ employs the advective Cahn-Hilliard equation, but with the opposite sign of the advective source term in Eq. 5.2 to account for the correct direction of the interfacial movement:

$$\frac{\partial \psi}{\partial t} = \nabla\cdot\left[M(\psi)\nabla\frac{\delta \mathcal{F}}{\delta \psi}\right] - v|\nabla\psi|, \tag{5.7}$$

where the variational derivative of $\mathcal{F}$ with respect to ψ is again given by Eq. 5.6, but it is no longer assumed to be zero.

To ensure that the behavior of Eqs. 5.2 and 5.7 never enters a regime where the equations become essentially hyperbolic or one where the evolution is dominated by the Mullins-Sekerka problem,[186] the interfacial mobility, M, is set as a function of the local current density. This scaling is achieved by requiring the dimensionless Peclet number, vl/M, of Eq. 5.2 to be unity, where l is a characteristic length scale chosen here to be the equilibrium interfacial thickness. For the free energy defined in Eq. 5.1, the interfacial thickness, 2δ, is given by:[182]

$$2\delta = 2\sqrt{\frac{2\epsilon^2}{W}}, \tag{5.8}$$

which, when combined with Eq. 5.4 and the definition of the Peclet number, provides the scaling relationship for the interfacial mobility:

$$M(\psi) = vl\psi = 2\frac{V_M|i_{rxn}|\psi}{z_M F}\sqrt{\frac{2\epsilon^2}{W}}. \tag{5.9}$$

which localizes the mobility to the metal/electrolyte interface to prevent coarsening of the microstructure away from the interface.

Collectively, the equations employed for the coupled Cahn-Hilliard/Allen-Cahn description of the phase-field kinetics, Eqs. 5.1-5.6, 5.8, and 5.9 are referred to as Model I. The equations for the all-Cahn-Hilliard description, Eqs. 5.1-5.4 and 5.6-5.9, are collectively referred to as Model II. The implementation of Model I is numerically less expensive than Model II. The accuracy of each approach is comparable when there is only a single solid phase present in the system, but Model I exhibits significant numerical artifacts at grain boundaries that are not observed with Model II. However, at high reaction current densities the diffuse interface in

Model II can become sharp enough such that numerical convergence of the model is prohibitively expensive. In the present work Model I is employed for all simulated systems with a single solid phase, while Model II is employed for all polycrystalline systems.

Ionic Transport Within the Electrolyte

As the metal dissolves, cations are released into the liquid electrolyte and diffuse out of the pit towards the bulk solution. The change in local concentration of charged species leads to non-uniformity of the conductivity and diffusion potential in the electrolyte, which in turn alters the electrostatic potential.[35] The spatial variation of the electrostatic potential therefore causes varying overpotentials along the metal/electrolyte interface. In this work, the electrolyte is assumed to be composed of three ionic species; an effective cation species for the dissolved metal that forms at the metal/electrolyte interface,[166] a supporting cation, and a supporting anion. The presence of hydrogen ions in the pit is neglected, as are the effects of hydrolysis on the dissolved cation concentration. It is assumed that the transport may be represented by dilute solution theory, thus the flux of each electrolyte species, $\mathbf{N}_i$, is described by the Nernst-Planck equation:[35,40]

$$\mathbf{N}_i = -D_i \nabla c_i - \frac{z_i F}{RT} D_i c_i \nabla \Phi, \tag{5.10}$$

where c_i is the concentration of the i-th species, D_i is its diffusivity, z_i is its charge state, R is the ideal gas constant, T is the absolute temperature, and Φ is the electrostatic potential in the electrolyte. The evolution of the concentration of each species in the electrolyte is described by the continuity equation:

$$\frac{\partial c_i}{\partial t} = -\nabla \cdot \mathbf{N}_i. \tag{5.11}$$

Additionally, the electrolyte is assumed to be electroneutral:

$$\sum_{i=1}^{n} z_i c_i = 0, \tag{5.12}$$

where the upper limit of n is the number of species in the electrolyte. Equation 5.12 allows the concentration evolution to be described with one less equation, as the concentration of a single reference species in Eqs. 5.10 and 5.11 can be expressed in terms of the concentrations of the remaining species. The current density is then calculated by summing the fluxes of all species:[35]

$$\mathbf{i} = -\kappa\nabla\Phi - F\sum_{j=1}^{n} z_j D_j \nabla c_j = -\kappa\nabla\Phi + F\sum_{j=1}^{n-1} z_j\left(D_n - D_j\right)\nabla c_j, \tag{5.13}$$

where κ is the local conductivity of the electrolyte, and the n-th species of the electrolyte is the reference species. The conductivity is given by:

$$\kappa = \frac{F^2}{RT}\sum_{j=1}^{n-1} z_j c_j\left(z_j D_j - z_n D_n\right), \tag{5.14}$$

which is once again calculated relative to the reference species. Lastly, the electrostatic potential needs to be determined from $\nabla \cdot \mathbf{i} = 0$, which follows from electroneutrality and charge conservation,[35] allowing Eq. 5.13 to be rewritten as:

$$0 = -\nabla \cdot (\kappa\nabla\Phi) + F\nabla \cdot \left[\sum_{j=1}^{n-1} z_j\left(D_n - D_j\right)\nabla c_j\right]. \tag{5.15}$$

In this model, the electrolyte is composed of the effective metal cations, a supporting cation, and a supporting anion (i.e., $n = 3$). The anion is eliminated via Eq. 5.12, and thus only the concentrations of the effective metal cations and the supporting electrolyte cations (abbreviated c_M and c_+, respectively) need to be directly solved.

Smoothed Boundary Method Formulation

As in Refs. 33,34,73, and 187, the transport in the electrolyte is coupled with the phase-field method via the SBM so that transport only occurs within the electrolyte where $\psi > 0$. The SBM is a mathematical technique that reformulates a given equation such that it is solved in an arbitrarily shaped domain represented by a phase-field-like order parameter.[73] The SBM is a relatively recent technique, but it has been successfully utilized to study problems involving moving boundaries, such as quantum dot growth,[188,189] nanopore formation during anodization,[190] template-directed eutectic solidification,[191] and, as previously mentioned, electrodeposition.[33,34] Furthermore, the SBM formulations of the governing equations (Eqs. 5.11 and 5.15) automatically incorporate the boundary conditions at the metal/electrolyte interface. This presents an advantage over other methods, as the potentially complex interfacial geometry can be embedded in a regularly shaped computational domain (e.g., a cube) that is more easily discretized. The SBM reformulated governing equations are:

$$\frac{\partial c_i}{\partial t} = \frac{1}{\psi}\nabla\cdot(\psi D_i \nabla c_i) + \frac{1}{\psi}\left(\frac{z_i F}{RT}\nabla\cdot(\psi D_i c_i \nabla\Phi)\right) + \frac{|\nabla\psi|}{\psi}\left(\frac{i_{rxn}}{z_i F}\right), \tag{5.16}$$

$$\nabla\cdot(\psi\kappa\nabla\Phi) = F\nabla\cdot\left[\psi\sum_{j=1}^{n-1} z_j\left(D_n - D_j\right)\nabla c_j\right] + |\nabla\psi| i_{rxn}, \tag{5.17}$$

from which the ionic concentrations and the electrostatic potential are solved in the electrolyte. Note that, in Eq. 5.16, i_{rxn} is only nonzero for the corroding metal; thus, there is an implied no-flux boundary condition for supporting electrolyte species at the metal/electrolyte interface.

Electrochemical Kinetics at the Interface

Anodic reactions can occur within the corrosion pit and on the surrounding metal surface. In stainless steels, at high applied potentials the corrosion reaction proceeds fast enough such that

the solubility of the salts of the alloying elements is exceeded, causing the precipitation of a resistive salt layer.[192] Once this occurs, the salt layer prevents the reaction from occurring faster than ions can be transported away from its surface, keeping the metal ion concentration at saturation at the interface. Within the present model, the effect of saturation is included by defining a Butler-Volmer-type kinetic expression for i_{rxn} that incorporates a maximum corrosion current density:[35,37]

$$\frac{i_{rxn}}{i_{corr}} = \left(1 - \frac{i_{rxn}}{i_{max,c}}\right) \exp\left(\frac{z_M(1-\beta)F}{RT}\eta\right), \tag{5.18}$$

where i_{corr} is the corrosion current density, $i_{max,c}$ is the maximum possible reaction current density, z_M is the charge of the metal cation, β is the charge transfer symmetry factor, and η is the overpotential. Here, the overpotential is defined as $\eta = V_s - E_{corr} - \Phi$, where V_s is the applied potential and E_{corr} is the corrosion potential of the metal. The value of $i_{max,c}$ is a time-dependent, spatially varying quantity defined by:

$$i_{max,c} = \left(\frac{z_M F}{1 - c_M V_M}\right)\left[\frac{2\delta}{\tau}\left(c_{M,sat} - c_M\right) + \left(D_M \nabla c_M + z_M \frac{F}{RT} D_M c_M \nabla\Phi\right) \cdot \mathbf{n}\right], \tag{5.19}$$

where $c_{M,sat}$ is the saturation concentration of the metal ions in solution and $2\delta/\tau$ is a characteristic velocity of ion transport across the diffuse interface. The bracketed terms represent the contributions to the maximum current density from both how far the electrolyte is from saturation at a point in time as well as the rate of transport of ions into the electrolyte. The value of $2\delta/\tau$ depends upon which transport process has the smallest characteristic time scale, and hence the largest characteristic velocity:

$$\frac{2\delta}{\tau} = \max\left(\frac{D_M}{2\delta}, \left|\frac{z_M D_M F \nabla\Phi}{RT}\right|\right). \tag{5.20}$$

With the terms in parentheses corresponding to the characteristic velocities of diffusion and migration, respectively. A detailed derivation of Eqs. 5.19 and 5.20 is presented in Appendix A.

At saturation, the first term on the right hand side of Eq. 5.19 vanishes and the equation recovers the Rankine-Hugoniot jump condition employed by other studies.[75,193] The maximum current must then correspondingly decrease until it matches the rate at which ions are able to diffuse away from the metal surface.[36,37] When the potential gradient becomes negligible, Eq. 5.19 recovers the typical expression for the macroscopic limiting current at saturation.[18,36] Thus, the reaction current density defined by Eqs. 5.18 through 5.20 allow the model to smoothly transition between activation-, IR-, and transport-controlled kinetic regimes. As a benefit, a Dirichlet boundary condition is no longer required for Eq. 5.16 in order to capture saturation. Instead, the condition is indirectly imposed through the flux boundary condition. It should be noted that Eq. 5.19 includes contributions to the flux from both migration and diffusion even at saturation. Thus, we describe the reaction kinetics as being transport-controlled. If the gradient of the electrostatic potential is negligible, the limiting kinetics will be identical to typical descriptions of diffusion-controlled behavior.[17,166]

Although the reaction current is defined as a continuous field throughout the entire domain, its effect is localized to the metal/electrolyte interface by the value of $|\nabla\psi|$, which is only nonzero at the interface. In a system with multiple metallic phases, each order parameter has its own set of kinetic constants and, by extension, its own reaction current defined by Eq. 5.18. However, to solve the electrostatic potential and the metal cation concentration, it is necessary to combine the individual reaction currents into a single spatially dependent field. This is achieved by defining a weighting parameter with respect to the individual order parameters

(similar to those used in Refs. 194 and 195 in the context of spatially varying dislocation densities for studies of recrystallization),

$$\xi_i = \frac{\phi_i}{\sum_{j=1}^{N} \phi_j}, \tag{5.21}$$

which is then employed to define the effective reaction rate:

$$i_{rxn} = \sum_{j=1}^{N} \xi_j i_{rxn,j}, \tag{5.22}$$

where $i_{rxn,j}$ is the reaction current defined according to Eq. 5.18 with the kinetic constants that correspond to order parameter j.

It is also possible to include the effects of anisotropy in the reaction kinetics. Experimentally, it has been observed that crystallographic orientation has a measurable effect on the corrosion behavior of stainless steels, with the densely packed {111} planes corroding roughly three times more slowly than {100} and {110} planes.[196] Thus, in polycrystalline systems, some grains experience slower corrosion kinetics than others. This effect can be included by introducing an anisotropic function for the corrosion current density that varies with the orientation of the crystal, which must be defined for each of the grains:

$$i_{corr,j}^{eff} = i_{corr,j} f\left(\theta_j, \mathbf{n}\right), \tag{5.23}$$

where $f(\theta_j, \mathbf{n})$ is a function that modifies the magnitude of the corrosion current density depending on the angle between the [01] direction of the j-th crystal and the vertical simulation axis, θ_j, and the inward unit normal vector with respect to the electrolyte at the metal/electrolyte interface, $\mathbf{n} = \nabla\psi/|\nabla\psi|$. We employ the following form of $f(\theta_j, \mathbf{n})$:

$$f(\theta_j, \mathbf{n}) = \frac{1}{2}\cos\left(4\left(\theta_{\mathbf{n}} - \theta_j\right)\right) + 1, \tag{5.24}$$

where $\theta_{\mathbf{n}}$ is the angle between $\mathbf{n}$ and the vertical simulation axis. This function represents a fourfold symmetry with maxima and minima at the <11> and <10> directions of a 2D crystal, respectively. The distribution of θ_j depends on the texture of the grains; in this study it is assumed that they are randomly oriented. Therefore, the values of θ_j for each order parameter (equivalently, each grain) are randomly assigned between $\pm\pi/2$. The values of $\theta_{\mathbf{n}}$ are calculated locally along the metal/electrolyte interface by:

$$\theta_{\mathbf{n}} = \cos^{-1}\left(\boldsymbol{e}_{\mathbf{y}} \cdot \mathbf{n}\right), \tag{5.25}$$

where $\boldsymbol{e}_{\mathbf{y}}$ is the unit normal vector parallel to the vertical axis of the Cartesian coordinate system. To prevent the corners of the kinetically preferred morphology from becoming infinitely sharp, a cutoff is implemented based on the mean curvature, H, of the electrolyte order parameter in a similar manner as Refs. 33 and 188:

$$H = \nabla \cdot \left(\frac{\nabla\psi}{|\nabla\psi|}\right). \tag{5.26}$$

In the present work, the formation of sharp corners occurs where the value of H is strongly negative. Therefore, when $H < H_C$, where H_C is the critical curvature for the cutoff, the corrosion reaction is disabled and i_{rxn} is locally set to zero.

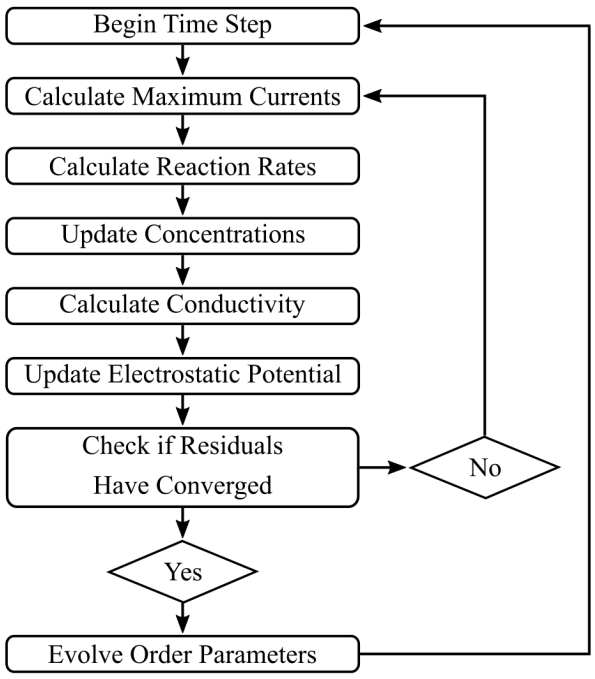

Figure 5.1. A flowchart of the general structure of the transport and phase-field solvers employed by the model. At the start of a time step, the model enters a coupled, self-consistent loop. During each subiteration, all quantities associated with transport in the electrolyte (the reaction rates, concentrations, conductivity, and electrostatic potential) are solved. The self-consistent loop is exited once all residuals have converged for the transport quantities, at which point the order parameters are evolved and the time step is advanced.

Numerical Methods and Model Parameters

The governing equations, Eqs. 5.2, 5.5, 5.7, and 5.16-19, are solved using the finite difference method with second-order central differences for all spatial derivatives. The temporal derivatives in Eqs. 5.2, 5.7, and 5.16 are discretized with implicit backward Euler time stepping, due to its inherent stability.[197] Equations 5.2 and 5.5 (Model I) or 5.2 and 5.7 (Model II) are simultaneously solved in a coupled fashion with point-wise successive over-relaxation (SOR).[198] The phase-field solver is iterated until the order parameter residual is 10^{-9}. Equations 5.16-19 are also solved simultaneously, with Eqs. 5.16 and 5.17 using pointwise SOR. At the beginning of every time step, the values of the concentrations, potential, conductivity, maximum current densities, and reaction current densities are initialized from the previous time step. Within each iteration of the pointwise solver, the new estimate of one field is calculated based on the current

values of the remaining quantities, which is repeated for all fields. The residuals for each field solved are then calculated with all of the updated values. This iterative process is repeated until the maximum residuals are less than 1 μM in concentrations and 1 μV in potential. Decreasing these tolerances had a minimal effect on the final solution. A flowchart summarizing the coupled process for solving the transport equations is presented in Figure 5.1. The SBM governing equations are solved everywhere in the domain. However, the values of the concentration and the electrostatic potential outside of the electrolyte, while numerically necessary to satisfy the continuity of the solution to the governing equations, do not have a specific physical meaning and are discarded during analysis.

The model was programmed in Fortran 2008, and the code was parallelized using the Message Passing Interface (MPI) standard to increase performance. On a quad-core MacBook Pro laptop, typical 1D simulations ran for 15 to 40 minutes, depending on the applied potential. For the 2D simulations, the typical runtime was 1 to 3 hours on a single Intel Xeon-based node with 24 Haswell architecture cores operating at 2.50 GHz. Due to larger domain sizes and longer simulated times, the simulations for experimental comparison were significantly more expensive, with the large uncoated and coated pits respectively requiring approximately 55 hours and 96 hours on 12 Intel Xeon-based nodes, each with 48 Skylake architecture cores operating at 2.10 GHz. This expense could in principal be reduced by modifying the over-relaxation parameters and using an adaptive time step size, but such optimization was not pursued in this work.

The 1D simulations in this work employ a uniform mesh of 900 grid points (physical domain size of 180 μm) and most of the 2D simulations employ a uniform mesh of 512 × 256 grid points (102.4 μm × 51.2 μm). The simulations for experimental comparison employed a mesh of 2560 × 1280 grid points (512 μm × 256 μm). The parameters employed in these

simulations are summarized in Table 5.1. The Butler-Volmer kinetic parameters and the saturation concentration correspond to 304 stainless steel in a neutral 1M NaCl solution and are obtained from previous experimental studies.[166,192] For the diffusivity, charge, and molar volume of the dissolving metal species, the single effective species is defined for the main elements of 304 stainless steel (Fe, 10 wt% Ni, 19 wt% Cr, and 1 wt% Mn).[76,166] The effective diffusivity and molar volume are calculated from handbook data[199] via a weighted average of the mass fractions of the constituent species. The diffusivity values employed in this calculation are for the constituent ions at infinite dilution, thus, it is likely that they are an overestimation at higher concentrations. An effective charge number is determined via a weighted average of their mole fractions.[76] Furthermore, it is assumed that the main ions in the supporting electrolyte are Na^+ and Cl^-. All potentials are defined relative to a saturated calomel electrode (SCE).

For the phase-field method, the coefficients W and γ are taken to be 1 and 1.5, respectively, which ensures that overlapping interfaces are appropriately penalized while maintaining the sum of the field variables to be approximately unity.[34,182] The gradient energy coefficient, ϵ^2, is chosen to ensure the diffuse interfaces remain 4-6 grid points wide throughout the simulation.

Table 5.1. Numerical and physical parameters used in this chapter. * Indicates values calculated as weighted average from values found in reference.

Parameter	Value	Units	Reference
Δt	1D: 5×10^{-3} 2D: 5×10^{-4}	s s	
ϵ	200	nm	
D_M	6.90×10^{-6}	cm^2/s	[199]*
D_+	13.32×10^{-6}	cm^2/s	[199]
D_-	20.32×10^{-6}	cm^2/s	[199]
z_M	2.20		[199]*
z_+	1.0		[199]
z_-	-1.0		[199]
V_M	6.92	$\mathrm{cm}^3/\mathrm{mol}$	[199]*
$c_{M,\mathrm{sat}}$	5.1	M	[192]
T	298	K	
E_{corr}	-0.24	V vs. SCE	[166]
i_{corr}	9.90×10^{-4}	A/cm^2	[166]
β	0.35		[166]

Simulation Results and Discussion

Pencil Electrode

The modeling framework (with Model I for the phase-field kinetics) described in the previous section is first utilized to simulate corrosion of a so-called pencil electrode, where a thin wire has been coated on all sides to only expose a small tip, making it essentially a 1D problem. The behavior of the corrosion pit depth and current density over time are examined for various applied potentials. To describe the corroding metallic phase, only one ϕ_i variable is required. No-flux boundary conditions are imposed on both ϕ_i as well as ψ. At the edge of the domain corresponding to the bulk electrolyte, Dirichlet boundary conditions of $c_M = 0$ M, $c_+ = 1$ M, and $\Phi = 0$ V vs. SCE are applied, and no-flux boundaries are enforced at the opposite edge of the computational domain. For the initial condition, 176 μm is initialized as the metal and 4 μm is initialized to be the electrolyte. All concentrations are initialized to their bulk electrolyte values, and the potential is initialized to 0 V vs. SCE. With this geometry, corrosion simulations are

performed for a total simulated evolution time of 150 s with applied potentials of -150, -100, -60, -20, and 100 mV vs. SCE.

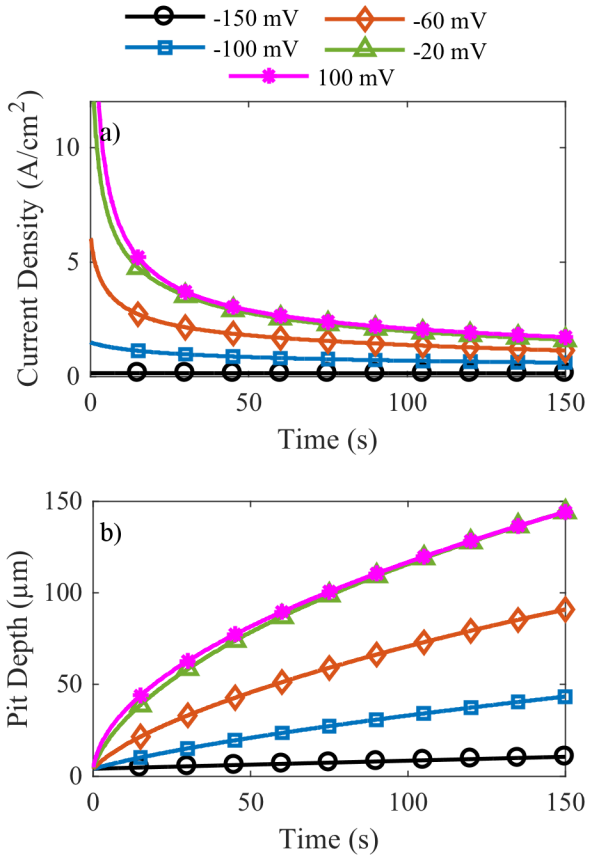

Figure 5.2. Simulation results for (a) current density vs. time behavior and (b) corrosion pit depth vs. time behavior at various applied potentials against an SCE reference for a 1D pencil electrode.

The pencil electrode simulation results are presented in Figure 5.2, with the interfacial current density and the corrosion pit depth shown in Figure 5.2a and Figure 5.2b, respectively. From this series of simulations, several observations are made. As the applied potential increases, so does the depth of the corrosion pit at a given time, which is expected. Additionally, at higher potentials, a Cottrell-like transient in the current density is observed where an initial spike in the current decays towards a steady-state response due to the increased overpotential at the surface. This same response has been observed experimentally for both 304 stainless steel and the aluminum alloy 7004-T6.[169,200] Increasing the applied potential beyond 100 mV vs. SCE

negligibly affected the simulated current density and pit depth, indicating that a transport-controlled kinetic regime has been achieved during the simulated time. If longer times were examined for the lower applied potentials, it is likely they would also become transport-limited.

At the lowest applied potential (-150 mV vs. SCE), the pit depth generally increases linearly as a function of time, although a large overall increase is not observed. As higher potentials are applied, the pit depth becomes larger, with an increasing amount of sublinearity as a function of time. To gain insight into whether the behavior is due to an activation-, IR-, or transport-controlled regime,[166] the concentration and the electrostatic potential at the metal/electrolyte interface are plotted in Figure 5.3. At -150 mV vs. SCE, it is observed that the potential at the interface is negligibly small, which is indicative of the corrosion process being almost entirely activation-controlled.[166] For the intermediate applied potentials of -100 and -60 mV vs. SCE, the potential at the interface changes significantly over time. However, the concentration remains far from saturation; thus, the system is predominantly IR-controlled over the examined time scale. At -20 mV vs. SCE, over the first 50 seconds of simulated time the kinetics is strongly IR-controlled, as evidenced by the sharp transient in the potential at the interface. However, around 50 seconds the concentration transient begins to level off and asymptotically approach saturation, indicating that the reaction kinetics is beginning to become transport-controlled. At 100 mV vs. SCE, the concentration almost immediately approaches saturation, confirming the existence of a transport-controlled regime.

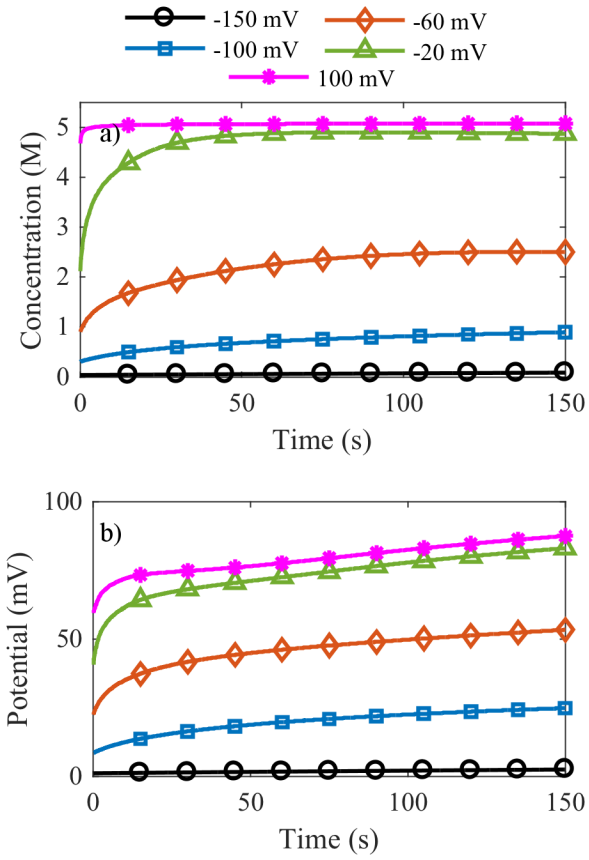

Figure 5.3. Simulation results for (a) the concentration and (b) the potential at the metal/electrolyte interface as a function of time for various applied potentials against an SCE reference for a 1D pencil electrode. After a rapid initial increase, the concentration continues to increase over time, approaching saturation for the higher applied potentials. However, the potential at the interface has not yet reached a constant value.

According to Frankel,[17] both IR- and diffusion-controlled kinetics lead to a current density with a $t^{-1/2}$ dependence, but the slopes are not necessarily the same. Figure 5.4 shows the inverse current density as a function of the square root of the time for the -20 mV vs. SCE applied potential. Here, there are two distinct regimes where the response is linear with a noticeable change in slope between them. The first and second regimes correspond to IR-controlled and transport-controlled regimes, respectively, with the transition occurring when the concentration in Figure 5.3 begins to approach saturation. In Figure 5.5, which shows the inverse current density as a function of the square root of time for the case with 100 mV vs. SCE applied potential, there is no discernable change in slope, indicating that the kinetic response almost

immediately becomes transport-controlled. The overall transition from activation- to transport-controlled behavior with increasing applied potentials is qualitatively similar to previous simulation results.[75,77–79] As in Mai *et al.*[79] and Chen and Bobaru,[78] the transition observed here is smooth. On the other hand, such a smooth transition was not observed by Scheiner and Hellmich[75] and Duddu,[77] which is likely due to the change in concentration boundary conditions employed in their models at saturation. However, Mai *et al.*[79] neglected the effects of migration and Chen and Bobaru[78] assumed its effects were described by an overall effective diffusivity of the ionic species. Thus, these models essentially proceed directly from activation to diffusion control. In comparison, the model presented here directly considers migration and its effects on the overpotential at the metal/electrolyte interface, which allows for the appearance of an IR-controlled kinetic regime between activation- and transport-controlled regimes.

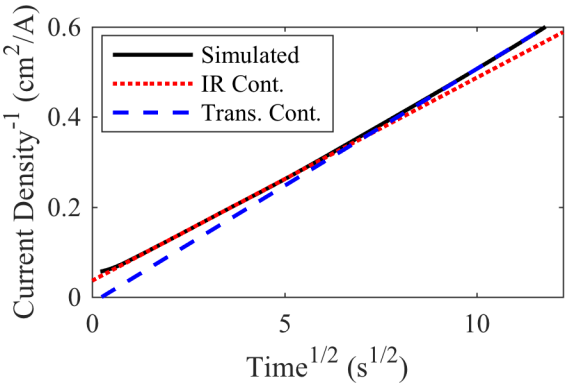

Figure 5.4. The inverse current density as a function of the square root of time for the pencil electrode at an applied potential of -20 mV vs. SCE. After a brief activation-controlled region, there are distinct IR-controlled regime (black curve overlapping with red dotted line) and transport-controlled regime (overlapping with blue dashed line). A clear inflection point exists around 7.7 $s^{1/2}$.

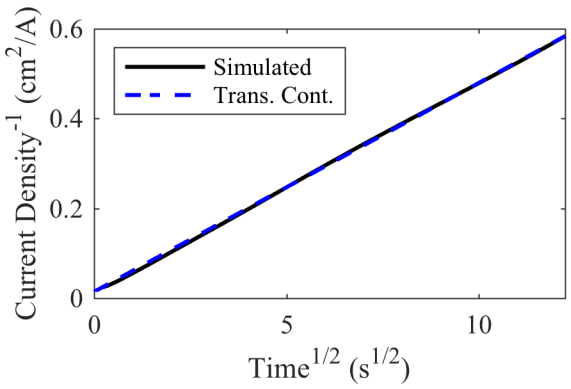

Figure 5.5. The inverse current density as a function of the square root of time for the pencil electrode at an applied potential of 100 mV vs. SCE. Unlike in Fig. 4, there is no obvious inflection point, indicating that the kinetics almost immediately become transport-controlled (blue dashed line).

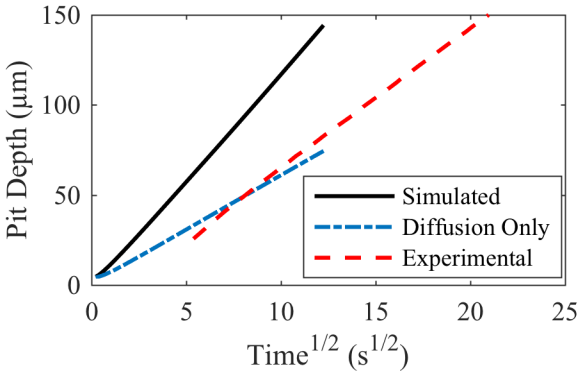

Figure 5.6. The corrosion pit depth as a function of the square root of time for the 1D electrode at an applied potential of 600 mV vs. SCE. The solid black and dash-dot blue lines are simulated, with the latter assuming a constant potential of 0 V in the electrolyte. The experimental results (red dashed line) are from Ernst and Newman.[169]

The model is also compared against experimental data. Figure 5.6 shows a comparison of the model at an applied potential of 600 mV vs. SCE against experimental results for a pencil electrode from the work of Ernst and Newman.[169] The solid black line represents the pit depth predicted by the full model, the dash-dot blue line is predicted when migration is neglected, and the dashed red line is the experimental result. It is observed that both of the simulated conditions have a linear response as a function of the square root of time that is indicative of transport-controlled kinetics.[17,51] If a linear trend is fitted to the data in Figure 5.6, the full simulation, diffusion only, and experimental results have slopes of 11.91, 6.02, and 7.74 µm $s^{-1/2}$,

respectively. When migration is considered, the slope of the simulated line is 54% greater than that of the experiment, which indicates that transport in the electrolyte is overpredicted. Conversely, without migration the slope of the simulation is 22% smaller than that of the experiment, indicating that transport is underpredicted. These differences can be attributed to multiple factors. First, the effective diffusivity in the model was calculated from data at infinite dilution, and thus the diffusivities of the ions would likely be lower at higher concentrations. Gaudet *et al.*[166] calculated the effective diffusivity of the metal ions both with and without consideration of migration, finding that they were able to achieve reasonable fits by including the effect of migration in a form of an effective diffusivity. Compared to their effective diffusivity value of 8.24×10^{-6} cm^2/s, the diffusivity in Table 5.1 is 16% smaller for the diffusion-only case. When migration was explicitly considered, Gaudet *et al.*[166] fitted a diffusivity of 4.98×10^{-6} cm^2/s, for which the diffusivity in Table 5.1 is 38% greater. The differences in diffusivities are comparable to the differences in the slopes. Additionally, previous experimental studies[51,192,201] have indicated that a resistive salt layer precipitates on the pit surface that has a strong effect on the limiting current and is responsible for a large portion of the electrostatic potential drop near the interface. The treatment of the salt layer is implicitly embedded in Eqs. 5.18-5.20, where the primary effect of any precipitation is to prevent the metal ion concentration from exceeding its saturation condition. However, this treatment is likely insufficient to capture the effect of the salt layer quantitatively, and thus may be a source of discrepancy between the model and experimental results. Finally, the exact geometry of the experimental setup was not available in the literature. By having a boundary condition of $\Phi = 0$ V at the pit opening, the model assumes that the reference electrode is in near-intimate contact with the metal surface, which may not be representative of the actual cell geometry. This may lead to an overestimation of the potential

gradient, which is consistent with the fact that transport proceeds more rapidly in the simulation than is observed experimentally. Experimental studies[87,202] and modeling studies[85,86] of pitting corrosion have indicated that a well-characterized cell geometry is essential in understanding the effects of migration. Beyond corrosion, the geometry has also been demonstrated to have a strong impact on the measured kinetic behavior in other models of electrodeposition and electrodissolution.[131]

Single Pit Growth With and Without a Protective Surface Layer

Next, 2D simulations are performed to study the morphological evolution of a single corrosion pit for the cases where (i) the metal surface is completely exposed to the electrolyte and (ii) a protective layer is present on the metal surface, but a pinhole exists above the center of the pit. The initial condition of the 2D simulation domain is presented in Figure 5.7. Applied potentials of -75 mV vs. SCE and 600 mV vs. SCE with an initial corrosion pit with a radius of 4 μm are considered. The simulation of case (ii) at 600 mV vs. SCE is intended to replicate the experimental results of Ernst and Newman,[169] who studied the behavior of a foil electrode that was coated with a protective lacquer except for a small pinhole. This also serves as a benchmark of the predicted corrosion behavior against the work of Duddu[77] and Mai *et al.*,[79] who each simulated the same condition with their respective models. All of the examples in this section employ Model I for the phase-field kinetics.

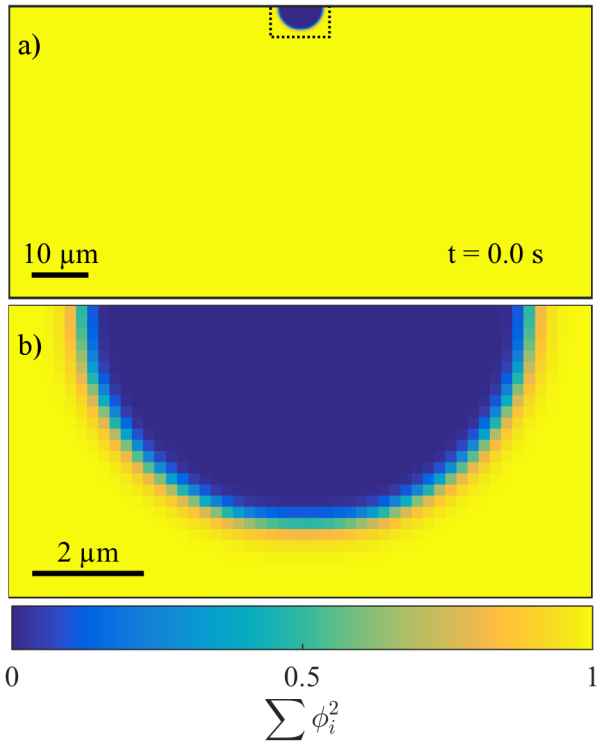

Figure 5.7. The initial condition of the 2D simulation domain, (a) depicting the entire geometry and (b) depicting the vicinity of the pit in the dotted box at higher magnification. The domain is initialized with a small semicircular pit in the surrounding metal. It is always assumed that the ion concentrations and electrostatic potential are fixed along the initial pit opening. If there is no protective layer, the ions are free to diffuse towards the bulk of electrolyte as the pit grows outwards. Otherwise, the ion flux outside of the initial pit to the bulk electrolyte is set to zero.

For both cases (i) and (ii), a single ϕ_i variable is used to describe the metal; no-flux boundary conditions are applied to ϕ_i and ψ on all sides of the rectangular computational domain. For the concentrations and the electrostatic potential, no-flux boundary conditions are applied where the domain is not contacting the corroding surface (left, right, and bottom in Figure 5.7). Along the initial opening of the pit, boundary conditions of $c_M = 0$ M, $c_+ = 1$ M, and $\Phi = 0$ V vs. SCE are enforced, and the remaining boundary conditions depend on whether a protective layer is included in the model. When there is no protection layer, these boundary conditions extend along the entire top of the computational domain. If a protective layer is on the electrode, no-flux boundary conditions are enforced outside of the initial pit opening. In the latter case, the electrolyte is only able to diffuse into the bulk solution through the pinhole. It is

assumed that the protective layer remains intact throughout the simulation; even though metal corrodes beneath the protective layer, no additional diffusion pathways form between the pit and the bulk electrolyte. As in the 1D examples, the pit cavity concentrations are initialized to their bulk electrolyte values and the potential is initialized to 0 V vs. SCE.

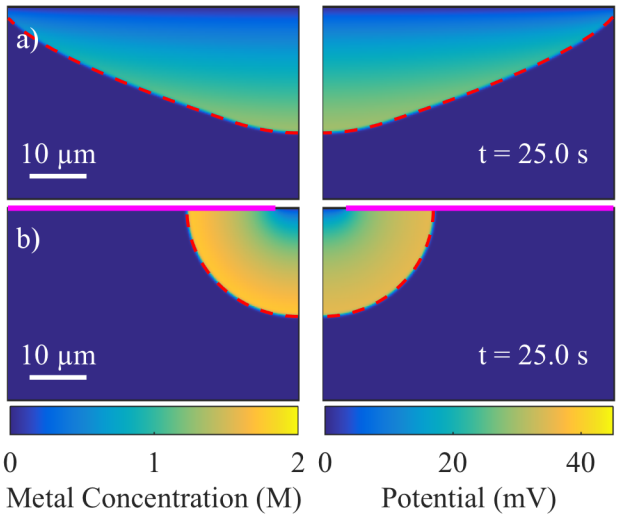

Figure 5.8. Simulated pit morphology with (left) the concentration profile and (right) electrostatic potential at 30 s for a -75 mV vs. SCE applied potential with (a) no protective layer and (b) a protective layer covering all of the top surface except a central 8 µm pinhole. The dotted red lines indicate the location of the metal/electrolyte interface, and the solid magenta line in (b) indicates the location of the inert coating. The profiles are symmetric around the vertical centerline. Note that the bottom portion of the computational domain has been removed to show the pit more clearly.

The resulting corrosion pit morphology and electrolyte concentration profile for both cases at the -75 mV vs. SCE applied potential are presented in Figure 5.8, where the metal/electrolyte boundary is denoted by a dotted red line. Both pits start with the same initial semicircular geometry as shown in Figure 5.7. However, once the metal is partially dissolved, the morphology differs between the two cases. The uncoated pit evolves into a wide, comparatively shallow trench (Figure 5.8a) while the coated pit remains a semicircle (Figure 5.8b). The differences in morphologies can be directly attributed to a change in the overall transport within the pit, as explained below.

For the uncoated case, the dissolved metal cation concentration is higher at the bottom of the pit than along the side, but it is far from saturation. As in the coated case, the entirety of the metal/electrolyte interface is in an IR-controlled kinetic regime, but the strength of this regime varies from the pit opening to the bottom of the pit due to variations in the electrostatic potential. The electrostatic potential is approximately 35 mV higher at the bottom than at the pit opening, which corresponds to an overpotential that is about 21% lower. Additionally, material that dissolves near the pit opening can rapidly diffuse into the bulk electrolyte. This results in higher current near the pit opening than at the bottom that in turn causes the pit to grow outward into the wide, shallow shape that exposes new diffusion pathways for the dissolved cations. With the protective coating, but otherwise identical simulation conditions, the concentration is both higher and more uniform along the metal/electrolyte interface than in the uncoated example. Although the concentration still has not reached saturation, the coating restricts the diffusion pathways such that the dissolved cations can only reach the bulk electrolyte through the initial pinhole. The restricted access leads to a higher electrostatic potential and a smaller overpotential around the entire pit. This results in a stronger—but uniform—IR-controlled condition in the coated case with a lower overall corrosion rate as compared to the uncoated case. The uniformity of the corrosion rate leads to the semicircular geometry being preserved.

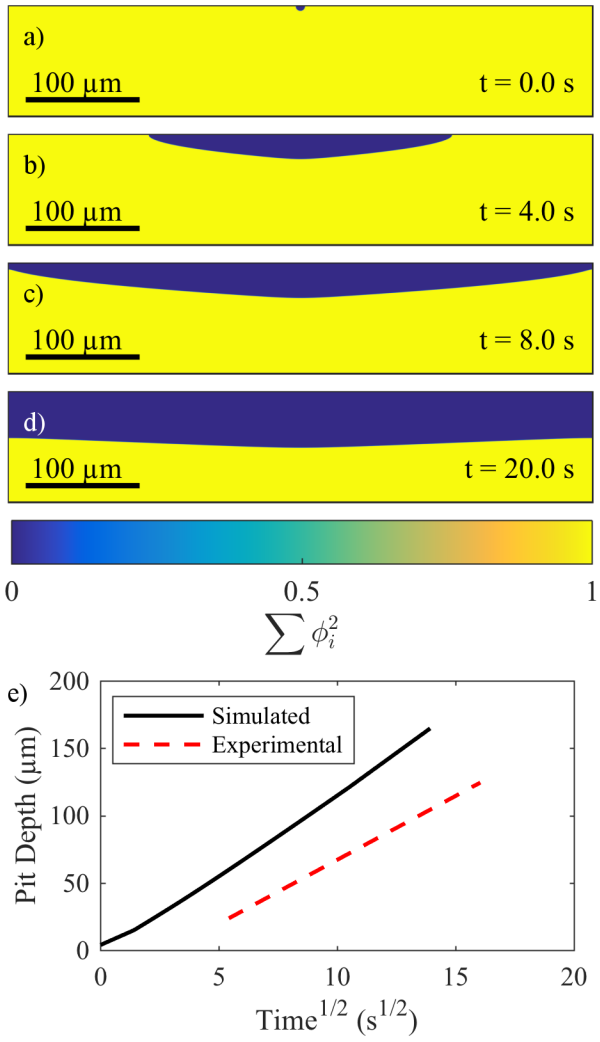

Figure 5.9. (a-d) Simulated pit morphology for an uncoated foil at 600 mV vs. SCE for a pit that fails to form a lacy cover during corrosion. The initial pit (a) rapidly corrodes outward to form a wide, shallow pit (b and c), with the pit eventually becoming an essentially 1D pit (d). The pit depth over the square root of time (e) is also shown in comparison to a similar pit observed by Ghahari *et al.*[18] Note that the bottom portion of the computational domain has been removed to more clearly show the corroding region.

The behavior of the model for 2D pits can also be examined at higher applied potentials. Figure 5.9 shows the evolution of the pit morphology for an uncoated pit at an applied potential of 600 mV vs. SCE. The initial pit (Figure 5.9a) rapidly corrodes near the pit opening as there is no barrier for a cation to be transported into the bulk electrolyte. This causes a very wide but shallow pit to form (Figure 5.9b) that after about eight seconds reaches the edge of the computational domain (Figure 5.9c). At this point, the pit continues to corrode, but the curvature

of the interface decreases until the pit essentially becomes 1D (Figure 5.9d). The overall pit depth is linear with respect to the square root of time throughout the regime where the 1D condition exists, indicating that the kinetics is transport-controlled. Ghahari *et al.*[18] observed similar behavior for a pit that failed to form a lacy cover. The linear trend for their results is included in Figure 5.9e along with the simulated pit depth; the simulation overpredicts the corrosion rate overall and yields a higher slope in the transport-controlled regime as compared to experiment.

For the coated pit at an applied potential of 600 mV vs. SCE, which is analogous to the coated pit examined experimentally by Ernst and Newman,[169] the final morphology and the pit depth over the square root of time are shown in Figure 5.10. Here, it is observed that the initial pit (*cf.* Figure 5.7 and Figure 5.9a) grows into a large semicircular shape, just as in the result for the -75 mV vs. SCE applied potential. Additionally, at the higher potential, the kinetics is transport-controlled, which is confirmed by the linear trend in the pit depth as a function of the square root of time. For the coated pit observed by Ernst and Newman,[169] the pit had a radius of about 190-200 μm after 720 seconds at a 600 mV vs. SCE applied potential. This point is included for comparison in Figure 5.10b. Here, the coated pit is predicted to be smaller than in the experimental result, with a depth of 157 μm. However, this is better agreement than observed by Duddu[77] and Mai *et al.*,[79] whose models both predicted a pit depth of about 120 μm at 720 seconds. The result from Duddu[77] is also included in Figure 5.10b. The results from Mai *et al.*[79] are omitted because they would overlap with the result from Duddu.[77]

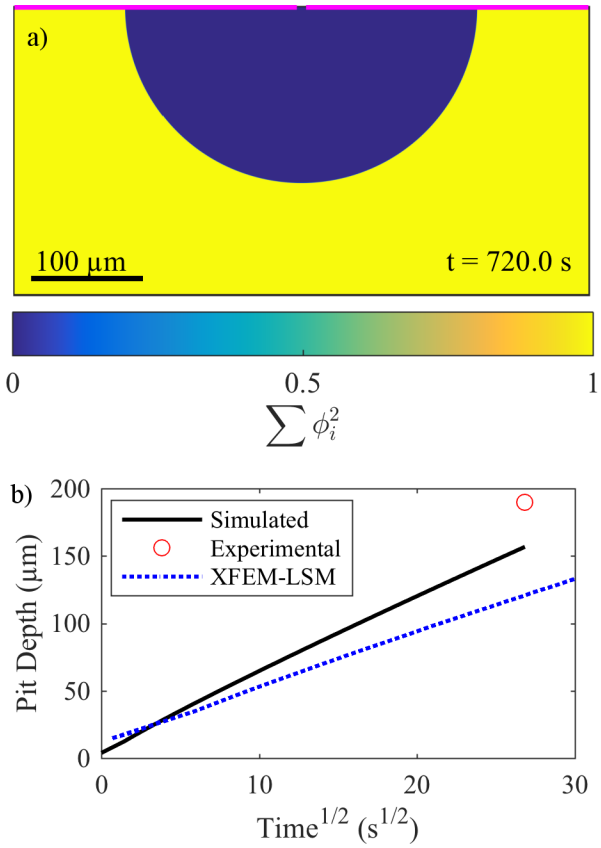

Figure 5.10. (a) The simulated pit morphology for a coated pit (coating indicated by magenta line) after 720 s at 600 mV vs. SCE, with (b) a comparison against the experimental result of Ernst and Newman[169] (red circle) and the XFEM-LSM simulation of Duddu[77] (dotted blue line) for the pit depth over the square root of time. The simulation result from Mai *et al.*[79] would directly overlap Duddu's[77] result and is omitted for clarity.

Qualitatively, the model is in general agreement with the pit morphologies observed experimentally[18,87,169,202] as well as in previous models.[75,77–81,86] These previous studies observed that pits in uncoated foils grow with a characteristically wide but shallow morphology as additional pathways form for diffusion into the bulk electrolyte.[18,75,77–80,86,87,169,202] Likewise, coated foils lead to semicircular pits where the growth is constrained due to a lack of new diffusion pathways.[18,75,77,79,80,169] However, the present work demonstrates a clear influence of IR-controlled kinetics at lower applied potentials that reduces the corrosion rate of the metal surface, which has not been extensively considered in previous modeling efforts. Additionally, the simulation results for the coated pit at 600 mV vs. SCE are in good quantitative agreement

with the experimental results of Ernst and Newman,[169] predicting a comparable pit depth over the examined time range.

The model could be modified to improve the quantitative accuracy of the results for both uncoated pit examples and the coated pit at -75 mV vs. SCE. As with the pencil electrode, the simulation geometry essentially places the reference electrode in close proximity to the metal surface, which likely does not perfect match experimental cells. Without the explicit consideration of the salt layer formation, the magnitude of the potential gradient within the pit is likely overpredicted. Additionally, experimental studies[166,203] indicate that the reaction kinetics depend on the local cation concentration, with passivation occurring on the surface where the concentration is below a critical value. The variation in the passivation of the surface directly influences the formation of the lacy cover over the pit, which the model currently neglect but has been considered in the previous modeling studies.[75–77,80,81,86] The lacy cover also affects the long-term stability of any pits that form.[52,204,205] However, the above effects should not have as strong of an impact on the coated pit at 600 mV vs. SCE. As the reaction is transport-controlled at this potential, the entire surface should be free of a passive film, although explicit consideration of salt layer formation would likely allow for further improvement in the model's agreement.

Single Pit Growth Within a Polycrystalline Microstructure

The previous simulations in this chapter demonstrate pitting corrosion without explicit consideration of microstructural features such as grains, grain orientation, or grain boundaries. These characteristics have been shown to influence local corrosion rates.[165,196,200,206] For example, previous studies of 316 stainless steel found that grain orientations with a higher atomic density exhibited lower corrosion rates than orientations with a lower atomic density.[196,206] Additionally, some alloy systems exhibit increased corrosion rates at the grain

boundaries.[165,200] Here, an example is introduced to illustrate how this modeling framework can describe the effects of polycrystalline microstructures on pit propagation during corrosion. As in the previous example, 2D simulations are considered, but now 16 ϕ_i order parameters are employed to describe individual grains within the metallic phase. A random microstructure is generated with these field variables by Voronoi tessellation without consideration of grain size distribution. Additionally, in this section, Model II is employed for the phase-field kinetics with grain coarsening in the bulk driven by the Cahn-Hilliard equation (Eqs. 5.2 and 5.7) eliminated by taking the mobility coefficient to be $M \cdot \psi$ so that motion only occurs near the metal/electrolyte interface. The boundary conditions and initial condition are the same as in the coated single crystal pitting example.

For the first part of this example, we assume isotropic, constant kinetics to examine the possible diffuse-interface artifacts of the phase-field approach in the interfacial movement when multiple interfaces are present. The evolution of this scenario is displayed in Figure 5.11. Here, the corrosion pit is initialized to be located within a single grain. Since there is a protective surface layer, the pit growth is a semicircular throughout the simulated timespan, as observed from the coated single crystal simulation results discussed above. As the pit continues to propagate, it encounters the additional grains in the microstructure and their associated boundaries. Other than a slight opening of the grain boundary at triple points with the electrolyte, the dissolution front remains much the same as in the coated single grain simulation. The triple point behavior is attributable to the underlying kinetics of the phase-field model, where there is a driving force to make all angles equal at triple points when interfacial energies are equal.[182] At the dissolution front, $M \cdot \psi$ is nonzero, and therefore evolution proceeds. However, the presence

of grain boundaries in the microstructure alone does not introduce significant artifacts in the overall time-dependent behavior of Model II.

For the second part of this example, the same polycrystalline microstructure will be considered, but now anisotropic kinetics will be introduced to the system. Each of the 16 grains is assigned a random orientation, and throughout the simulation the anisotropic kinetics is evaluated according to Eqs. 5.23-5.25. The evolution of the microstructure is then simulated under the same conditions as in the first part of the example. The results for this simulation are presented in Figure 5.12 for the same elapsed times as Figure 5.11. Whereas before the corrosion front generally retained its semicircular symmetry, with the anisotropic kinetics it is observed that the corrosion leads to the formation of mostly flat, sharply defined facets. The effect of the anisotropy is pronounced, such that by the first snapshot there remains little evidence of the semicircular initial condition. At $t = 60$ s, there is an observable artifact in the upper left region of the microstructure where the electrolyte somewhat infiltrates the metal, leading to $\sum_{i=1}^{N} \phi_i^2 < 1$ several gridpoints away from the interface. This artifact is likely due to a rapidly changing inward normal vector along the metal/electrolyte interface, which leads to a correspondingly sharp change in the mobility near the corner of the grains that are exposed to the electrolyte. Due to the rapid change in the current and mobility, the Peclet number may also be deviating away from unity, causing local changes in the characteristic behavior of the Cahn-Hilliard equation (Eqs. 5.2 and 5.7). Overall, the result in Figure 5.12 is in direct qualitative agreement with experimental results from Lindell and Pettersson,[196] who observed the formation of such faceted pits. This is in contrast to the model of Mai *et al.*,[79] which did not predict faceting. The difference may lay in the treatment of anisotropic corrosion kinetics by Mai *et al.*,[79] which was implemented by a modification of the isotropic corrosion current density of each grain.

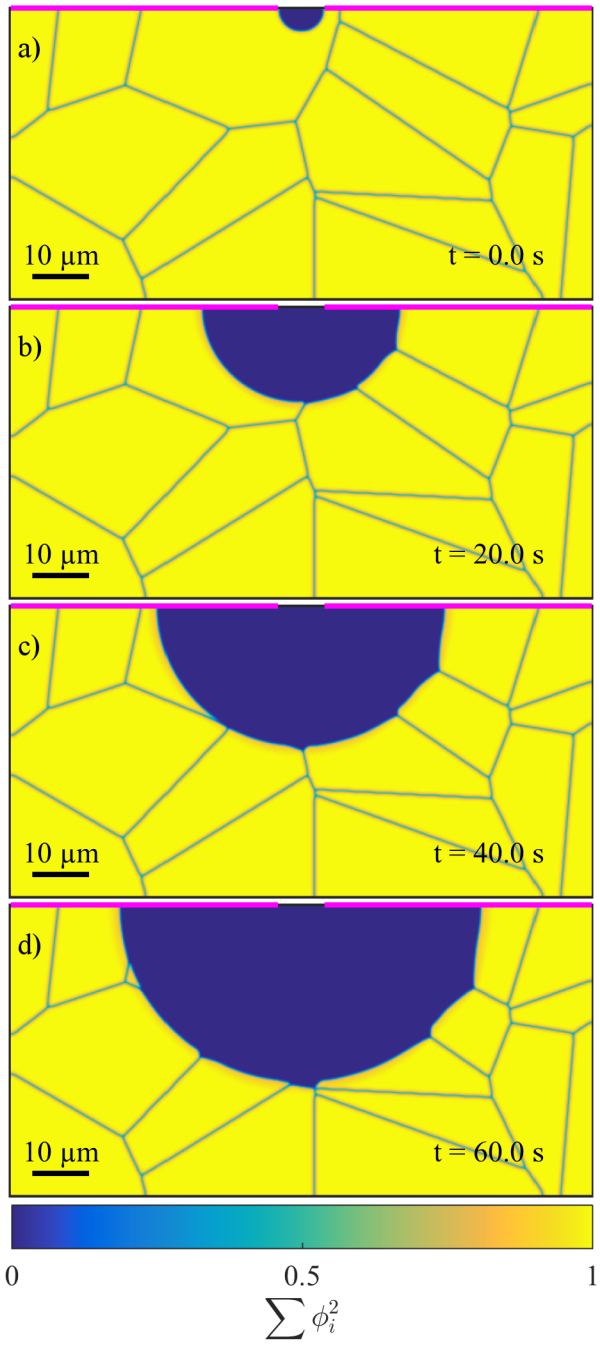

Figure 5.11. Simulated pit morphology evolution within a polycrystalline microstructure with isotropic reaction kinetics at (a) 0, (b) 20, (c) 40, and (d) 60 s with an applied potential of -75 mV vs. SCE and a protective lacquer covering the surface (magenta line).

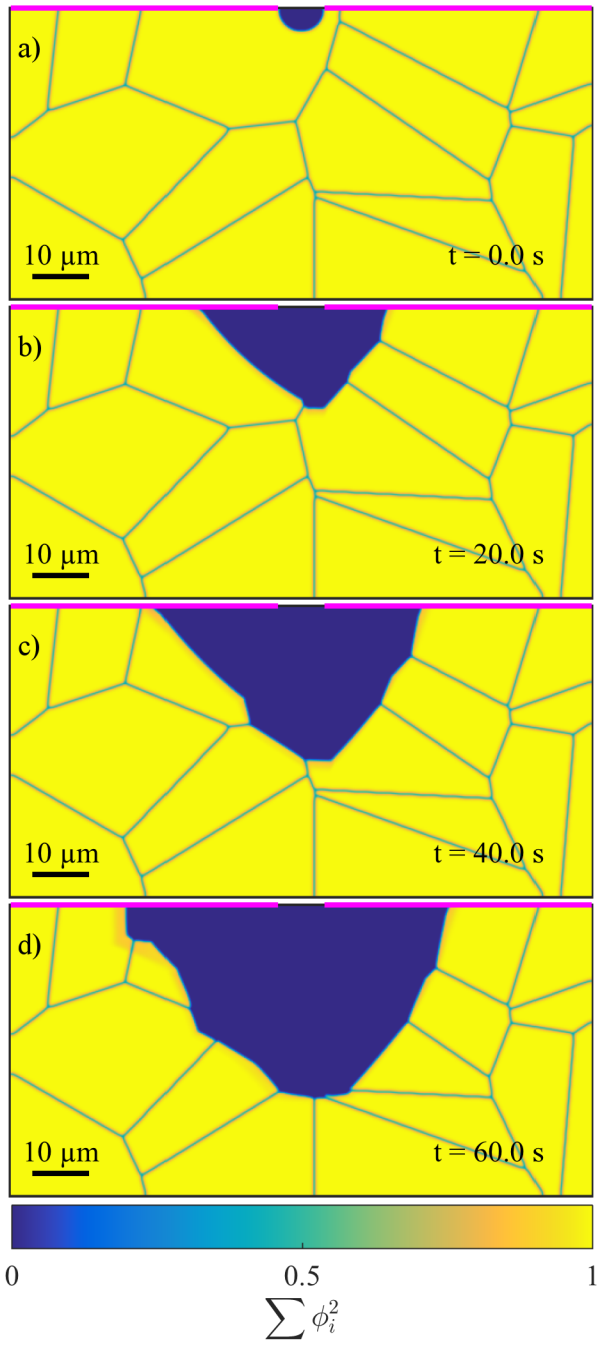

Figure 5.12. Simulated pit morphology evolution within a randomly oriented polycrystalline microstructure with orientation-dependent reaction kinetics at (a) 0, (b) 20, (c) 40, and (d) 60 s with an applied potential of -75 mV vs. SCE and a protective lacquer covering the surface (magenta line). Unlike in Figure 5.11, faceting of the grains is observed.

Single Pit Growth With Secondary Phases

The previous case focused on the presence of a polycrystalline microstructure during corrosion. However, the localized corrosion rate also depends significantly on the composition of the constituent solid that can vary due to the presence of solute depleted zones, grain boundary segregation, and precipitate particles.[17,165] The majority of existing models tend to neglect these effects for simplicity. As a final example to explicitly address these factors, the present model is applied to the corrosion of an arbitrary alloy with secondary phases (e.g., intermetallic precipitates). It should be noted that this example is intended to demonstrate the modeling framework's capability to handle such microstructures, and the example is not meant to represent any specific material. To demonstrate this scenario, 2D simulations are performed using two ϕ_i order parameters to describe a bicrystal matrix with an initial corrosion pit located on the grain boundary. Furthermore, an additional ϕ_i order parameter is used to describe a pair of precipitate particles located along the boundary below the corrosion pit. As in the previous example, Model II is employed to describe the phase-field kinetics of the polycrystalline system.

In general, the secondary phase particles would likely have kinetic properties or involve reaction species that differ from the matrix phase (see Eqs. 5.10 through 5.19). However, for simplicity, in this example all input parameters are taken to be the same as in Table 5.1 except for the corrosion current density, i_{corr}, which is assumed to be the dominant factor controlling corrosion. Within the matrix phase, i_{corr} is taken to be 9.90×10^{-4} A/cm^2 (equal to the value in Table 5.1), while it is taken to be 9.90×10^{-3} A/cm^2 (ten times faster than the value in Table 5.1) for the secondary phase particles. This corresponds to a secondary phase that is more susceptible to corrosion relative to the matrix phase. For this example, the applied potential is -

75 mV vs. SCE, and the remaining boundary conditions are the same as for the polycrystalline case, including the presence of an inert coating on the surface.

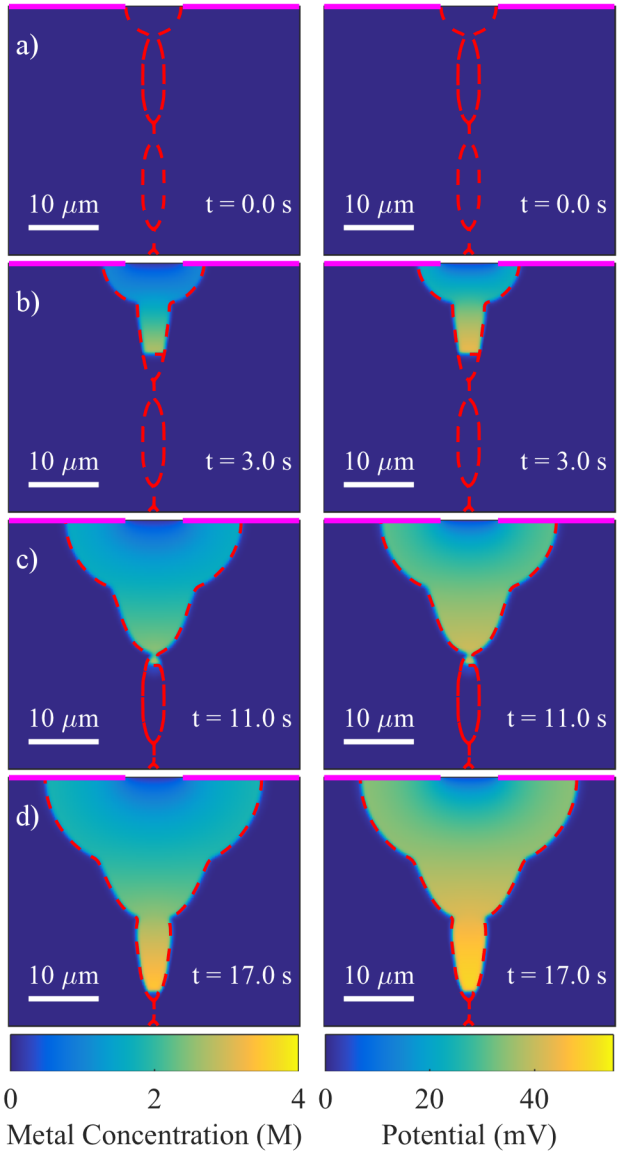

Figure 5.13. Simulated pit morphology evolution for a microstructure with precipitates located along a grain boundary, showing the (left) dissolved metal concentration and (right) electrostatic potential at (a) 0, (b) 3, (c) 11, and (d) 17 s with a -75 mV vs. SCE applied potential and an inert layer covering the surface (indicated by a magenta line). The dotted red line indicates the exact location of the interfaces as given by $\phi_i = 0.5$.

The simulation results for this example are presented in Figure 5.13. Initially, the pit grows uniformly, and because it is uncoated, new diffusion pathways can form. As the pit propagates, it eventually encounters the secondary phase particles. The first particle rapidly

dissolves, as expected, because its corrosion current density is ten times larger than that of the matrix phase. As observed in both the 1D and single-crystal simulations, the quick increase in concentration at the interface leads to a decreased overpotential that slows the corrosion reaction due to IR-controlled kinetics. Once the first particle dissolves, a deeper and narrow pit is created within the matrix phase.

When the corrosion front reaches the second particle, the corrosion rates vary throughout the pit. Towards the top, it can be observed that the pit opening is widening, suggesting that the cusp between the original pit and the first particle will eventually disappear. As in the coated single crystal, the transport pathway toward the bottom becomes more restricted and the ions must diffuse through a narrow opening into the electrolyte where the first particle dissolved. This constrained transport leads to a higher metal ion concentration and electrostatic potential at the surface where the second particle is corroding. The increased electrostatic potential in turn decreases the overpotential in Eq. 5.18, leading to stronger IR-controlled kinetics that cause the second particle to dissolve more slowly. This is confirmed in Figure 5.14, where it is observed that when the corrosion front encounters the first particle, there is a sharp increase in the velocity of the center of the pit. After the first particle dissolves, the pit growth rate returns to a slower value and more of the crystal matrix is removed. Upon encountering the second particle, the pit growth rate increases again. However, the second particle has a reduced interfacial velocity and takes longer to dissolve than the first particle.

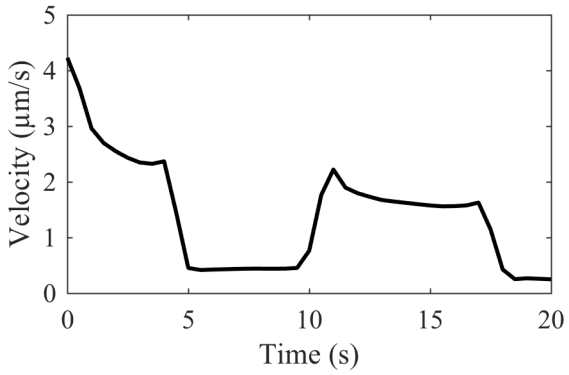

Figure 5.14. The velocity of the center of the corrosion pit as a function of time. Upon encountering the precipitate particles, the velocity of the interface increases sharply until the first particle dissolves. The second particle corrodes more slowly than the first due to a longer, more restricted diffusion pathway and an accompanying lower overpotential.

Note that the initial geometry used in this example is only one of many microstructures that can be investigated with this model. Other constructions can include particles within the matrix phase away from grain boundaries and particles with varying shape, size, and distribution. Therefore, this modeling approach enables the explicit study of secondary phases and their influences on corrosion rates and pit morphology evolution in alloys, provided that the electrochemical properties of the constituent phases are properly characterized.

Summary and Conclusions

A general modeling framework was presented for simulating localized corrosion in metallic materials. This model utilized the smoothed boundary method to couple mass transport processes and electrochemical kinetics within the electrolyte to a phase-field model describing evolution of the metallic phases and their interfaces in a straightforward manner. A microscopic expression was derived for the diffuse-interface formulation to allow simulation of activation-, IR-, and transport-controlled reaction kinetics. Two alternative approaches for describing the phase-field model were presented: a coupled Cahn-Hilliard/equilibrium Allen-Cahn approach and an all-Cahn-Hillard approach, each with variable mobility. The former was found to have better

computational performance but was unsuitable for polycrystalline systems due to an artifact, while the latter captured the behavior of a polycrystalline metal accurately. The combination of the phase-field model with the smoothed boundary method allowed for straightforward coupling of the reaction kinetics along the moving boundary with the ionic concentrations and the electrostatic potential. This permitted the inclusion of varying overpotentials and reaction rates along the metal/electrolyte interface.

Simulations with one-dimensional wire and two-dimensional foil electrodes were performed to validate the model behavior for 304 stainless steel in 1M NaCl, which showed good agreement with the experimental results of Ernst and Newman.[169] As in the models of Mai *et al.*[79] and Chen and Bobaru,[78] the transition between activation-controlled kinetics at low applied potentials to a transport-controlled regime at higher applied potentials occurred smoothly. In contrast to these previous models, the presented work explicitly included the electrostatic potential and its effects on ionic transport, allowing for the direct consideration of IR-controlled kinetics without coarse-grained approximations. The simulations demonstrated that the potential gradient has a significant effect on the limiting reaction kinetics. However, as has been previously indicated,[86,87,131,202] accurate quantification of this effect requires detailed knowledge of the cell geometry and surface morphology. Additionally, accuracy could be improved by directly considering the precipitation of a salt layer as well as the formation of a lacy pit cover. Further simulations were performed to demonstrate the model's capability by considering the effects of spatially varying and/or anisotropic reaction kinetics in synthetic polycrystalline microstructures. Overall, the model presented is suitable for simulating the morphological evolution associated with corrosion while taking into account the effects of grain orientation and

different electrochemical properties of phases in polycrystalline and/or multiphase metallic alloys.

Chapter 6.

Preliminary Work: Reduced-Order Modeling of Lithium Symmetric Cells

Introduction

In this chapter,[*] we present preliminary work for a reduced-order version of the morphology-aware 1D model as implemented in Chapter 3 and Chapter 4. As demonstrated, the framework is an effective tool that leverages coarse-grained descriptions of the anode surface morphology in order to quickly and efficiently simulate the time-dependent behavior of the system. However, while the model has provided mechanistic insight into the behavior of both magnesium and lithium metal deposition and dissolution, there are areas where the model could potentially be simplified to further reduce the computational cost. Particular optimizations will be examined specifically for the application of the model to lithium symmetric cells.

Within the full model as described in Chapter 4, one of the largest computational costs is associated with solving for the electrolyte species concentrations and the electrostatic potential in the electrolyte. Additionally, there is a significant cost to refine the computational domain due to the moving electrolyte boundary. As such, the ability to simplify the description of electrolyte transport within a moving domain would permit significant computational savings, provided that the model still accurately represented the parametric behavior of the system. In the simulation results of Chapter 4,[14] we observed that the overall potential drop in the electrolyte was small in

[*]Derived from the manuscript currently in preparation: V.W.L. Chan, A.F. Chadwick, and K. Thornton, "Parametrically-Informed Reduced-Order Model of Lithium Deposition and Dissolution in Symmetric Cells," *in preparation.*

comparison to the overpotentials associated with the reactions at each electrode (*cf.* Figure 4.10). Additionally, this potential drop was relatively constant throughout the course of cycling. These results imply that the transport in the electrolyte can be described as an average set of behaviors in the cell, and the model can therefore be further simplified.

Governing Equations

We assume that the concentration of lithium will be uniform across the cell because of the observed behavior that the potential drop across the cell does not appreciably change during a half-cycle despite changes in the concentration profile. Therefore, instead of solving the complete PNP system of equations, the time-dependent behavior of the potential drop across the electrolyte, $\Delta V_{IR}(t)$, can be described by Ohm's law:

$$\Delta V_{IR}(t) = i\frac{L(t)}{\kappa(t)}, \tag{6.1}$$

where i is the current density through the cell, $\kappa(t)$ is the average electrolyte conductivity and $L(t)$ is the time-dependent electrode separation. The conductivity is related to the bulk concentration of the electroactive species by[35]

$$\kappa(t) = \frac{F^2}{RT}\sum_i z_i^2 D_i \bar{c}_i(t), \tag{6.2}$$

where F is Faraday's constant, R is the ideal gas constant, T is the absolute temperature, z_i is the charge of the i-th electrolyte species, D_i is its diffusivity, which may or may not be dependent on concentration, and $\bar{c}_i(t)$ is its bulk concentration. The electrode separation can be calculated by integrating the magnitude of the current over time:

$$L(t) = L_0 + \left(\frac{1}{CE} - 1\right)\frac{\Omega_{Li}}{F}\int_0^t |i|\, dt, \tag{6.3}$$

where L_0 is the initial separation, Ω_{Li} is the molar volume of lithium metal, and CE is the Coulombic efficiency of the system. We assume that the growth of any morphological features such as dendrites does not significantly affect the effective electrode separation.

To describe the concentration of lithium in the electrolyte, we will examine two different sets of approximations. The first set assumes, as implied by the Coulombic efficiency model in Chapter 4, that the total number of ions produced from the lithium salt remains constant throughout cycling and that there is an essentially infinite supply of solvent. The bulk concentrations of each species in the electrolyte can then be obtained by

$$\bar{c}_i(t) = \frac{L_0}{L(t)} \bar{c}_{i,0}, \tag{6.4}$$

where $\bar{c}_{i,0}$ is the initial bulk concentration of a given species. The second set of approximations assumes that there is either an effectively infinite volume of electrolyte or that the total charge deposited on or dissolved from the electrode surface is small. The bulk concentrations of each electrolyte species can then be assumed to remain constant:

$$\bar{c}_i(t) = \bar{c}_{i,0}. \tag{6.5}$$

Both assumptions would likely fail once a significant amount of electrolyte decomposition has occurred or when the total volume of electrolyte is small. In both of these regimes, the volume of the electrolyte, and by extension the concentration of the electrolyte species, would need to be calculated from the total amount of each species and their partial molar volumes.

The overpotentials at the electrodes are calculated from the modified Butler-Volmer equation presented in Chapter 4,[14] but now the concentrations at the electrode surface are replaced with uniform concentrations:

$$i = \gamma F k_{\text{eff}}^0 \left[c_{Li} \exp\left(\frac{(1-\beta)F}{RT} \eta \right) - \bar{c}_{Li^+}(t) \exp\left(-\frac{\beta F}{RT} \eta \right) \right], \tag{6.6}$$

where γ is the relative increase in electrode surface area, $k_{\text{eff}}^0 = \theta_{\text{fast}} k_{\text{fast}}^0 + (1 - \theta_{\text{fast}}) k_{\text{slow}}^0$ is the effective rate constant as a function of the relative fraction of the electrode surface area with fast kinetics, θ_{fast}, c_{Li} is the concentration of lithium metal, and η is the overpotential. The implementation of the surface model that defines γ and θ_{fast} is the same as described by Eqs. 4.9-4.14. The total cell voltage can be calculated by summing the potential drop across the electrolyte and the overpotential at each electrode:

$$V_{cell}(t) = \eta_{Left}(t) + \Delta V_{IR}(t) + \eta_{Right}(t). \tag{6.7}$$

Unlike the full model, which is represented by a system of coupled partial differential equations, with the reduced-order approach we have simplified the model to contain only a single ordinary differential equation, Eq. 6.3. For a given value of L_0, CE, and i, Eq. 6.3 can be solved over the desired simulation time range, and the remaining quantities can be calculated based on this solution. As such, a significant computational savings can be realized over the full model, which could be further exploited when combined with a more efficient method to parameterize the model, such as Latin hypercube sampling[207] or the Levenberg-Marquardt algorithm.[208,209] This would have multiple benefits. First, the reduced cost could allow for end-users to quickly determine an initial estimate of the model parameters, the values of which could then be refined with the full model. Second, a computationally inexpensive model could enable real-time feedback between simulation and experiment or, when combined with models of cathode materials, serve as a diagnostic algorithm for monitoring the health of metal-anode batteries in EV battery packs.

Preliminary Results

To demonstrate the model, two simulations are performed for the full model, the reduced-order model with variable concentration, and the reduced-order model with constant

concentration, for a total of six simulations. The two simulations for each model employ identical model parameters as in Table 4.2 of Chapter 4 except for the following. For the first simulation, we ignore the effect of the rest in between half-cycles. The second simulation considers two full cycles using a time step of 10^{-1} s (ten times larger than the time step used in Chapter 4) to examine a parameter set that may be employed in initial coarse-time-resolution simulations of the system. For performance comparison purposes, the reduced-order model is implemented as a separate subroutine within the same overall Fortran 2008 framework as the full model. Selecting either the full or reduced-order models is accomplished by changing a single flag within the model input file that, after performing the same initialization for each model, launches the subroutine(s) for the selected model. All simulations are performed on a 2017 MacBook Pro with a 2.3 GHz Intel Core i5 processor running version 8.1.0 of the GNU Compiler Collection (GCC).

The performance results, including the run time for the full and reduced-order models and the relative speedup, are presented in Table 6.1. The assumption of constant or variable concentration in the reduced-order model did not significantly affect the run time; thus, Table 6.1 only includes the result for the model when assuming variable concentration. All of the reported run times are obtained from the best of three runs of the respective models; the worst runs were at most about a second slower. The speedup was calculated as $S = t_{\text{full}}/t_{\text{reduced}}$, where S is the speedup, t_{full} is the run time of the full model, and t_{reduced} is the run time of the reduced-order model. A large improvement in run time is realized with the reduced-order model over the full model, with a speedup of 7.6 and 70.9 for the coarser and finer simulations, respectively. The insensitivity of the reduced-order model to the simulation time step size is likely due to the significantly reduced computational complexity of the model. The reduced-order model does not

require any linear algebra computations, unlike the full model. Additionally, the amount of memory required by the reduced-order model may be small enough to fit in the cache of the processor. The largest remaining expense in the reduced-order model is the calculation of the lookup table for the electrode morphology, which does not depend on the time step size.

Table 6.1. The test matrix of system size, time step size, and number of simulated charge/discharge cycles, along with the performance comparisons between the full and reduced-order models.

System Size (μm)	Δt (s)	n_{cyc}	Full Model	Reduced Model	Speedup
750	10^{-1}	2	15.9 s	2.1 s	7.6
750	10^{-2}	5	205.5 s	2.9 s	70.9

While the reduced-order model offers a dramatic improvement in performance, it is only worthwhile to employ the model if it yields similar simulation results as the full model. Figure 6.1 plots the overall cell potential, η_{Left}, η_{Right}, and ΔV_{IR} as a function of time for the 750 μm initial electrode separation. We observe that the overall agreement between the full model and the reduced-order model both with and without constant concentration is excellent. There is a slight discrepancy amongst the models during deposition (half-cycles with peak values of η at the end of the half-cycle) and in the potential drop, which combined cause the reduced-order model to somewhat under-predict the overall polarization as compared to the full model, typically by 15-20 mV. These quantities depend upon the concentration gradient across the cell, which we know is non-negligible at this larger electrode separation from Figure 4.7. However, within the assumed model conditions the reduced order model produces nearly identical results regardless of whether the concentration is held constant, with the total polarization decreasing by a maximum of 1 mV when the concentration is constant.

Summary

In this chapter, we presented a reduced-order version of the morphology-aware voltammetry model described in Chapter 3 and Chapter 4. This reduced-order model neglects the variation in the electrolyte species' concentrations across the simulated cell, and by extension also neglects any spatial variation in properties that depend upon the concentrations. The simplification of the concentration profiles allows the model to solve Ohm's law instead of the PNP equations employed in the full model. Preliminary examinations were performed to understand the relative accuracy and computational performance of the reduced-order model. Overall, the results presented in this chapter indicate that assuming a homogenous concentration profile across a planar cell geometry is an effective way to dramatically reduce the computational cost of the 1D modeling framework. Despite this seemingly drastic simplification of the model physics, overall agreement between the full and reduced-order models remains excellent. While some discrepancies are present, these may well be within the statistical uncertainty resulting from the variations in the experimental systems and measurements with which the parameters are fitted; further examination of the models will determine whether this is indeed the case. Additionally, the differences in the simulation results were negligible when the average concentration was held constant instead of being allowed to vary as in Chapter 4. However, further analysis is needed to determine when the model and its approximations can be applied without a loss of accuracy. Overall, these preliminary results appear to confirm that the morphological evolution, which is incorporated in the morphology-aware Butler-Volmer kinetic model, is the dominant contribution to the overall cell polarization, and that concentration gradients play a comparatively minor role.

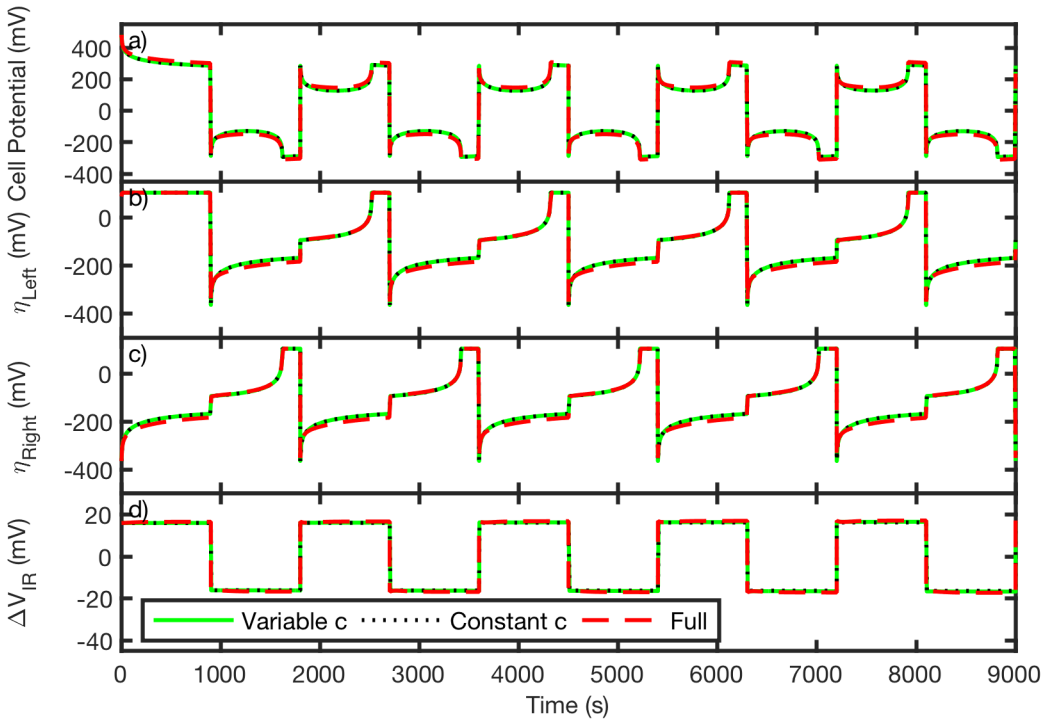

Figure 6.1. The simulated curves for (a) the total cell polarization, (b) the overpotential of the left electrode, (c) the overpotential of the right electrode, and (d) the potential drop in the electrolyte as a function of time for an initial electrode separation of 750 μm. Each plot contains the curves for the reduced-order model with both variable concentration (solid green line) and constant concentration (dotted black line), as well as the full model (dashed red line). The largest discrepancy is visible in the electrode overpotentials during deposition half-cycles, as the concentration gradient across the cell is non-negligible. A slight deviation is also visible in the IR drop throughout each cycle.

Chapter 7.

Preliminary Work: Mechanical Interactions Between Decomposed Protection Layers and Lithium Anodes

Introduction

In this chapter,[*] we present preliminary work for a diffuse-interface model that couples the transport solver developed in Chapter 5 with a smoothed boundary formulation of linear elasticity. This model is developed to simulate the mechanical interactions between a lithium anode and a decomposed, mixed-ionic conducting protection layer. This work is still ongoing; as such, only selected results are shown.

Significant progress has been made towards developing long-life lithium metal anodes for Li-S and Li-air chemistries. However, degradation of the anode surface remains a significant barrier to the success of lithium metal batteries, whether it be the formation of dendrites on the lithium anode[14,163,210] or passivation of the anode surface.[211–214] One possible approach to extend the lifetime of the anode is to apply a protection layer that isolates the anode from the electrolyte. The protection layer can consist of a variety of materials. For example, they may be standalone polymer or ceramic membranes laminated on the anode,[215,216] ceramic layers deposited via atomic layer deposition (ALD),[148,217,218] or thin layers of alloyed metals.[219] While protection layers have shown marked improvement in the lifespan of a lithium metal anode, some solid-

[*]Derived from the manuscript currently in preparation: A.F Chadwick and K. Thornton, "Effect of Material and System Anisotropy on the Mechanical Response of Mixed Ionic Conducting Thin Films for Lithium Anode Protection," *in preparation.*

state materials such as LiPON,[220] NASICON-type ceramics,[221] $Li_7P_3S_{11}$,[222] and $Li_{10}GeP_2S_{12}$ (LGPS)[223] are unstable in contact with lithium metal. The materials mentioned above are essentially single-ion conductors (i.e., they have a lithium transference number that is near unity), and therefore transport should occur almost entirely by lithium cation migration.[224] However, some protection layer materials have less-than-unity transference numbers for lithium. For instance, graphene oxide membranes have been found to have a transference number of 0.93,[216] and spinel-type materials show evidence of concentration gradients during cycling, indicative of a transference number less than one.[225] Additionally, some solid electrolytes break down upon contact with lithium to form mixed ionic/electronic conducting interphases[223,226] in which species other than lithium can carry some portion of the current in the layer. Lastly, several examples of potential protection layer materials exhibit phase changes with varying lithium concentrations.[225,227–232] The lithium cation concentration gradient in either a pristine mixed-conducting or a decomposed region of a single-ion-conducting protection layer material would lead to eigenstrains during cycling due to the lattice-size dependence on concentration. The resulting stresses may not necessarily be large enough to cause catastrophic failure of the protection layer such as electrochemical shock as observed in cathode materials.[95] However, given the intimate contact between lithium and the protection layer, the induced eigenstrain could produce stress in the anode and at the anode-protection layer interface that may lead to degradation, such as delamination, which would alter the effectiveness of the protection layer.

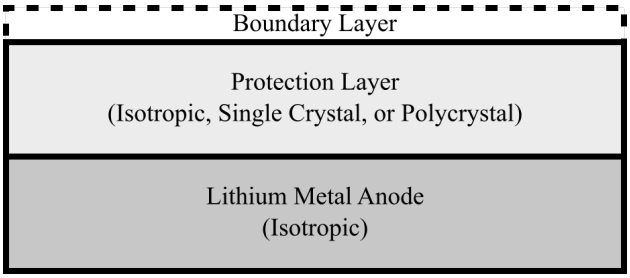

Figure 7.1. Two-dimensional schematic of the model geometry simulated in this study, consisting of the lithium metal anode, the protection layer, and a thin numerical boundary layer necessary for the traction-free boundary condition in the smoothed boundary method. The anode is assumed to be a single isotropic domain, but the protection layer's exact properties and morphology depend upon the specific example being considered.

Model Formulation

In this chapter, we consider a half-cell that consists of a lithium-metal anode and a protection layer that is directly bonded to the anode surface. We assume that the counter electrode acts as an ideal source or sink of lithium ions that enforces a constant lithium ion concentration in the undecomposed region of the protection layer, but its exact composition, geometry, and reaction kinetics are not explicitly considered. The lithium anode is assumed to have isotropic properties, while the protection layer can be either isotropic, an anisotropic single crystal, or a polycrystalline aggregate of anisotropic crystals. The anode has a thickness, L_A, and the protection layer has an overall thickness, L_{PL}. We examine a system in which a portion of the protection layer has decomposed to form a mixed-ionic conductor, with the decomposed region having a thickness L_{PL}^{D}. We also assume that the protection layer does not further decompose, i.e., the thickness of the decomposed region is static over the course of the simulation. A 2D schematic representation of the model geometry is presented in Figure 7.1. In addition to the anode and protection layer, a thin numerical boundary layer is included in the computational domain, the necessity of which is described in the Numerical Methods section.

Here, we assume that both the lithium electrode and the protection layer exhibit linear elastic behavior and that the system is in mechanical equilibrium. In the Einstein notation, mechanical equilibrium is expressed as:[233]

$$\frac{\partial \sigma_{ij}}{\partial x_j} = \frac{\partial}{\partial x_j}\left[C_{ijkl}\left(\epsilon_{kl} - \epsilon_{kl}^{\text{eig}}\right)\right] = 0, \tag{7.1}$$

where σ_{ij} is the stress tensor, x_i is the position along the i-th axis, C_{ijkl} is the stiffness tensor, $\epsilon_{ij} = \left(\partial u_i/\partial x_j + \partial u_j/\partial x_i\right)/2$ is the elastic strain tensor, $\epsilon_{ij}^{\text{eig}}$ is the eigenstrain tensor, and u_i is the displacement in the i-th direction. All indices in Eq. 7.1 range from one to three, representing three spatial coordinates. The eigenstrain arises from a tensorial form of Vegard's law[234] and can be expressed as

$$\epsilon_{ij}^{\text{eig}} = \beta_{ij}(c_+ - \bar{c}_+), \tag{7.2}$$

where β_{ij} is the chemical expansion tensor given below,[92,235,236] c_+ is the local concentration of lithium, and $\bar{c}_+$ is the constant, initial lithium concentration in the decomposed protection layer. This form of eigenstrain has been employed in models of volumetric expansion in cathode materials.[92,235,236] The chemical expansion tensor has the form:

$$\beta_{ij} = \frac{1}{c_+ - \bar{c}_+}\begin{bmatrix} \dfrac{a_1(c_+) - a_1(\bar{c}_+)}{a_1(\bar{c}_+)} & 0 & 0 \\ 0 & \dfrac{a_2(c_+) - a_2(\bar{c}_+)}{a_2(\bar{c}_+)} & 0 \\ 0 & 0 & \dfrac{a_3(c_+) - a_3(\bar{c}_+)}{a_3(\bar{c}_+)} \end{bmatrix}, \tag{7.3}$$

where a_1, a_2, and a_3 are the concentration-dependent lattice parameters of the crystal.

Once Eq. 7.1 has been solved, the stress tensor can be evaluated throughout the material, and the hydrostatic (σ_H) and von Mises (σ_{VM}) stresses may be calculated via[233]

$$\sigma_H = \frac{1}{3}(\sigma_1 + \sigma_2 + \sigma_3), \tag{7.4}$$

$$\sigma_{VM} = \frac{1}{\sqrt{2}}[(\sigma_1 - \sigma_2)^2 + (\sigma_2 - \sigma_3)^2 + (\sigma_1 - \sigma_3)^2 + 6(\sigma_4^2 + \sigma_5^2 + \sigma_6^2)]^{1/2}. \quad (7.5)$$

The hydrostatic stress describes whether a material is in tension or compression and the von Mises stress is often employed as a diagnostic of when materials may yield or fail.[233]

The transport of ionic species and the resulting current distribution are solved for within the protection layer. We assume that the protection layer material contains three relevant ionic species: lithium cations, a fixed anion, and a mobile anion, with each species having concentrations c_+, c_-^F, and c_-^M, respectively. The protection layer may have additional species that are assumed to be inert and thus are not explicitly considered in the present model. We assume that electroneutrality is enforced throughout the entire protection layer,

$$c_+ - c_-^F - c_-^M = 0, \quad (7.6)$$

where we have further assumed that the anions have a charge number of -1. To calculate the initial concentrations of the anionic species in the protection layer material, we employ the definition of the transference number of lithium,[35,37] t_+:

$$t_+ = \frac{D_+ \bar{c}_+}{D_+ \bar{c}_+ + D_-^F \bar{c}_-^F + D_-^M \bar{c}_-^M}, \quad (7.7)$$

where D_+ is the diffusivity of lithium, D_-^F is the diffusivity of the fixed anion, D_-^M is the diffusivity of the mobile anion, and the bar over each concentration refers to the initial concentration of each species in the protection layer within the decomposed region. For the fixed anion, D_-^F is zero, and thus the fixed anion is unable to carry any portion of the current. The current is thus carried by either lithium or the mobile anion, which, to simplify the analysis, we assume have equal diffusivities. Therefore, we can calculate the initial concentration of the mobile anion by

$$\bar{c}_-^M = \bar{c}_+ \frac{1 - t_+}{t_+}. \quad (7.8)$$

To ensure electroneutrality, $\bar{c}_-^F$ must therefore satisfy

$$\bar{c}_-^F = \bar{c}_+ - \bar{c}_-^M = \bar{c}_+ \frac{2t_+ - 1}{t_+}. \tag{7.9}$$

By inspection of Eqs. 7.6-7.9, we observe that, when $t_+ = 1$, $\bar{c}_-^M$ is zero. To satisfy electroneutrality throughout the protection layer, c_+ must be constant and equal to $c_-^F = \bar{c}_-^F$, which is consistent with the expected behavior of single-ion conductors.[224] We also observe that t_+ must always be greater than 0.5, as otherwise $\bar{c}_-^F$ would be negative, which is unphysical. When $0.5 < t_+ < 1$, the c_+ must always be greater than or equal to c_-^F, as in order for $c_+ < c_-^F$ to be true, c_-^M would have to be negative to satisfy electroneutrality. From the observed behavior of Eqs. 7.6-7.9, we therefore conclude that the total lithium concentration can be expressed as the sum of two effective lithium cation concentrations. The first effective concentration is a portion that counteracts the charge of the fixed anions, $\bar{c}_+^F$, which must equal $\bar{c}_-^F$. The second effective concentration is the remainder that counteracts the charge of the mobile anions, with an initial concentration $\bar{c}_+^M = \bar{c}_-^M$.

When current flows through the protection layer, there will be an induced flux of ions. The flux due to c_+^F, $\mathbf{N}_+^F$, only contains a contribution from migration due to the presence of an electric field, as c_+^F is constant:[35,37]

$$\mathbf{N}_+^F = -\frac{F}{RT} D_+ c_+^F \nabla\Phi, \tag{7.10}$$

where F is Faraday's constant, R is the ideal gas constant, T is the absolute temperature, and Φ is the electrostatic potential. On the other hand, the flux due to c_+^M, $\mathbf{N}_+^M$, contains contributions from both diffusion and migration, as c_+^M is able to vary across the protection layer. We assume that there are no interactions between the lithium cations and the mobile anions, and therefore $\mathbf{N}_+^M$ can be described by the Nernst-Planck equation:[35,37–40,44]

$$\mathbf{N}_{+}^{M} = -D_{+}\nabla c_{+}^{M} - \frac{F}{RT} D_{+} c_{+}^{M} \nabla \Phi. \tag{7.11}$$

The fixed anion is assumed to have a diffusivity of zero; therefore, its flux satisfies

$$\mathbf{N}_{-}^{F} = 0 \tag{7.12}$$

throughout the protection layer. Lastly, we assume that the flux of the mobile anion, $\mathbf{N}_{-}^{M}$, can also be described by the Nernst-Planck equation:

$$\mathbf{N}_{-}^{M} = -D_{-}^{M}\nabla c_{-}^{M} + \frac{F}{RT} D_{-}^{M} c_{-}^{M} \nabla \Phi. \tag{7.13}$$

Through our assumptions of electroneutrality and equal diffusivities among all mobile species, we can rewrite Eq. 7.13 as

$$\mathbf{N}_{-}^{M} = -D_{+}\nabla c_{+}^{M} + \frac{F}{RT} D_{+} c_{+}^{M} \nabla \Phi. \tag{7.14}$$

If there is an imbalance between its incoming and outgoing flux in any given volume, c_{+}^{M} will evolve over time according to the continuity equation,

$$\frac{\partial c_{+}^{M}}{\partial t} = -\nabla \cdot \mathbf{N}_{+}^{M}, \tag{7.15}$$

where t is time. The values of c_{+}^{F} and c_{-}^{F} are constant over time because we assume that decomposition is not ongoing in the protection layer, and the value of c_{-}^{M} can be calculated through electroneutrality; therefore only Eq. 7.15 is required to describe the evolution of the concentrations. The electrostatic potential distribution in the electrolyte is needed in order to solve for the individual fluxes. The electrostatic potential can be calculated via the current continuity equation. The current density in the protection layer is obtained from the net flux given by the sum of the fluxes described by Eqs. 7.10-7.14:

$$\mathbf{i} = F(\mathbf{N}_{+}^{F} + \mathbf{N}_{+}^{M} - \mathbf{N}_{-}^{F} - \mathbf{N}_{-}^{M}) = -\frac{F^{2}}{RT} D_{+}(c_{+}^{F} + 2c_{+}^{M})\nabla \Phi = -\kappa \nabla \Phi, \tag{7.16}$$

where $\mathbf{i}$ is the current density and κ is the local conductivity of the protection layer. If we assume that the current density is divergence-free, which follows from electroneutrality and charge conservation,[35] then the electrostatic potential is determined by

$$\nabla \cdot \mathbf{i} = -\nabla \cdot (\kappa \nabla \Phi) = 0. \tag{7.17}$$

At the protection layer/anode interface, a reaction will occur that causes ions to enter or exit the protection layer. We assume that the interface is blocking to the anionic species and only lithium will be involved in the interfacial reaction. The total flux of lithium ions at the interface is

$$\frac{i_{rxn}}{F} = \mathbf{N}_+ \cdot \mathbf{n}_{PL} = (\mathbf{N}_+^{\mathbf{F}} + \mathbf{N}_+^{\mathbf{M}}) \cdot \mathbf{n}_{PL} = -\left[D_+ \nabla c_+^M + \frac{F}{RT} D_+ (c_+^F + c_+^M) \nabla \Phi\right] \cdot \mathbf{n}_{PL}, \tag{7.18}$$

where i_{rxn} is the reaction current normal to the interface and $\mathbf{n}_{PL}$ is the inward unit normal vector at the interface with respect to the protection layer. We have assumed that c_+^F is constant; therefore, the boundary condition of Eq. 7.15 is obtained by rearranging Eq. 7.18:

$$-\frac{i_{rxn}}{F} - \left(\frac{F}{RT} D_+ c_+^F \nabla \Phi\right) \cdot \mathbf{n}_{PL} = \left(D_+ \nabla c_+^M + \frac{F}{RT} D_+ c_+^M \nabla \Phi\right) \cdot \mathbf{n}_{PL}. \tag{7.19}$$

The reaction current density, i_{rxn}, is calculated via Butler-Volmer kinetics:[35,37]

$$i_{rxn} = i_0 \left\{ \exp\left[\frac{(1-\beta)F}{RT}\eta\right] - \exp\left[-\frac{\beta F}{RT}\eta\right] \right\}, \tag{7.20}$$

where i_0 is the exchange current density and β is the charge transfer symmetry coefficient. The overpotential, η, is given by $\eta = V_a - E^{0'} - \Phi$, where V_a is the voltage applied to the lithium anode and $E^{0'}$ is the formal potential of lithium reduction. In this chapter, all simulations are performed assuming galvanostatic conditions. Therefore, the value of V_a is allowed to vary over time such that the average current density along the interface is always equal to a desired applied current density, i_{app}, and the reference potential can be chosen arbitrarily. At L_{PL}^D, we assume

that there is no discontinuity in the total lithium concentration between the pristine and decomposed regions of the protection layer. Therefore, the concentration of each species is fixed at its initial value. When solving for the electrostatic potential, the reaction current density defined by Eq. 7.20 is also the value of the current density at the protection layer/anode interface, which leads to one of the boundary conditions for Eq. 7.17:

$$\mathbf{i} \cdot \mathbf{n}_{PL} = -\kappa \nabla \Phi \cdot \mathbf{n}_{PL} = i_{rxn}. \tag{7.21}$$

At the interface between the protection layer and the boundary layer, the electrostatic potential is set such that the current density normal to that interface is equal to i_{app}.

Numerical Methods

For this study, we employ a numerical approach based on the smoothed boundary method[73] (SBM) to solve Eqs. 7.1, 7.15, and 7.17. The SBM is a diffuse-interface technique that solves the governing equations on a domain that is defined by mathematically smooth functions and that automatically enforces boundary conditions along the edge of that domain. When applied to linear elasticity, the SBM allows for a traction-free boundary condition to be applied on the diffuse interface, which in our case is the interface between the protection layer and a liquid electrolyte. Using the formalism of Yu *et al.,*[73] Eq. 7.1 may be rewritten as:

$$\frac{\partial}{\partial x_j}\left[\psi_{TF} C_{ijkl} \frac{1}{2}\left(\frac{\partial u_i}{\partial x_j} + \frac{\partial u_j}{\partial x_i}\right)\right] + |\nabla \psi_{TF}| N_i = \frac{\partial}{\partial x_j}\left[\psi_{TF} C_{ijkl} \beta_{kl} (c_+ - \bar{c}_+)\right], \tag{7.22}$$

where ψ_{TF} is a phase-field-like domain parameter, and N_i is the applied surface traction, which for a traction-free boundary is zero. The value of ψ_{TF} is one in the solid (anode and the protection layer), zero outside the solid, and smoothly transitions between from one to zero at the traction-free surface located at the protection layer/boundary layer interface in Figure 7.1 A

hyperbolic tangent function is employed to describe ψ_{TF} as a function of the vertical position, which is given by the expression:

$$\psi_{TF} = \frac{1}{2}\left[1 - \tanh\left(\frac{z - z_{TF}}{\zeta}\right)\right], \tag{7.23}$$

where z is the position along the vertical axis, z_{TF} is the location of the traction-free boundary between the protection layer and the boundary layer, and ζ is the half thickness of the diffuse interface.

In order to apply the SBM to Eqs. 7.15 and 7.17, we first define a diffuse-interface representation of the model geometry in Figure 7.1. To obtain the continuous functions that define the boundaries, we employ the phase-field method to smooth an initial voxel-based representation of the anode and protection layer, where the protection layer contains N grains. The anode and each grain are assigned to an order parameter, ϕ_i, with values of one inside the anode or corresponding grain and zero elsewhere prior to the smoothing operation based on the phase-field approach. A free energy functional is defined with these order parameters according to the polycrystalline phase-field model of Fan and Chen:[237]

$$\mathcal{F} = \int_{\Omega}\left(W f_0(\{\phi_i\}) + \frac{\epsilon^2}{2}\sum_{i=0}^{N}(\nabla\phi_i)^2\right)d\Omega, \tag{7.24a}$$

$$f_0(\{\phi_i\}) = \sum_{i=0}^{N}\left(\frac{{\phi_i}^4}{4} - \frac{{\phi_i}^2}{2}\right) + \gamma\sum_{i=0}^{N}\sum_{j>i}^{N}{\phi_i}^2{\phi_j}^2. \tag{7.24b}$$

Here, W is the well height of the free energy, ϵ is the gradient energy coefficient associated with an energy penalty for large gradients, and γ is a parameter that controls the barrier in the free energy for overlapping interfaces. In Eq. 7.24, ϕ_0 corresponds to the lithium anode and ϕ_i for $1 \leq i \leq N$ corresponds to the individual grains of the protection layer. This initial microstructure is smoothed with the Allen-Cahn equation:[74]

$$\frac{\partial \phi_i}{\partial t} = -L\frac{\delta \mathcal{F}}{\delta \phi_i}, \tag{7.25a}$$

$$\frac{\delta \mathcal{F}}{\delta \phi_i} = W\left(\phi_i^3 - \phi_i + 2\gamma\phi_i\sum_{j\neq i}^{N}\phi_j^2\right) - \epsilon^2\nabla^2\phi_i, \tag{7.25b}$$

where L is the Allen-Cahn mobility coefficient. The microstructure is smoothed until all of the interfacial thicknesses are approximately equal to 2ζ.

To solve Eqs. 7.15 and 7.17 via the SBM, we define a domain parameter corresponding to the protection layer, ψ_{PL}, as

$$\psi_{PL} = 1 - \phi_0. \tag{7.26}$$

Equations 7.15 and 7.17 can now be reformulated by the SBM. The SBM form of Eq. 7.15 is

$$\frac{\partial c_+^M}{\partial t} = \frac{D_+}{\psi_{PL}}\nabla\cdot\left(\psi_{PL}\left[\nabla c_+^M + \frac{F}{RT}c_+^M\nabla\Phi\right]\right) + \frac{|\nabla\psi_{PL}|}{\psi_{PL}}\left[\frac{i_{rxn}}{F} + \left(\frac{F}{RT}D_+\bar{c}_+^S\nabla\Phi\right)\cdot\mathbf{n}_{PL}\right], \tag{7.27}$$

and the SBM form of Eq. 7.17 is

$$\nabla\cdot(\psi_{PL}\psi_{TF}\kappa\nabla\Phi) = |\nabla\psi_{PL}|i_{rxn} - |\nabla\psi_{TF}|i_{app}. \tag{7.28}$$

For the slab geometry in Figure 7.1, Eq. 7.28 may also be written as

$$\begin{aligned} H_{BC}\nabla\cdot(\psi_{PL}\kappa\nabla\Phi) + (1-H_{BC})\nabla\cdot(\psi_{TF}\kappa\nabla\Phi) \\ = H_{BC}|\nabla\psi_{PL}|i_{rxn} - (1-H_{BC})|\nabla\psi_{TF}|i_{app}, \end{aligned} \tag{7.29}$$

where H_{BC} is a Heaviside function with a value of one near the anode that sharply switches to zero halfway across the protection layer towards the traction-free surface. Equation 7.29 is employed for the simulations presented in this chapter. The value of $\mathbf{n}_{PL}$ in Eq. 7.27 is calculated from the order parameter by:

$$\mathbf{n}_{PL} = \nabla\psi_{PL}/|\nabla\psi_{PL}|. \tag{7.30}$$

The overall governing equations, Eqs. 7.22, 7.27, and 7.29, are solved using the Fortran-2008-based SBM framework developed in Chapter using the finite difference method. All spatial

derivatives are discretized with second-order centered differences, and Eq. 7.27 is solved until the steady state is achieved using an implicit pseudo time-stepping scheme. The resulting system of equations is solved using point-wise SOR[198] with a red-black ordering scheme that allows for vectorized execution of the relaxation.

Model Parameters

The kinetic, transport, and mechanical parameters employed in this preliminary study are summarized in Table 7.1. All components of the stiffness tensor are calculated from the Young's modulus, E, Poisson's ratio, ν, and the Zener anisotropy, A_z,[238] using the Voigt-Reuss-Hill (VRH) formalism.[239] We restrict the present model to only consider either isotropic are cubic materials, which in the material coordinate system only have nonzero values of $C_{11} = C_{22} = C_{33}$, $C_{12} = C_{13} = C_{23}$, and $C_{44} = C_{55} = C_{66}$. With the VRH formalism, the values of the elastic constants are:

$$C_{11} = \frac{E(11 + 13A_z + A_z^2 - 19\nu - 7A_z\nu + A_z^2\nu)}{(3 + 19A_z + 3A_z^2)(1 - \nu - 2\nu^2)}, \tag{7.31}$$

$$C_{12} = \frac{E(-4 + 3A_z + A_z^2 + 11\nu + 13A_z\nu + A_z^2\nu)}{(3 + 19A_z + 3A_z^2)(1 - \nu - 2\nu^2)}, \tag{7.32}$$

$$C_{44} = \frac{1}{2}A_z(C_{11} - C_{12}). \tag{7.33}$$

The elastic constants are set locally as a function of position and crystallographic orientation:

$$C_{ijkl} = \sum_{m=0}^{N} \phi_m C_{ijkl}^m(\theta_1^m, \Theta^m, \theta_2^m), \tag{7.34}$$

$$\beta_{ij} = \sum_{m=0}^{N} \phi_m \beta_{ij}^m(\theta_1^m, \Theta^m, \theta_2^m), \tag{7.35}$$

The crystallographic orientations are represented by a set of rotations described with extrinsic z-x-z Euler angles,[240] where a given grain is first rotated by angle θ_1 around the z axis, then by angle Θ around the x axis, and finally by θ_2 around the z axis. In the unrotated case, it is assumed that the [100] axis is parallel with the x axis, the [010] axis is parallel with the y axis, and the [001] axis is parallel with the z axis and the direction of the current.

Table 7.1. The values of the material properties and operating conditions of the protection layer/anode half-cell examined in this preliminary study. All of the protection layer properties are chosen to be comparable to typical protection layer materials but are not meant to represent a specific material. The lithium mechanical properties are taken from a literature DFT study.[24]

Parameter	Description	Default Value	Source
i_{app}	Average applied current density	-1 mA/cm^2	
i_0	Exchange current density	1 mA/cm^2	
β	Charge transfer symmetry coefficient	0.5	
$E^{0'}$	Formal potential	0 V vs. Li/Li$^+$	
$\bar{c}_+$	Initial lithium concentration	10 M	
t_+	Li$^+$ transference number	0.9	
D_+	Li$^+$ diffusivity	10^{-8} cm^2/s	
L_{PL}	Protection layer thickness	6.4 µm	
L_{Li}	Lithium anode thickness	6.4 µm	
E_{PL}	Protection layer Young's modulus	100 GPa	
ν_{PL}	Protection layer Poisson ratio	0.34	
$\beta_{11} = \beta_{22} = \beta_{33}$	Chemical expansion coefficient	1 cm^3/mol	
E_{Li}	Lithium metal Young's modulus	13 GPa	24
ν_{Li}	Lithium metal Poisson ratio	0.34	24

Preliminary Results

The model is first validated against the analytical solution described by Eqs. B.4 and B.11 in Appendix B. For these validation simulations, a thin 3D geometry is employed with a resolution of 128 × 16 × 144 in the x, y, and z directions, respectively. Of the 144 grid points in the z direction, 16 are used to represent the thickness of the numerical boundary layer required for the SBM mechanical equilibrium model. For the results presented here, we assumed that the entire thickness of the protection layer had decomposed, i.e., $L_{PL}^{D} = L_{PL}$. Initial simulations indicated that, for a constant value of L_{PL}^{D}, increasing L_{PL} negligibly affected the stress distributions. Two trends are examined for the validation: the peak hydrostatic stress in the protection layer as a function of the lithium transference number in an isotropic material (i.e., $A_z = 1$), and the peak hydrostatic stress as a function of crystallographic orientation in a cubic material with $A_z = 2$.

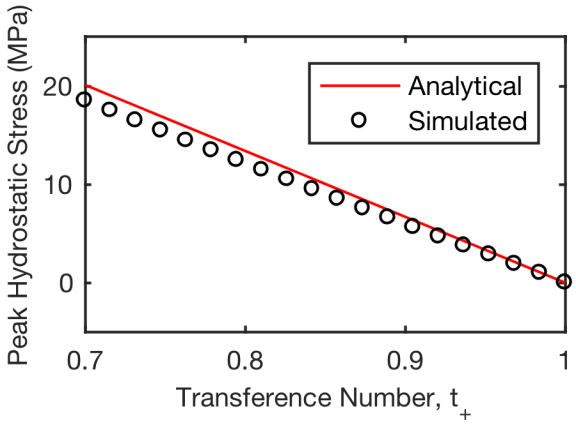

Figure 7.2. The comparison between the analytical model in Appendix B and the numerical model presented in this chapter for the trend in the peak hydrostatic stress in the protection layer as a function of the lithium transference number in an isotropic material.

To examine the effect of the transference number, t_+ is varied between 0.7 and 1 for an isotropic protection layer. The resulting trends for the numerical and analytical models are presented in Figure 7.2. We observe that the overall agreement between both models is generally good. Both models correctly predict that there should be no concentration-induced stress when $t_+ = 1$, as should be the case for single-ion conducting materials. The analytical model slightly

overpredicts the peak stress at smaller transference numbers, which is due to the assumption of a constant potential gradient across the protection layer in the analytical model. As the transference number is decreased, the potential gradient increasingly varies across the protection layer in the simulations. If we were to relax the assumption of a constant gradient in the analytical model, the agreement would be improved.

To examine the effect of the crystallographic orientation, we consider a single crystal with cubic anisotropy and $t_+ = 0.9$ (as in Table 7.1). The crystallographic orientation is rotated away from its initial orientation, with each Euler angle in Eqs. 7.33 and 7.34 having an identical value between 0 and π radians. The resulting trend for the peak hydrostatic stress as a function of this rotation is present in Figure 7.3. Here, we observe that the numerical and analytical models are in excellent agreement. The results indicate that the presence of anisotropy in the crystal structure leads to crystallographic orientations that experience higher levels of stress than others. Combined, the results in Figure 7.2 and Figure 7.3 demonstrate that the numerical model accurately represents the mechanical response of the mixed-conducting protection layer.

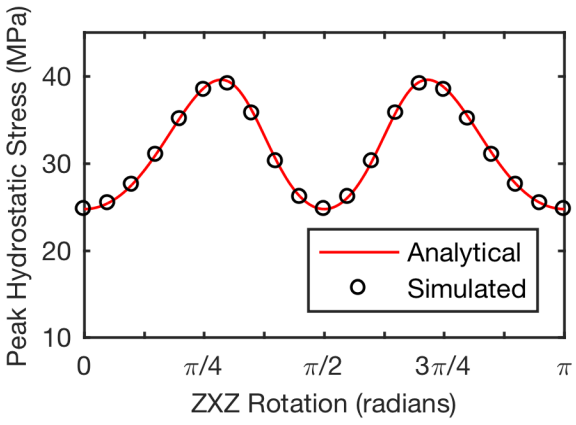

Figure 7.3. The comparison between the analytical model in Appendix B and the numerical model presented in this chapter for the trend of the peak hydrostatic stress in the protection layer as a function of the crystallographic orientation of a cubic material with $A_z = 2$ and $t_+ = 0.9$.

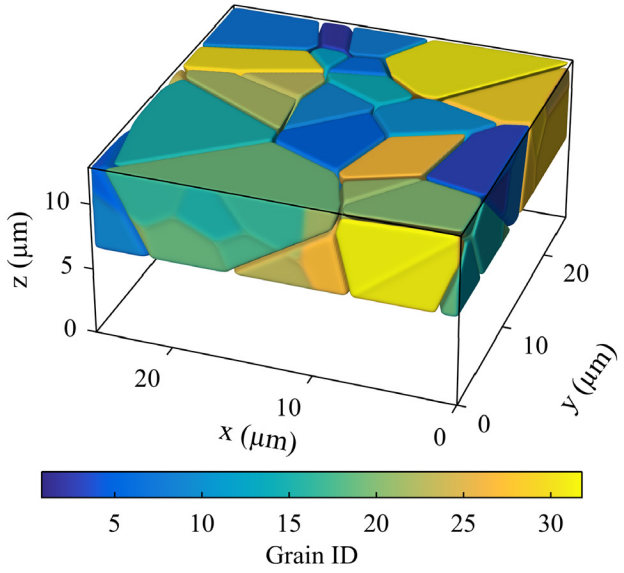

Figure 7.4. The synthetic microstructure of the anode/protection layer half-cell considered in the preliminary study. The numerical boundary layer on top of the protection layer and the lithium anode have been removed to clearly show the protection layer.

Next, the model is employed to simulate the stress distribution in an anode and a polycrystalline protection layer with 32 randomly oriented cubic grains with $A_z = 3.52$. This simulation is performed with a resolution of 256 × 256 × 144. The initial crystal structure, shown in Figure 7.4 with the boundary layer and lithium anode removed, was generated via Voronoi tessellation and then smoothed using the Allen-Cahn dynamics described earlier.

The results for the simulation are presented in Figure 7.5, including the concentration profile in the protection layer, the hydrostatic and von Mises stresses in the protection layer, and the von Mises stress in the lithium anode. We observe that, due to the random orientation of the grains in the protection layer, there is a wide variation in the stress distributions of the protection layer. Due to the anisotropy of the mechanical response, the protection layer induces stress in the lithium anode. Regions near grain boundaries in the protection layer tend to experience increased levels of stress. Additionally, much of the anode that is near the grain boundaries is at or above the yield stress of lithium, which is about 560 kPa.[241] Thus, in a time-dependent simulation we

would expect the lithium to plastically deform and the distribution in stress would lead to variations in the local deposition rate across the anode surface.[242]

While plastic deformation is beyond the scope of the present model's capability, we can examine the pseudo-steady-state displacement of the anode surface. A quiver plot of the displacement field along the lithium anode isosurface is plotted in Figure 7.6. The length of each quiver is 50,000 times the magnitude of the displacement vector. Although the resulting displacements are on the order of a few angstroms, we observe that some regions of the lithium anode are pulled into the protection layer while others are compressed towards the base of the anode. In some areas of the anode this change in displacement direction occurs over short distances near the highly stressed grain boundaries, thus it is possible that a significant amount of plastic deformation could occur. Additionally, experimental studies have observed a viscoplastic response in lithium metal,[243] and therefore variations in the deposition rate would alter the local strain rate of the material and lead to strain hardening. Over time, plastic deformation might lead to areas of the anode separating from the protection layer, leading to hotspots of deposition.

These results demonstrate that, even for relatively high transference numbers, the presence of anisotropy in the mechanical properties or the microstructure of a protection layer directly leads to deformation of the lithium anode. Further studies on systems with only a small number of grains are being analyzed to gain mechanistic understanding of how the anisotropy affects the lithium anode.

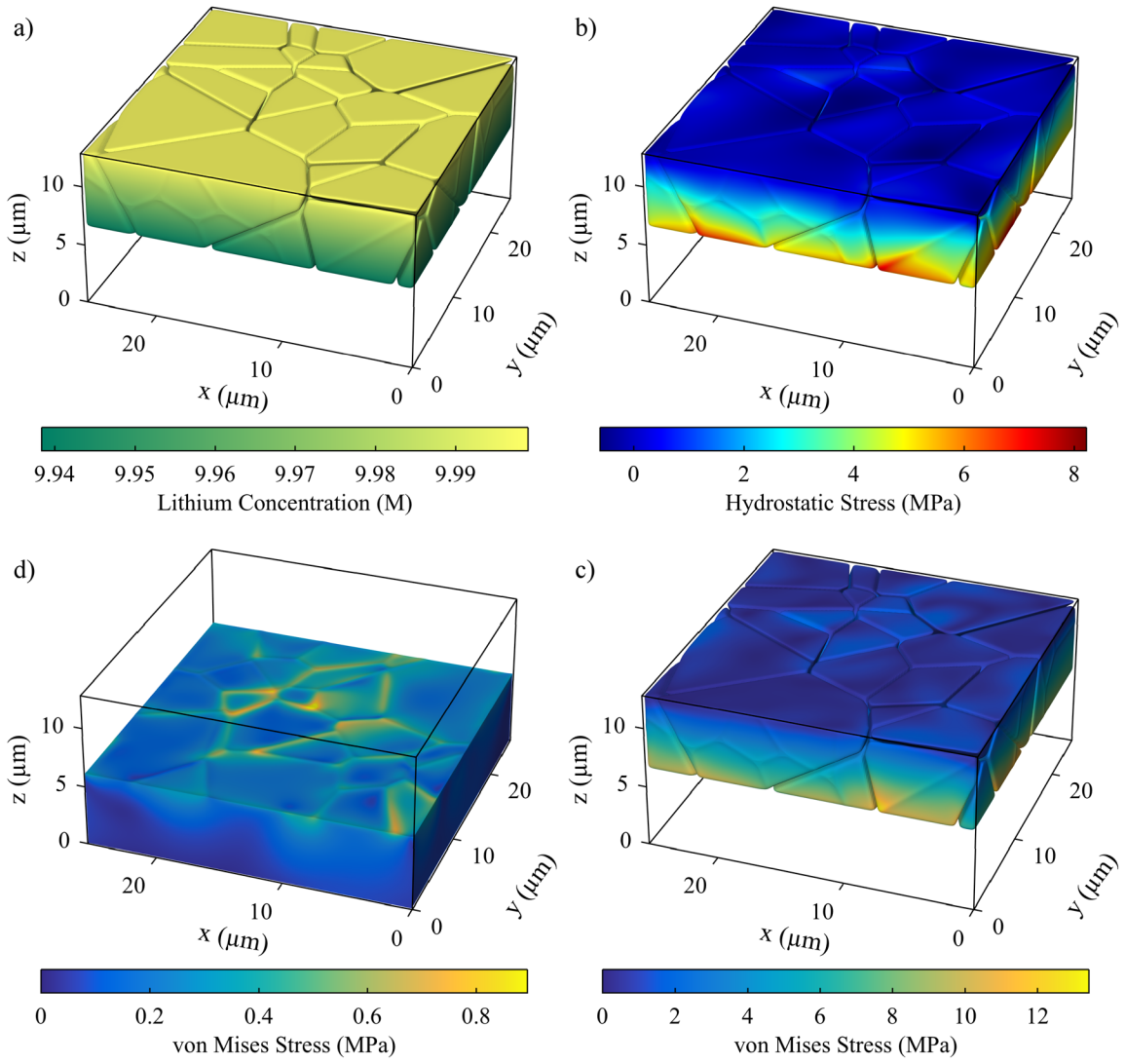

Figure 7.5. The simulated (a) concentration profile in the protection layer, (b) hydrostatic stress in the protection layer, (c) von Mises stress in the protection layer, and (d) von Mises stress in the lithium anode. Despite a generally linear concentration profile, there is a wide variation in the stress distributions in the protection layer due to the randomly oriented anisotropic grains. Additionally, the von Mises stress in the anode is comparable to the yield stress of lithium.

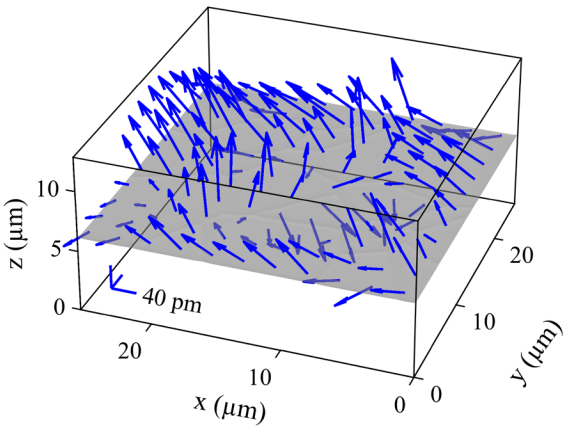

Figure 7.6. A quiver plot of the displacement field along the lithium anode isosurface. The length of each quiver is equal to 50,000 times the magnitude of the displacement vector at a given point. The small axes in the lower left corner of the plot indicate the scale of the displacement quivers in each direction.

Summary

In this chapter, we presented the formulation of a diffuse-interface mechanical equilibrium model using the smoothed boundary method. This was combined with to a model of transport to enable simulations of the coupled chemo-mechanical response of protected lithium-metal anodes where the protection layer had decomposed from a pristine, single-ion conducting condition to form mixed-ionic conductors. Preliminary results were presented to validate the model against an approximate analytical solution of the governing equations. The peak hydrostatic stress in the protection layer was evaluated both as a function of the lithium transference number in an isotropic material and as a function of the orientation of a cubic single-crystalline protection layer. Additional simulations were presented to examine the effect of anisotropy in the microstructure of the protection layer for a polycrystalline protection layer with randomly oriented cubic grains. These results indicate that presence of anisotropy in the protection layer leads to significant stress along the anode surface, which over time could lead to deformation of the anode.

Chapter 8.

Summary and Future Work

Dissertation Summary

In this dissertation, we investigated the coupled effects of ionic transport, the electrostatic potential, reaction kinetics, and morphological evolution on the resulting time-dependent behaviors of electrode and electrolyte systems. Three systems were examined: the deposition and dissolution of magnesium on gold via cyclic voltammetry, the galvanostatic cycling of lithium symmetric cells, and pitting corrosion of stainless steel. Chapter 3 presented the development of a new 1D modeling framework that employed a coarse-grained description of the electrode morphology to enable efficient simulations of magnesium deposition and dissolution. This model described transport and the electrostatic potential in the electrolyte using dilute solution theory. We proposed that at any point in time the electrode surface could be described in terms of a combination of existing magnesium deposits that could grow or dissolve and the remaining electrode area where nucleation of new deposits could occur. This assumption was implemented within a morphology-aware modification to the Butler-Volmer equation to capture the morphological evolution of the working electrode. The power of this approach was demonstrated by determining the unknown kinetic and transport properties of a $Mg(BH_4)_2$ electrolyte via fitting to an experimental voltammogram. Even with this limited input, the model determined estimates of the parameters that were comparable to available data in the literature, and the fitted

parameters predicted voltammograms at different experimental conditions that matched actual results.

In Chapter 4, we extended the 1D model to consider the behavior of a lithium symmetric cell over the early cycles of galvanostatic cycling. Specifically, the model was employed to gain insight into the sources of the characteristic double-peak behavior that is commonly observed in such cells. This application required the addition of moving boundaries to the model. Further, the morphology-aware Butler-Volmer model was generalized to consider a regime where parts of the lithium electrodes were covered in a thick SEI or other passivating layer while regions that had been freshly deposited upon (such as dendritic features) had a comparatively thin surface layer. We proposed that the regions with thinner layers would have faster reaction kinetics and that, as their relative surface area increased, there would be an attendant shift in the preferred reaction pathway. The model was fitted to an experimental voltage trace and we observed that the model was able to accurately capture the double-peak behavior. Analysis of the model agreed with visual observations[14] in that, when the electrodes were both "covered" in dendrite-like features, the cell polarization was at the minimum value for a given half-cycle. A parametric study of the model confirmed that these dendritic regions should have faster reaction kinetics because the surface area increase of the electrode alone was insufficient to produce the double peak. Additionally, the width of the second peak was found to directly correlate to the overall Coulombic efficiency of the reaction.

In Chapter 5, we presented the development of a combined phase-field/smoothed boundary method (PF/SBM) framework to simulate the microstructural evolution of stainless steels under artificial pitting corrosion conditions. To do so, we extended earlier versions of this method as introduced by DeWitt *et al.*[33] and Enrique *et al.*[34] to enable consideration of multiple

electrolyte species and grains/phases in the alloy microstructure in predicting concentration gradients, potential gradients, and microstructural evolution. We also developed an approach to capture IR- and transport-controlled kinetic regimes within the phase-field/smoothed boundary paradigm. Overall, resulting simulations produced predictions for the evolution of the corrosion pit morphology that agreed with experimental data in the literature. Additionally, the model directly considered the variation in IR-controlled kinetics along the metal/electrolyte interface and correctly captured the phenomenon where kinetic faceting of the microstructure only occurred below the transport-limited regime. Neither of these aspects of pitting corrosion have been extensively considered in previous modeling studies.

In addition, we presented the preliminary results of two other studies. In Chapter 6, we introduced a reduced-order version of the lithium symmetric cell model presented in Chapter 4. In this simplified model, we assume that the concentration profile of lithium in the electrolyte is essentially homogenous. Therefore, the electrolyte can be described by a resistor obeying Ohm's law. Preliminary results indicated that dramatic decreases in computational cost could be realized through this approach. Additionally, there does not appear to be a significant loss of accuracy by employing the reduced-order model, either with constant or variable concentration of the electrolyte salt, although further analysis will be performed to determine when such approximations can be made without loss of accuracy.

In Chapter 7, we presented initial results for a pseudo-steady-state diffuse-interface model to examine how the formation of concentration gradients in decomposed protection layer materials for lithium metal anodes can induce stress in the protection layer and anode. When anisotropy is present in the mechanical properties and morphology of the protection layer, there are spatial variations in the mechanical response. This leads to deformation of the lithium anode

and the formation of significant volumes of material near the protection layer grain boundaries that are above the yield stress of lithium. These results indicate that decomposition may in turn lead to variations in the lithium deposition behavior due to the distribution of stresses along the anode/protection layer interface. Further analysis will be performed to gain a deeper mechanistic understanding of the mechanical behavior of decomposed protection-layer materials resulting from the interplay between the anode/protection layer morphology and anisotropy in the mechanical properties.

In total, the models and results presented in this dissertation provide an understanding of the effects of morphological evolution at metal-electrode/electrolyte interfaces. There is a complex interplay amongst transport, electrostatics, reaction kinetics, and microstructural morphology that contributes to the time-dependent behavior of these systems. In regard to the open questions posed in Chapter 1, we determined that coarse-grained approximations of electrode morphologies are an effective tool in developing efficient numerical models of the electrode/electrolyte system. The model based on these approximations proved useful in determining multiple system parameters and gaining mechanistic insight into the surface reactions with limited amounts of experimental input. Additionally, we developed the capability to directly consider the effects of varying electrostatic potentials along a metal-electrode/electrolyte interface and examined how this variation affects the corrosion behavior of the metal under different experimental conditions.

Future Work

Beyond the preliminary studies that will be completed in the near future, there are multiple avenues for how the models in this dissertation could be extended and applied to new

applications. Extensions of the 1D high-throughput model and the 2D PF/SBM model will be discussed, along with applications where they could be combined in a multiscale approach.

One of the chief attractions of the 1D modeling framework is that it is heavily optimized for computational efficiency and can be parameterized with a variety of electrochemical measurements. With a large set of experimental results, the model could be applied to statistically obtain estimates of the kinetic and transport properties for a given combination of anode, cathode, and electrolyte. If the resulting database of fitted parameters was sufficiently large, data mining could be performed to search for parametric trends across a class of battery materials. This could potentially reveal what properties of the materials are most associated with long battery cycle life, fast discharge rates, low self-discharge, or other desirable battery benchmarks. As described in Chapter 3, the cell geometry would need to be accurately characterized to obtain the best parameter estimates, such as by employing a standardized form factor like a coin cell. Incorporating the model into a data-based workflow could also be performed in conjunction with atomistic modeling efforts instead of experimental studies. For example, one of the goals of the Electrolyte Genome Project[19] is to create a large database of candidate materials to enable next-generation batteries. The 1D model could be combined with such a database to calculate theoretical voltammetric behaviors of a candidate material. These simulated voltammograms could be compared against experimental results as an additional measure of the validity and accuracy of the parameters predicted through *ab initio* studies.

From a physics standpoint, the 1D model could be extended to a concentrated solution regime to improve its agreement in predicting the behavior of highly concentrated electrolytes such as those being developed for sparingly solvating electrolytes.[214] However, other than binary electrolytes as in the P2D model,[59] changing to concentrated solution theory introduces

significantly larger degrees of freedom to the mathematical description of the model.[35] Thus, there may be an associated tradeoff: the model may be theoretically more accurate within a given regime, but an increase in the number of degenerate solutions may increase the uncertainty in fitted parameters. Employing the reduced-order model may improve the accuracy of initial parameter estimates as it has fewer degrees of freedom. With the reduced-order model, the parameters associated with the reaction kinetics and morphological evolution could be determined while employing an initial set of volume-averaged transport properties. Then, the kinetic and morphology parameters could be held constant while the transport properties are refined with the full model.

One of the main limitations of the 1D modeling framework is that assumptions must be employed to construct the piecewise functions that describe the electrode surface morphology. For heavily faceted, potentially porous electrode morphologies, such functions may not be immediately attainable. However, experimental measurements could be employed to construct the mathematical functions with real microstructural observations, such as through image analysis of the data obtained with a visualization cell as in the work of Wood *et al.*[14] or tomographic data obtained via transmission x-ray microscopy. Constructing the morphology model could also be an application of the PF/SBM framework. A series of simulations could be performed to predict the evolution of the anode microstructure during deposition for a variety of initial conditions. Then, the surface areas and volumes required to generate the constitutive relationship in the 1D model could be calculated through post-processing of the data. For very large surface morphologies that may develop, the behavior after long-term deposition would perhaps need to be extrapolated from shorter time scales.

For the 2D PF/SBM framework, there are two areas where the existing model could be improved. With the addition of the maximum current density to the reaction kinetics (cf. Eqs. 5.19 and 5.20), the computational performance of the model noticeably decreased. It is possible that, due to this portion of the model being a more recent addition, the resulting code is not as well optimized as other parts of the code. However, there is also a possibility that improvements are needed in the numerical methods to increase the rate of convergence, such as by linearizing the governing equations and employing the Newton-Raphson method. Similarly to the decreased performance incurred by Eqs. 5.19 and 5.20, the code has not performed well on emerging highly threaded computing architectures such as the Intel Xeon Phi. Typically, the code runs three to four times more slowly on Xeon Phi as compared to typical Xeon-based hardware. Profiling of the code did not pinpoint an exact cause for this performance loss. Employing a hybrid MPI/OpenMP-based parallelization scheme may improve performance, although the existing codebase would likely need to be restructured to minimize the cost associated with creating teams of threads in OpenMP. Alternatively, the code may need to be redeveloped within frameworks and programming languages that have inherently embedded parallelism, such as the Kokkos framework[244] from Sandia National Laboratories or Chapel[245] from Cray.

An impactful application of the 2D PF/SBM framework would be to study the effects of microstructure on the observed corrosion of additively manufactured materials. In additively manufactured metals, it has recently been reported that the corrosion behavior of commercially important alloys such as 316L stainless steel and Ti-6Al-4V is significantly altered as compared to traditional processing techniques.[246–248] Some of these alloys exhibit a different degree of susceptibility to pitting corrosion, intergranular corrosion, and stress-enhanced corrosion than their traditionally processed equivalents. It is hypothesized that this difference arises due to

changes in the microstructure that occur with the additive manufacturing process.[248] Given that additively manufactured components are being examined for applications in corrosive environments under stress, such as for biomaterials[249] and nuclear materials,[250] it is critical that models be developed to understand how the microstructures and stresses evolve over the life of the component.

Appendices

Appendix A.

Derivation of the Maximum Reaction Current Density

Here, the derivation of the expression for the maximum corrosion current density, $i_{max,c}$, appearing in Eq. 5.19 in Chapter 5 is presented. As in previous models,[75–77,79] we assume that the rate of formation of the salt layer is assumed to be fast enough such that no supersaturation can occur in solution, and the exact thickness and morphology of the salt layer is neglected.

We consider a control volume at the metal/electrolyte interface in the plane of the interface with a thickness of 2δ and a cross-sectional area A. At any point in time, the metal ion concentration in this volume will be at or below its saturation limit, $c_{M,sat}$. For given values of the metal ion concentration gradient and the electrostatic potential gradient, there can be an imbalance between the inward flux of ions into the volume due to the corrosion reaction and the outward flux of ions into the electrolyte. Additionally, the corrosion reaction will cause movement of the diffuse interface, which increases the size of the control volume and therefore reduces the effective flux of metal ions due to the reaction. Over a characteristic time scale, τ, the concentration of metal ions in the control volume will evolve due to this imbalance:

$$\delta c_M \delta V = \left[\frac{i_{rxn}(1 - c_M V_M)}{z_M F} - \left(D_M \nabla c_M + z_M \frac{F}{RT} D_M c_M \nabla \Phi\right) \cdot \mathbf{n}\right] A\tau, \tag{A1}$$

where δc_M is the change in concentration in the control volume, $\delta V = 2\delta \cdot A$, and the term $(1 - c_M V_M)$ arises from the movement of the diffuse interface and the conservation of mass.[75,193] Under our assumption that saturation cannot be exceeded, there is a maximum value of i_{rxn} that,

when included in Eq. A1, will lead to saturation. Equation A1 can therefore be rewritten for this case as

$$\frac{c_{M,sat} - c_M}{\tau} = \frac{1}{2\delta}\left[\frac{i_{max,c}(1 - c_M V_M)}{z_M F} - \left(D_M \nabla c_M + z_M \frac{F}{RT} D_M c_M \nabla \Phi\right) \cdot \mathbf{n}\right], \tag{A2}$$

where $i_{max,c}$ is the maximum possible reaction current density. From Eq. A2, the maximum possible current density can be defined such that, over the characteristic time scale, τ, the current density would lead c_M to reach $c_{M,sat}$, or equivalently $c_{M,sat} - c_M$ becomes zero (i.e. the electrolyte becomes saturated with the metal ion). If the reaction current density is any higher, the concentration would exceed the saturation value. By rearranging Eq. A2, one obtains:

$$i_{max,c} = \left(\frac{z_M F}{1 - c_M V_M}\right)\left[\frac{2\delta}{\tau}\left(c_{M,sat} - c_M\right) + \left(D_M \nabla c_M + z_M \frac{F}{RT} D_M c_M \nabla \Phi\right) \cdot \mathbf{n}\right]. \tag{A3}$$

The first term on the right-hand side of Eq. A3 quantifies how far the metal ion concentration is from its saturation value; the larger this difference is, the greater $i_{max,c}$ is. The second term quantifies the portion of $i_{max,c}$ that is due to the rate of transport of metal ions to and from the electrolyte. When the direction of the concentration and potential gradients is such that metal ions are transported into the electrolyte, stronger magnitudes of these gradients increase $i_{max,c}$. When the direction of the gradients would lead to ions being transported towards the metal/electrolyte interface, stronger gradients would reduce the value of $i_{max,c}$.

Below saturation, the magnitude of the first term on the right-hand side of Eq. A3 varies with a characteristic velocity of the ionic transport across the interface, $2\delta/\tau$, whose value in turn depends upon the dominant transport process at the interface

$$\frac{2\delta}{\tau} = \max\left(\frac{2\delta}{\tau_{diff}}, \frac{2\delta}{\tau_{migr}}\right), \tag{A4}$$

where the two terms inside parentheses correspond to the characteristic velocities of diffusion and migration, respectively. The characteristic velocity for diffusion is

$$\frac{2\delta}{\tau_{diff}} = \frac{D_M}{2\delta}, \tag{A5}$$

and for migration, it is

$$\frac{2\delta}{\tau_{migr}} = \frac{z_M D_M F}{RT} |\nabla \Phi \cdot \mathbf{n}|. \tag{A6}$$

When migration is the dominant process according to Eq. A6, then the thickness of the diffuse interface is eliminated from Eq. A3. However, when diffusion is dominant, the value of the diffuse interface thickness will affect Eq. A3. Choosing the smaller value of the characteristic velocity, rather than the greater value as in Eq. A4, would reduce the limiting current below what the present conditions of the electrolyte could sustain. For example, in the model initial conditions, the metal ion concentration and the electrostatic potential are initially zero everywhere. If Eq. A6 was always chosen for the characteristic velocity, then the initial maximum current would be zero; no current would be able to flow throughout the simulation. Near saturation, when the current would approach its limiting value, the term $(c_{M,sat} - c_M)/\tau$ becomes small and only the transport portion of the maximum current is significant, and thus the exact value of τ should have a minimal effect on the result. Equations A3 through A6 are implemented within the main loop of the simultaneous solver that is described in the numerical methods subsection. Therefore, the value of $i_{max,c}$ is always calculated with the newest estimates of the metal cation concentration at the next time step, which prevents the concentration from ever exceeding saturation.

Figure A1 plots the behavior of $i_{max,c}$ over time and the individual components due to saturation ($i^s_{max,c}$, the first term in Eq. A3), diffusion ($i^d_{max,c}$, the term containing ∇c_M), and

migration ($i^m_{max,c}$, the term containing $\nabla\Phi$) for -60 mV vs. SCE and 100 mV vs. SCE applied potentials. For the -60 mV vs. SCE case, the concentration (cf. Fig. 3a) is far from saturation throughout the simulation, and thus the maximum current is dominated by $i^s_{max,c}$. However, the maximum value of $i_{rxn}/i_{max,c}$ is about 0.052; thus the maximum current has a minimal impact on the observed current density. In comparison, for the 100 mV vs. SCE case, the concentration is asymptotically approaching saturation and $i^m_{max,c}$ is the dominant component of the maximum current density. The minimum value of $i_{rxn}/i_{max,c}$ is 0.889 and the maximum value is 0.999, therefore the current density is strongly transport-controlled.

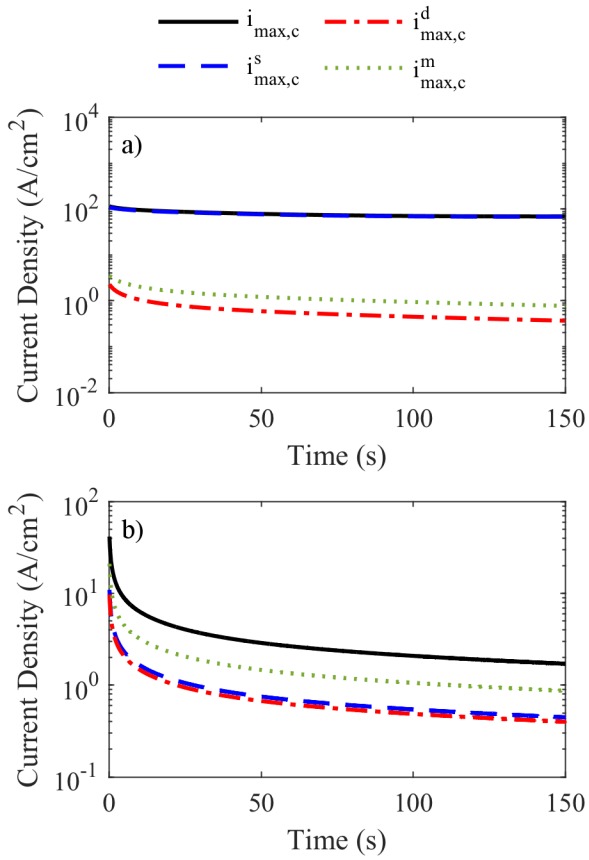

Figure A.1. The contributions of the individual components of Eq. A3 to the value of $i_{max,c}$ over time for (a) -60 mV vs. SCE and (b) 100 mV vs. SCE. In (a), the metal ion concentration remains far from saturation and thus the maximum current density is dominated by $i^s_{max,c}$, whereas in (b) the concentration is asymptotically approaching saturation and the largest component is $i^m_{max,c}$.

Appendix B.

Derivation of the Analytical Expression for the Stress in the Protection Layer

In this appendix, an analytical solution is provided for the protection layer mechanical behavior model in Chapter 7. We derive a pseudo-one-dimensional model of the stress in the protection layer by finding an analytical solution to Eq. 7.1. First, we assume that the protection layer has uniform, but not necessarily isotropic, material properties. Furthermore, we only consider an infinitesimally small portion of the protection layer along the z-axis, and we assume that this sliver of material is uniform within the x-y plane. Within these assumptions, any derivatives in the x and y directions have a value of zero by necessity, and therefore Eq. 7.1 may be simplified:

$$\begin{cases} \dfrac{d\sigma_3}{dz} = 0 \\ \dfrac{d\sigma_4}{dz} = 0, \\ \dfrac{d\sigma_5}{dz} = 0 \end{cases} \tag{B.1}$$

Equation B.1 implies that σ_3, σ_4, and σ_5 are all constant throughout the protection layer in this pseudo-one-dimensional solution. The value of this constant stress is obtained through the boundary condition. Here, we assume that the surface of the protection layer in contact with a liquid electrolyte experiences no traction, which mathematically may be expressed as

$$\mathbf{T} = \mathbf{n} \cdot \boldsymbol{\sigma} = 0, \tag{B.2}$$

where $\mathbf{T}$ is the traction vector and $\mathbf{n}$ is the unit normal vector of the surface. Equation B.2 may be further expanded in terms of its components:

$$\begin{cases} \sigma_1 \mathbf{n}_x + \sigma_6 \mathbf{n}_y + \sigma_5 \mathbf{n}_z = 0 \\ \sigma_6 \mathbf{n}_x + \sigma_2 \mathbf{n}_y + \sigma_4 \mathbf{n}_z = 0, \\ \sigma_5 \mathbf{n}_x + \sigma_4 \mathbf{n}_y + \sigma_3 \mathbf{n}_z = 0 \end{cases} \tag{B.3}$$

where $\mathbf{n}_x$, $\mathbf{n}_y$, and $\mathbf{n}_z$ are the x, y, and z components of the normal vector. At the protection layer surface, $\mathbf{n}_x = \mathbf{n}_y = 0$, and $\mathbf{n}_z = 1$. Thus, in addition to being constant, we conclude that $\sigma_3 = \sigma_4 = \sigma_5 = 0$ throughout the protection layer. The presented analytical solution will therefore satisfy the assumption of plane stress, which is often applicable in thin films.[233] As a consequence of assuming that the interface between the protection layer and the electrolyte is traction-free, the analytical model requires that the interface between the layer and the lithium substrate also be traction-free. Lithium is a soft metal,[241,251] and as such this should be a reasonable approximation for comparatively stiffer protection layer materials.

With the knowledge that the protection layer is in plane stress, it is now possible to solve for the displacements in the protection layer. Within the assumption of uniformity in the x-y plane, as in the stress tensor, all partial derivatives with respect to x and y are also zero in the strain tensor. This allows the equation for a given stress component to be reformulated as:

$$\begin{aligned} \sigma_i = C_{i5} \frac{du}{dz} + C_{i4} \frac{dv}{dz} + C_{i3} \frac{dw}{dz} \\ - (c_+ - \bar{c}_+)[C_{i1}\beta_1 + C_{i2}\beta_2 + C_{i3}\beta_3 + 2(C_{i4}\beta_4 + C_{i5}\beta_5 + C_{i6}\beta_6)], \end{aligned} \tag{B.4}$$

where the subscript i represents one of the six individual components of the tensor. Having established that $\sigma_3 = \sigma_4 = \sigma_5 = 0$, Eq. B.4 can explicitly be expanded for these three components of the tensor. This expansion represents a linear system of equations with at most three unknowns ($\epsilon_5 = du/dz$, $\epsilon_4 = dv/dz$, and $\epsilon_3 = dw/dz$) that is significantly simpler than the original system of coupled partial differential equations, and the spatially-dependent solution can be solved analytically at each point in the protection layer. The only remaining component required for this solution is the lithium concentration as a function of position, which we describe

in the following section. With the solutions to Eq. B.4, the remaining components of the stress tensor may be evaluated at each point, and the analytical von Mises and hydrostatic stresses can be calculated. Depending upon the symmetry properties of the protection layer material, simplifications are possible for the analytical solution.

Concentration Profile Across the Protection Layer

To calculate the stress across the protection layer, we need to know the spatially varying concentration of lithium ions. Using Eqs. 7.10-7.14 and 7.16 and applying the approximation described above that allows for a 1D treatment, the overall fluxes at the protection layer/anode interface can be written as:

$$\frac{i}{F} + \frac{F}{RT} D_+ c_+^F \frac{d\Phi}{dz} = -\frac{F}{RT} D_+ c_+^M \frac{d\Phi}{dz} - D_+ \frac{dc_+^M}{dz}, \tag{B.5a}$$

$$0 = \frac{F}{RT} D_+ c_+^M \frac{d\Phi}{dz} - D_+ \frac{dc_+^M}{dz}, \tag{B.5b}$$

where i is the current density at the interface, F is Faraday's constant, R is the ideal gas constant, T is the absolute temperature, D_+ is the lithium cation diffusivity, and Φ is the electrostatic potential.[35] Equation B.5b can be employed to eliminate the effects of electrostatic migration upon c_+^M in the right-hand side of Eq. B.5a:

$$\frac{i}{F} + \frac{F}{RT} D_+ c_+^F \frac{d\Phi}{dz} = -2D_+ \frac{dc_+^M}{dz}. \tag{B.6}$$

From Eq. B.6, we observe that c_M^+ and c_M^- behave much like a binary electrolyte. At steady-state, the transport of lithium ions in the protection layer therefore satisfies the condition[35]

$$\frac{d^2 c_+^M}{dz^2} = 0. \tag{B.7}$$

To solve Eq. B.7, we assume that $d\Phi/dz$ is constant throughout the protection layer and that at the edge of the decomposed region with thickness L_{PL}^D, $c_+^M = \bar{c}_+^M$. Additionally, the charge in the

protection layer is locally conserved, which implies $di/dz = 0$.[35] Under these assumptions, an analytical solution of Eq. B.7 can be obtained:

$$c_+^M(z) = \bar{c}_+^M - \frac{1}{2}\left[\frac{F}{RT}c_+^F\frac{d\Phi}{dz} + \frac{i}{D_+F}\right](z - L_{PL}). \tag{B.8}$$

To determine the value of $d\Phi/dz$, as a first approximation, we assume that the protection layer obeys Ohm's law:

$$\frac{d\Phi}{dz} = -\frac{i}{\bar{\kappa}} = -\frac{iRT}{F^2D_+(\bar{c}_+^F + 2\bar{c}_+^M)} = -\frac{iRTt_+}{F^2D_+\bar{c}_+}, \tag{B.9}$$

where $\bar{\kappa}$ is the bulk conductivity calculated from the initial concentrations of each species.[35] Equation B.11 can now be simplified as:

$$c_+^M(z) = \bar{c}_+^M - i\frac{(1 - t_+)}{D_+F} \cdot (z - L_{PL}). \tag{B.10}$$

The total lithium concentration at any point will be the sum of c_+^M and the constant value of c_+^F, and thus we obtain the ansatz of the lithium concentration in the protection layer:

$$c_+(z) = \bar{c}_+ - i\frac{(1 - t_+)}{D_+F} \cdot (z - L_{PL}), \tag{B.11}$$

which, when combined with Eq. B.4, forms the complete analytical solution for the stress in the protection layer. When the transference number is unity, Eq. B.11 correctly captures a constant cation concentration, and the largest concentration differences would occur as t_+ approaches 0.5. During charging (negative current densities), the concentration will decrease at the interface ($z = 0$). The magnitude of this decrease is bounded, however; at a strong enough current density, c_+^M will approach zero at the interface and the overall lithium concentration should not decrease further.

Bibliography

1. International Energy Agency, *Global EV Outlook 2017: Two million and counting*, p. 1-71, (2017).

2. World Energy Council, *World Energy Resources - E-Storage*, p. 60, (2016).

3. G. Koch, J. Varney, N. Thompson, O. Moghissi, M. Gould, and J. Payer, *International Measures of Prevention, Application, and Economics of Corrosion Technologies Study*, p. 1-216, Houston, TX, (2016).

4. National Transportation Safety Board, *Collapse of I-35W Highway Bridge Minneapolis, Minnesota August 1, 2007*, p. 178, Washington, D.C., (2007).

5. P. Arora, M. Doyle, and R. E. White, *J. Electrochem. Soc.*, **146**, 3543 (1999).

6. F. Lambert, (2016) https://electrek.co/2016/02/03/tesla-battery-tear-down-85-kwh/.

7. Panasonic, *Panasonic Lithium Ion NCR18650 Datasheet*, p. 1, (2012).

8. H. D. Yoo, I. Shterenberg, Y. Gofer, G. Gershinsky, N. Pour, and D. Aurbach, *Energy Environ. Sci.*, **6**, 2265 (2013).

9. R. Huggins, *Advanced Batteries*, Springer US, Boston, MA, (2009).

10. M. Armand and J.-M. Tarascon, *Nature*, **451**, 652–657 (2008).

11. K. Xu, *Chem. Rev.*, **114**, 11503–11618 (2014).

12. J. S. Lee, S. T. Kim, R. Cao, N. S. Choi, M. Liu, K. T. Lee, and J. Cho, *Adv. Energy Mater.*, **1**, 34–50 (2011).

13. J. Steiger, G. Richter, M. Wenk, D. Kramer, and R. Mönig, *Electrochem. commun.*, **50**, 11–14 (2015).

14. K. N. Wood, E. Kazyak, A. F. Chadwick, K.-H. Chen, J.-G. Zhang, K. Thornton, and N. P. Dasgupta, *ACS Cent. Sci.*, **2**, 790–801 (2016).

15. D. J. Wetzel, M. A. Malone, R. T. Haasch, Y. Meng, H. Vieker, N. T. Hahn, A.

Gölzhäuser, J.-M. Zuo, K. R. Zavadil, A. A. Gewirth, and R. G. Nuzzo, *ACS Appl. Mater. Interfaces*, **7**, 18406–18414 (2015).

16. E. Peled, *J. Electrochem. Soc.*, **126**, 2047 (1979).

17. G. S. Frankel, *J. Electrochem. Soc.*, **145**, 2186 (1998).

18. S. M. Ghahari, D. Krouse, N. Laycock, T. Rayment, C. Padovani, M. Stampanoni, F. Marone, R. Mokso, and A. J. Davenport, *Corros. Sci.*, **100**, 23–35 (2015).

19. X. Qu, A. Jain, N. N. Rajput, L. Cheng, Y. Zhang, S. P. Ong, M. Brafman, E. Maginn, L. A. Curtiss, and K. A. Persson, *Comput. Mater. Sci.*, **103**, 56–67 (2015).

20. L. Cheng, R. S. Assary, X. Qu, A. Jain, S. P. Ong, N. N. Rajput, K. Persson, and L. A. Curtiss, *J. Phys. Chem. Lett.*, **6**, 283–291 (2015).

21. N. Kumar and D. J. Siegel, *J. Phys. Chem. Lett.*, **7**, 874–881 (2016).

22. S. H. Lapidus, N. N. Rajput, X. Qu, K. W. Chapman, K. A. Persson, and P. J. Chupas, *Phys. Chem. Chem. Phys.*, **16**, 21941–21945 (2014).

23. P. Canepa, G. S. Gautam, R. Malik, S. Jayaraman, Z. Rong, K. R. Zavadil, K. Persson, and G. Ceder, *Chem. Mater.*, **27**, 3317–3325 (2015).

24. S. Yu, R. D. Schmidt, R. Garcia-Mendez, E. Herbert, N. J. Dudney, J. B. Wolfenstine, J. Sakamoto, and D. J. Siegel, *Chem. Mater.*, **28**, 197–206 (2016).

25. H. Liu, M. J. Choe, R. A. Enrique, B. Orvañanos, L. Zhou, T. Liu, K. Thornton, and C. P. Grey, *J. Phys. Chem. C*, **121**, 12025–12036 (2017).

26. J. Bhattacharya and A. Van der Ven, *Phys. Rev. B*, **81**, 104304 (2010).

27. S. DeWitt and K. Thornton, in *Computational Materials System Design*,, p. 67–87, Springer International Publishing, Cham (2018).

28. *Modeling Across Scales: A Roadmapping Study for Connecting Materials Models and Simulations Across Length and Time Scales*, Warrendale, Pennsylvania, (2015).

29. J. A. V. Butler, *Trans. Faraday Soc.*, **19**, 659 (1924).

30. J. A. V. Butler, *Trans. Faraday Soc.*, **19**, 729–733 (1924).

31. J. A. V. Butler, *Trans. Faraday Soc.*, **19**, 734 (1924).

32. T. Erdey-Grúz and M. Volmer, *Zeitschrift für Phys. Chemie*, **150A**, 203–213 (1930).

33. S. DeWitt, N. Hahn, K. Zavadil, and K. Thornton, *J. Electrochem. Soc.*, **163**, A513–A521 (2016).

34. R. A. Enrique, S. DeWitt, and K. Thornton, *MRS Commun.*, **7**, 658–663 (2017).

35. J. Newman and K. E. Thomas-Alyea, *Electrochemical Systems*, Third., Wiley Interscience, Hoboken, New Jersey, (2004).

36. G. S. Frankel, in *Active Protective Coatings*, Springer Series in Materials Science. A. E. Hughes, J. M. C. Mol, M. L. Zheludkevich, and R. G. Buchheit, Editors, vol. 233, p. 17, Springer Netherlands, Dordrecht (2016).

37. A. J. Bard and L. R. Faulkner, *Electrochemical Methods: Fundamentals and Applications*, Second., John Wiley & Sons, Inc., Hoboken, New Jersey, (2001).

38. M. Planck, *Ann. der Phys. und Chemie*, **276**, 561–576 (1890).

39. M. Planck, *Ann. der Phys. und Chemie*, **275**, 161–186 (1890).

40. M. Planck, *Z. Phys.*, **94**, 469–472 (1935).

41. F. G. Cottrell, *Z. Phys. Chem.*, **42**, 385–431 (1903).

42. R. S. Nicholson and I. Shain, *Anal. Chem.*, **36**, 706–723 (1964).

43. R. S. Nicholson, *Anal. Chem.*, 1351–1355 (1965).

44. W. Nernst, *Zeitschrift für Phys. Chemie*, **4U**, 129–181 (1889).

45. E. J. F. Dickinson, J. G. Limon-Petersen, and R. G. Compton, *J. Solid State Electrochem.*, **15**, 1335–1345 (2011).

46. H. Cohen and J. W. Cooley, *Biophys. J.*, **5**, 145–162 (1965).

47. J. R. Sandifer and R. P. Buck, *J. Phys. Chem.*, **79**, 384–392 (1974).

48. T. R. Brumleve and R. P. Buck, *J. Electroanal. Chem. Interfacial Electrochem.*, **90**, 1–31 (1978).

49. I. Streeter and R. G. Compton, *J. Phys. Chem. C*, **112**, 13716–13728 (2008).

50. E. J. F. Dickinson, J. G. Limon-Petersen, N. V Rees, and R. G. Compton, *J. Phys. Chem. C*, **113**, 11157–11171 (2009).

51. J. W. Tester and H. S. Isaacs, *J. Electrochem. Soc.*, **122**, 1438 (1975).

52. J. R. Galvele, *J. Electrochem. Soc.*, **123**, 464 (1976).

53. S. M. Sharland and P. W. Tasker, *Corros. Sci.*, **28**, 603–620 (1988).

54. S. M. Sharland, *Corros. Sci.*, **28**, 621–630 (1988).

55. J. Euler and W. Nonnenmacher, *Electrochim. Acta*, **2**, 268–286 (1960).

56. J. S. Newman and C. W. Tobias, *J. Electrochem. Soc.*, **109**, 1183 (1962).

57. R. de Levie, *Electrochim. Acta*, **8**, 751–780 (1963).

58. J. Newman and W. Tiedemann, *AIChE J.*, **21**, 25–41 (1975).

59. M. Doyle, T. F. Fuller, and J. Newman, *J. Electrochem. Soc.*, **140**, 1526 (1993).

60. T. F. Fuller, M. Doyle, and J. Newman, *J. Electrochem. Soc.*, **141**, 1 (1994).

61. M. Doyle, J. Newman, A. S. Gozdz, C. N. Schmutz, and J.-M. Tarascon, *J. Electrochem. Soc.*, **143**, 1890 (1996).

62. M. Schmuck and M. Z. Bazant, *SIAM J. Appl. Math.*, **75**, 1369–1401 (2015).

63. D. Wheeler, D. Josell, and T. P. Moffat, *J. Electrochem. Soc.*, **150**, C302 (2003).

64. J. E. Guyer, W. J. Boettinger, J. A. Warren, and G. B. McFadden, *Phys. Rev. E*, **69**, 021603 (2004).

65. J. E. Guyer, W. J. Boettinger, J. A. Warren, and G. B. McFadden, *Phys. Rev. E*, **69**, 021604 (2004).

66. J. Deng, G. J. Wagner, and R. P. Muller, *J. Electrochem. Soc.*, **160**, A487–A496 (2013).

67. Y. Shibuta, Y. Okajima, and T. Suzuki, *Sci. Technol. Adv. Mater.*, **8**, 511–518 (2007).

68. L. Liang, Y. Qi, F. Xue, S. Bhattacharya, S. J. Harris, and L. Q. Chen, *Phys. Rev. E*, **86**, 1–5 (2012).

69. L. Liang and L.-Q. Chen, *Appl. Phys. Lett.*, **105**, 263903 (2014).

70. D. A. Cogswell, *Phys. Rev. E*, **92**, 011301 (2015).

71. D. R. Ely, A. Jana, and R. E. García, *J. Power Sources*, **272**, 581–594 (2014).

72. J. W. Cahn and J. E. Hilliard, *J. Chem. Phys.*, **28**, 258–267 (1958).

73. H.-C. Yu, H.-Y. Chen, and K. Thornton, *Model. Simul. Mater. Sci. Eng.*, **20**, 075008 (2012).

74. S. M. Allen and J. W. Cahn, *Acta Metall.*, **27**, 1085–1095 (1979).

75. S. Scheiner and C. Hellmich, *Comput. Methods Appl. Mech. Eng.*, **198**, 2898–2910 (2009).

76. S. Scheiner and C. Hellmich, *Corros. Sci.*, **49**, 319–346 (2007).

77. R. Duddu, *Comput. Mech.*, **54**, 613–627 (2014).

78. Z. Chen and F. Bobaru, *J. Mech. Phys. Solids*, **78**, 352–381 (2015).

79. W. Mai, S. Soghrati, and R. G. Buchheit, *Corros. Sci.*, **110**, 157–166 (2016).

80. Z. Chen, G. Zhang, and F. Bobaru, *J. Electrochem. Soc.*, **163**, C19–C24 (2016).

81. N. J. Laycock and S. P. White, *J. Electrochem. Soc.*, **148**, B264 (2001).

82. K. B. Deshpande, *Electrochim. Acta*, **56**, 1737–1745 (2011).

83. L. Yin, Y. Jin, C. Leygraf, and J. Pan, *Electrochim. Acta*, **192**, 310–318 (2016).

84. R. Duddu, N. Kota, and S. M. Qidwai, *J. Appl. Mech.*, **83**, 081003 (2016).

85. W. Mai and S. Soghrati, *Electrochim. Acta*, **260**, 290–304 (2018).

86. S. Jafarzadeh, Z. Chen, and F. Bobaru, *Corrosion*, **74**, 393–414 (2018).

87. S. M. Ghahari, thesis, University of Birmingham (2012).

88. C. Monroe and J. Newman, *J. Electrochem. Soc.*, **152**, A396 (2005).

89. Z. Ahmad and V. Viswanathan, *Phys. Rev. Mater.*, **1**, 055403 (2017).

90. P. Barai, K. Higa, and V. Srinivasan, *J. Electrochem. Soc.*, **164**, A180–A189 (2017).

91. A. Ferrese and J. Newman, *J. Electrochem. Soc.*, **161**, A948–A954 (2014).

92. S. A. Roberts, V. E. Brunini, K. N. Long, and A. M. Grillet, *J. Electrochem. Soc.*, **161**, F3052–F3059 (2014).

93. W. H. Woodford, Y.-M. Chiang, and W. C. Carter, *J. Electrochem. Soc.*, **157**, A1052 (2010).

94. G. Bucci, T. Swamy, S. Bishop, B. W. Sheldon, Y.-M. Chiang, and W. C. Carter, *J. Electrochem. Soc.*, **164**, A645–A654 (2017).

95. H. Wang, Y.-I. Jang, B. Huang, D. R. Sadoway, and Y.-M. Chiang, *J. Electrochem. Soc.*, **146**, 473–480 (1999).

96. W. H. Woodford, W. C. Carter, and Y.-M. Chiang, *Energy Environ. Sci.*, **5**, 8014 (2012).

97. W. Mai and S. Soghrati, *Corros. Sci.*, **125**, 87–98 (2017).

98. T. D. Gregory, R. J. Hoffman, and R. C. Winterton, *J. Electrochem. Soc.*, **137**, 775–780 (1990).

99. D. Aurbach, Z. Lu, A. Schechter, Y. Gofer, H. Gizbar, R. Turgeman, Y. Cohen, M. Moshkovich, and E. Levi, *Nature*, **407**, 724–7 (2000).

100. M. Matsui, *J. Power Sources*, **196**, 7048–7055 (2011).

101. A. Benmayza, M. Ramanathan, T. S. Arthur, M. Matsui, F. Mizuno, J. Guo, P.-A. Glans, and J. Prakash, *J. Phys. Chem. C*, **117**, 26881–26888 (2013).

102. F. Mizuno, N. Singh, T. S. Arthur, P. T. Fanson, M. Ramanathan, A. Benmayza, J. Prakash, Y.-S. Liu, P.-A. Glans, and J. Guo, *Front. Energy Res.*, **2**, 1–11 (2014).

103. T. J. Carter, R. Mohtadi, T. S. Arthur, F. Mizuno, R. Zhang, S. Shirai, and J. W. Kampf, *Angew. Chemie Int. Ed.*, **53**, 3173–3177 (2014).

104. C. J. Barile, R. Spatney, K. R. Zavadil, and A. A. Gewirth, *J. Phys. Chem. C*, **118**, 10694–10699 (2014).

105. C. J. Barile, E. C. Barile, K. R. Zavadil, R. G. Nuzzo, and A. A. Gewirth, *J. Phys. Chem. C*, **118**, 27623–27630 (2014).

106. J. Muldoon, C. B. Bucur, A. G. Oliver, T. Sugimoto, M. Matsui, H. S. Kim, G. D. Allred, J. Zajicek, and Y. Kotani, *Energy Environ. Sci.*, **5**, 5941 (2012).

107. J. Muldoon, C. B. Bucur, A. G. Oliver, J. Zajicek, G. D. Allred, and W. C. Boggess, *Energy Environ. Sci.*, **6**, 482–487 (2013).

108. R. Mohtadi, M. Matsui, T. S. Arthur, and S.-J. Hwang, *Angew. Chemie Int. Ed.*, **51**, 9780–9783 (2012).

109. Y. Shao, T. Liu, G. Li, M. Gu, Z. Nie, M. Engelhard, J. Xiao, D. Lv, C. Wang, J.-G. Zhang, and J. Liu, *Sci. Rep.*, **3**, 3130 (2013).

110. Y. Shao, M. Gu, X. Li, Z. Nie, P. Zuo, G. Li, T. Liu, J. Xiao, Y. Cheng, C. Wang, J.-G.

Zhang, and J. Liu, *Nano Lett.*, **14**, 255–260 (2014).

111. T. Liu, Y. Shao, G. Li, M. Gu, J. Hu, S. Xu, Z. Nie, X. Chen, C. Wang, and J. Liu, *J. Mater. Chem. A*, **2**, 3430 (2014).

112. I. Shterenberg, M. Salama, Y. Gofer, E. Levi, and D. Aurbach, *MRS Bull.*, **39**, 453–460 (2014).

113. N. N. Rajput, X. Qu, N. Sa, A. K. Burrell, and K. A. Persson, *J. Am. Chem. Soc.*, **137**, 3411–3420 (2015).

114. T. Kakibe, J. Hishii, N. Yoshimoto, M. Egashira, and M. Morita, *J. Power Sources*, **203**, 195–200 (2012).

115. S.-Y. Ha, Y.-W. Lee, S. W. Woo, B. Koo, J.-S. Kim, J. Cho, K. T. Lee, and N.-S. Choi, *ACS Appl. Mater. Interfaces*, **6**, 4063–4073 (2014).

116. F. Tuerxun, Y. Abulizi, Y. NuLi, S. Su, J. Yang, and J. Wang, *J. Power Sources*, **276**, 255–261 (2015).

117. G. Vardar, A. E. S. Sleightholme, J. Naruse, H. Hiramatsu, D. J. Siegel, and C. W. Monroe, *ACS Appl. Mater. Interfaces*, **6**, 18033–18039 (2014).

118. R. E. Doe, R. Han, J. Hwang, A. J. Gmitter, I. Shterenberg, H. D. Yoo, N. Pour, and D. Aurbach, *Chem. Commun.*, **50**, 243–245 (2014).

119. Z. Lu, A. Schechter, M. Moshkovich, and D. Aurbach, *J. Electroanal. Chem.*, **466**, 203–217 (1999).

120. D. Aurbach, Y. Gofer, Z. Lu, A. Schechter, O. Chusid, H. Gizbar, Y. Cohen, V. Ashkenazi, M. Moshkovich, and R. Turgeman, *J. Power Sources*, **97–98**, 28–32 (2001).

121. C. Liebenow, Z. Yang, and P. Lobitz, *Electrochem. Commun.*, **2**, 641–645 (2000).

122. D. Aurbach, H. Gizbar, A. Schechter, O. Chusid, H. E. Gottlieb, Y. Gofer, and I. Goldberg, *J. Electrochem. Soc.*, **149**, A115 (2002).

123. N. W. Kondyrew and D. P. Manojew, *Ber. Dtsch. Chem. Ges.*, **58**, 464–467 (1925).

124. W. V. Evans and F. H. Lee, *J. Am. Chem. Soc.*, **55**, 1474–1477 (1933).

125. W. V. Evans, F. H. Lee, and C. H. Lee, *J. Am. Chem. Soc.*, **57**, 489–490 (1935).

126. R. E. Dessy and R. M. Jones, *J. Org. Chem.*, **24**, 1685–1689 (1959).

127. L. Martinot, *Bull. des Soc. Chim. Belges*, **75**, 711–724 (1966).

128. L. Martinot, *Bull. des Soc. Chim. Belges*, **76**, 617–630 (1967).

129. J. D. Genders and D. Pletcher, *J. Electroanal. Chem.*, **199**, 93–100 (1986).

130. Z. Feng, Y. NuLi, J. Wang, and J. Yang, *J. Electrochem. Soc.*, **153**, C689 (2006).

131. A. F. Chadwick, G. Vardar, S. DeWitt, A. E. S. Sleightholme, C. W. Monroe, D. J. Siegel, and K. Thornton, *J. Electrochem. Soc.*, **163**, A1813–A1821 (2016).

132. H. Noth, *Angew. Chemie*, **73**, 371–383 (1961).

133. A. E. Shirk and D. F. Shriver, *J. Am. Chem. Soc.*, **95**, 5901–5904 (1973).

134. E. J. F. Dickinson and R. G. Compton, *Chem. Phys. Lett.*, **497**, 178–183 (2010).

135. R. He, S. Chen, F. Yang, and B. Wu, *J. Phys. Chem. B*, **110**, 3262–3270 (2006).

136. C. Liebenow, *J. Appl. Electrochem.*, **27**, 221–225 (1997).

137. D. Aurbach, G. S. Suresh, E. Levi, A. Mitelman, O. Mizrahi, O. Chusid, and M. Brunelli, *Adv. Mater.*, **19**, 4260–4267 (2007).

138. J. G. Limon-Petersen, I. Streeter, N. V. Rees, and R. G. Compton, *J. Phys. Chem. C*, **113**, 333–337 (2009).

139. M. Z. Bazant, K. Thornton, and A. Ajdari, *Phys. Rev. E*, **70**, 021506 (2004).

140. J. A. Riddick and W. B. Bunger, *Organic Solvents: Physical Properties and Methods of Purification*, 3rd ed., Wiley Interscience, New York, (1970).

141. M. W. Verbrugge and B. J. Koch, *J. Electrochem. Soc.*, **141**, 3053 (1994).

142. J. O. M. Bockris and Z. Nagy, *J. Chem. Educ.*, **50**, 839 (1973).

143. R. Guidelli, R. G. Compton, J. M. Feliu, E. Gileadi, J. Lipkowski, W. Schmickler, and S. Trasatti, *Pure Appl. Chem.*, **86**, 245–258 (2014).

144. J. C. Myland and K. B. Oldham, *Anal. Chem.*, **72**, 3972–3980 (2000).

145. P. G. Bruce, L. J. Hardwick, and K. M. Abraham, *MRS Bull.*, **36**, 506–512 (2011).

146. J. Steiger, D. Kramer, and R. Mönig, *J. Power Sources*, **261**, 112–119 (2014).

147. J. Steiger, D. Kramer, and R. Mönig, *Electrochim. Acta*, **136**, 529–536 (2014).

148. E. Kazyak, K. N. Wood, and N. P. Dasgupta, *Chem. Mater.*, **27**, 6457–6462 (2015).

149. X.-B. Cheng and Q. Zhang, *J. Mater. Chem. A*, **3**, 7207–7209 (2015).

150. F. Ding, W. Xu, G. L. Graff, J. G. Zhang, M. L. Sushko, X. Chen, Y. Shao, M. H. Engelhard, Z. Nie, J. Xiao, X. Liu, P. V. Sushko, J. Liu, and J. G. Zhang, *J. Am. Chem. Soc.*, **135**, 4450–4456 (2013).

151. J. Qian, W. A. Henderson, W. Xu, P. Bhattacharya, M. Engelhard, O. Borodin, and J.-G. Zhang, *Nat. Commun.*, **6**, 6362 (2015).

152. N. Schweikert, A. Hofmann, M. Schulz, M. Scheuermann, S. T. Boles, T. Hanemann, H. Hahn, and S. Indris, *J. Power Sources*, **228**, 237–243 (2013).

153. W. Xu, J. Wang, F. Ding, X. Chen, E. Nasybulin, Y. Zhang, and J.-G. Zhang, *Energy Environ. Sci.*, **7**, 513–537 (2014).

154. L. O. Valøen and J. N. Reimers, *J. Electrochem. Soc.*, **152**, A882 (2005).

155. H. Wang, A. Thiele, and L. Pilon, *J. Phys. Chem. C*, **117**, 18286–18297 (2013).

156. S. DeWitt and K. Thornton, *Langmuir*, **30**, 5314–5325 (2014).

157. D. J. Gavaghan and S. W. Feldberg, *J. Electroanal. Chem.*, **491**, 103–110 (2000).

158. J. K. Stark, Y. Ding, and P. A. Kohl, *J. Electrochem. Soc.*, **160**, D337–D342 (2013).

159. H.-C. Yu, D.-H. Yeon, A. Van der Ven, and K. Thornton, *Acta Mater.*, **55**, 6690–6704 (2007).

160. R. P. Seward and E. C. Vieira, *J. Phys. Chem.*, **62**, 127–128 (1958).

161. Y. Chernyak, *J. Chem. Eng. Data*, **51**, 416–418 (2006).

162. K. K. Karkkainen, A. H. Sihvola, and K. I. Nikoskinen, *IEEE Trans. Geosci. Remote Sens.*, **38**, 1303–1308 (2000).

163. G. Bieker, M. Winter, and P. Bieker, *Phys. Chem. Chem. Phys.*, **17**, 8670–8679 (2015).

164. J. R. Davis, *Corrosion: Understanding the Basics*, p. 574, ASM International, Materials Park, OH, USA, (2000).

165. T.-S. Huang, S. Zhao, G. S. Frankel, and D. A. Wolfe, *Corrosion*, **63**, 819–827 (2007).

166. G. T. Gaudet, W. T. Mo, T. A. Hatton, J. W. Tester, J. Tilly, H. S. Isaacs, and R. C. Newman, *AIChE J.*, **32**, 949–958 (1986).

167. R. Landolfo, L. Cascini, and F. Portioli, *Sustainability*, **2**, 2163–2175 (2010).

168. S. M. Sharland, *Corros. Sci.*, **27**, 289–323 (1987).

169. P. Ernst and R. C. Newman, *Corros. Sci.*, **44**, 927–941 (2002).

170. N. Birbilis and R. G. Buchheit, *J. Electrochem. Soc.*, **152**, B140 (2005).

171. N. Birbilis and R. G. Buchheit, *J. Electrochem. Soc.*, **155**, C117 (2008).

172. J. N. Harb and R. C. Alkire, *Corros. Sci.*, **29**, 31–43 (1989).

173. O. Guseva, J. A. DeRose, and P. Schmutz, *Electrochim. Acta*, **88**, 821–831 (2013).

174. W. J. Boettinger, J. A. Warren, C. Beckermann, and A. Karma, *Annu. Rev. Mater. Res.*, **32**, 163–194 (2002).

175. S. G. Kim, W. T. Kim, and T. Suzuki, *Phys. Rev. E*, **60**, 7186–7197 (1999).

176. J. A. Stewart and D. E. Spearot, *Comput. Mater. Sci.*, **123**, 111–120 (2016).

177. L.-Q. Chen and W. Yang, *Phys. Rev. B*, **50**, 15752–15756 (1994).

178. J. A. Warren, R. Kobayashi, A. E. Lobkovsky, and W. Craig Carter, *Acta Mater.*, **51**, 6035–6058 (2003).

179. M. Koslowski, A. M. Cuitiño, and M. Ortiz, *J. Mech. Phys. Solids*, **50**, 2597–2635 (2002).

180. Y.-H. Wen, L.-Q. Chen, and J. A. Hawk, *Model. Simul. Mater. Sci. Eng.*, **20**, 035013 (2012).

181. L.-Q. Chen, *Scr. Metall. Mater.*, **32**, 115–120 (1995).

182. N. Moelans, B. Blanpain, and P. Wollants, *Phys. Rev. B*, **78**, 024113 (2008).

183. L.-Q. Chen, *Annu. Rev. Mater. Res.*, **32**, 113–140 (2002).

184. T. Uehara and R. F. Sekerka, *J. Cryst. Growth*, **254**, 251–261 (2003).

185. S. M. Wise, J. S. Lowengrub, J. S. Kim, and W. C. Johnson, *Superlattices Microstruct.*, **36**, 293–304 (2004).

186. R. L. Pego, *Proc. R. Soc. A*, **422**, 261–278 (1989).

187. B. Orvananos, T. R. Ferguson, H.-C. Yu, M. Z. Bazant, and K. Thornton, *J. Electrochem. Soc.*, **161**, A535–A546 (2014).

188. L. K. Aagesen, L. K. Lee, P. C. Ku, and K. Thornton, *J. Cryst. Growth*, **361**, 57–65

(2012).

189. L. K. Aagesen, M. E. Coltrin, J. Han, and K. Thornton, *J. Appl. Phys.*, **117** (2015).

190. S. DeWitt and K. Thornton, *J. Phys. Chem. C*, **120**, 2419–2431 (2016).

191. J. Kim, L. K. Aagesen, J. H. Choi, J. Choi, H. S. Kim, J. Liu, C.-R. Cho, J. G. Kang, A. Ramazani, K. Thornton, and P. V. Braun, *Adv. Mater.*, **28**, 9452–9452 (2016).

192. H. S. Isaacs, J.-H. Cho, M. L. Rivers, and S. R. Sutton, *J. Electrochem. Soc.*, **142**, 1111 (1995).

193. W. J. M. Rankine, *Philos. Trans. R. Soc. London*, **160**, 277–288 (1870).

194. N. Moelans, A. Godfrey, Y. Zhang, and D. Juul Jensen, *Phys. Rev. B*, **88**, 1–10 (2013).

195. N. Moelans, *Acta Mater.*, **59**, 1077–1086 (2011).

196. D. Lindell and R. Pettersson, *Mater. Corros.*, **66**, 727–732 (2015).

197. S. H. Crandall, *Q. Appl. Math.*, **13**, 318–320 (1955).

198. D. Young, *Trans. Am. Math. Soc.*, **76**, 92–92 (1954).

199. J. R. Rumble, D. R. Lide, and T. J. Bruno, *CRC Handbook of Chemistry and Physics*, 98th ed., CRC Press, Boca Raton, (2017).

200. Q. Meng and G. S. Frankel, *J. Electrochem. Soc.*, **151**, B271 (2004).

201. H. S. Isaacs, *J. Electrochem. Soc.*, **120**, 1456 (1973).

202. S. M. Ghahari, D. P. Krouse, N. J. Laycock, T. Rayment, C. Padovani, T. Suter, R. Mokso, F. Marone, M. Stampanoni, M. Monir, and A. J. Davenport, *Corros. Eng. Sci. Technol.*, **46**, 205–211 (2011).

203. N. J. Laycock and R. C. Newman, *Corros. Sci.*, **39**, 1771–1790 (1997).

204. H. S. Isaacs and G. Kissel, *J. Electrochem. Soc.*, **119**, 1628 (1972).

205. I. L. Rosenfeld and I. S. Danilov, *Corros. Sci.*, **7**, 129–142 (1967).

206. A. Shahryari, J. A. Szpunar, and S. Omanovic, *Corros. Sci.*, **51**, 677–682 (2009).

207. M. D. McKay, R. J. Beckman, and W. J. Conover, *Technometrics*, **21**, 239–245 (1979).

208. K. Levenberg, *Q. Appl. Math.*, **2**, 164–168 (1944).

209. D. W. Marquardt, *J. Soc. Ind. Appl. Math.*, **11**, 431–441 (1963).

210. K. N. Wood, M. Noked, and N. P. Dasgupta, *ACS Energy Lett.*, **2**, 664–672 (2017).

211. M. Barghamadi, A. Kapoor, and C. Wen, *J. Electrochem. Soc.*, **160**, A1256–A1263 (2013).

212. P. G. Bruce, S. A. Freunberger, L. J. Hardwick, and J.-M. Tarascon, *Nat. Mater.*, **11**, 19–29 (2011).

213. L. F. Nazar, M. Cuisinier, and Q. Pang, *MRS Bull.*, **39**, 436–442 (2014).

214. L. Cheng, L. A. Curtiss, K. R. Zavadil, A. A. Gewirth, Y. Shao, and K. G. Gallagher, *ACS Energy Lett.*, **1**, 503–509 (2016).

215. S. E. Doris, A. L. Ward, P. D. Frischmann, L. Li, and B. A. Helms, *J. Mater. Chem. A*, **4**, 16946–16952 (2016).

216. J.-Q. Huang, T.-Z. Zhuang, Q. Zhang, H.-J. Peng, C.-M. Chen, and F. Wei, *ACS Nano*, **9**, 3002–3011 (2015).

217. Y. Cao, X. Meng, and J. W. Elam, *ChemElectroChem*, **3**, 858–863 (2016).

218. L. Chen, J. G. Connell, A. Nie, Z. Huang, K. R. Zavadil, K. C. Klavetter, Y. Yuan, S. Sharifi-Asl, R. Shahbazian-Yassar, J. A. Libera, A. U. Mane, and J. W. Elam, *J. Mater. Chem. A*, **5**, 12297–12309 (2017).

219. H. Kim, J. T. Lee, D.-C. Lee, M. Oschatz, W. Il Cho, S. Kaskel, and G. Yushin, *Electrochem. commun.*, **36**, 38–41 (2013).

220. A. Schwöbel, R. Hausbrand, and W. Jaegermann, *Solid State Ionics*, **273**, 51–54 (2015).

221. P. Hartmann, T. Leichtweiss, M. R. Busche, M. Schneider, M. Reich, J. Sann, P. Adelhelm, and J. Janek, *J. Phys. Chem. C*, **117**, 21064–21074 (2013).

222. S. Wenzel, D. A. Weber, T. Leichtweiss, M. R. Busche, J. Sann, and J. Janek, *Solid State Ionics*, **286**, 24–33 (2016).

223. S. Wenzel, S. Randau, T. Leichtweiß, D. A. Weber, J. Sann, W. G. Zeier, and J. Janek, *Chem. Mater.*, **28**, 2400–2407 (2016).

224. S. Xu, R. M. Jacobs, H. M. Nguyen, S. Hao, M. Mahanthappa, C. Wolverton, and D. Morgan, *J. Mater. Chem. A*, **3**, 17248–17272 (2015).

225. B. Put, P. M. Vereecken, M. J. Mees, F. Rosciano, I. P. Radu, and A. Stesmans, *Phys. Chem. Chem. Phys.*, **17**, 29045–29056 (2015).

226. S. Wenzel, T. Leichtweiss, D. Krüger, J. Sann, and J. Janek, *Solid State Ionics*, **278**, 98–105 (2015).

227. S. Hori, M. Kato, K. Suzuki, M. Hirayama, Y. Kato, and R. Kanno, V. Sprenkle, Editor. *J. Am. Ceram. Soc.*, **98**, 3352–3360 (2015).

228. R. Djenadic, M. Botros, C. Benel, O. Clemens, S. Indris, A. Choudhary, T. Bergfeldt, and H. Hahn, *Solid State Ionics*, **263**, 49–56 (2014).

229. S. C. Jung and Y.-K. Han, *J. Phys. Chem. Lett.*, **4**, 2681–2685 (2013).

230. K. Yamamoto, R. Yoshida, T. Sato, H. Matsumoto, H. Kurobe, T. Hamanaka, T. Kato, Y. Iriyama, and T. Hirayama, *J. Power Sources*, **266**, 414–421 (2014).

231. S. C. Jung, H.-J. Kim, J. W. Choi, and Y.-K. Han, *Nano Lett.*, **14**, 6559–6563 (2014).

232. S. Hori, K. Suzuki, M. Hirayama, Y. Kato, T. Saito, M. Yonemura, and R. Kanno, *Faraday Discuss.*, **176**, 83–94 (2014).

233. G. E. Dieter, *Mechanical Metallurgy*, 3rd ed., McGraw-Hill Education, (1986).

234. L. Vegard, *Zeitschrift für Phys.*, **5**, 17–26 (1921).

235. B. L. Trembacki, D. R. Noble, V. E. Brunini, M. E. Ferraro, and S. A. Roberts, *J. Electrochem. Soc.*, **164**, E3613–E3626 (2017).

236. V. Malavé, J. R. Berger, H. Zhu, and R. J. Kee, *Electrochim. Acta*, **130**, 707–717 (2014).

237. D. Fan and L.-Q. Chen, *Acta Mater.*, **45**, 611–622 (1997).

238. C. Zener, *Elasticity and Anelasticity of Metals*, University of Chicago Press, Chicago, (1948).

239. R. Hill, *Proc. Phys. Soc. London Sect. A*, **65**, 349–354 (1952).

240. A. Kelly and K. M. Knowles, *Crystallography and Crystal Defects*, John Wiley & Sons, Ltd, Chichester, UK, (2012).

241. R. Schultz, *Lithium: Measurement of Young's Modulus and Yield Strength*, p. 1-6, Batavia, IL, (2002).

242. C. W. Monroe and J. Newman, *J. Electrochem. Soc.*, **151**, A880 (2004).

243. Y. Wang and Y. T. Cheng, *Scr. Mater.*, **130**, 191–195 (2017).

244. H. C. Edwards, C. R. Trott, and D. Sunderland, *J. Parallel Distrib. Comput.*, **74**, 3202–

3216 (2014).

245. B. L. Chamberlain, in *Programming Models for Parallel Computing*, P. Balaji, Editor, p. 129–159, The MIT Press, Cambridge, MA (2015).

246. X. Chen, J. Li, X. Cheng, H. Wang, and Z. Huang, *Mater. Sci. Eng. A*, **715**, 307–314 (2018).

247. J. Yang, H. Yang, H. Yu, Z. Wang, and X. Zeng, *Metall. Mater. Trans. A*, **48**, 3583–3593 (2017).

248. D. A. Macatangay, S. Thomas, N. Birbilis, and R. G. Kelly, *Corrosion*, **74**, 153–157 (2018).

249. S. Bose, D. Ke, H. Sahasrabudhe, and A. Bandyopadhyay, *Prog. Mater. Sci.*, **93**, 45–111 (2018).

250. X. Lou, P. L. Andresen, and R. B. Rebak, *J. Nucl. Mater.*, **499**, 182–190 (2018).

251. C. Xu, Z. Ahmad, A. Aryanfar, V. Viswanathan, and J. R. Greer, *Proc. Natl. Acad. Sci.*, **114**, 57–61 (2017).